(64)

Local-Rules Based Topological Modeling of Tetrahedral Ceramic Network Structures

by

Caroline Esther Jesurum

Sc.B., Carnegie Mellon University (1991)
S.M., Massachusetts Institute of Technology (1995)

Submitted to the Department of Mathematics
in partial fulfillment of the requirements for the degree of

Doctor of Philosophy

at the

MASSACHUSETTS INSTITUTE OF TECHNOLOGY

February 1998

Author .....
.....
Department of Mathematics
December 16, 1997

Certified by...
.....
Bonnie Berger
Samuel A. Goldblith Associate Professor of Mathematics
Thesis Supervisor

Certified by....
.....
Linn W. Hobbs
John F. Elliott Professor of Materials
esis Supervisor

Accepted by .....
.....
Hung Cheng
Chairman, Applied Mathematics

Accepted by .....
.....
Richard Melrose
Chairman, Departmental Committee on Graduate Students

Local-Rules Based Topological Modeling of Tetrahedral Ceramic Network Structures

by

Caroline Esther Jesurum

Submitted to the Department of Mathematics
on December 16, 1997, in partial fulfillment of the
requirements for the degree of
Doctor of Philosophy

Abstract

This thesis presents the theory and implementation of a computer modeling tool for simulating the growth of polyhedral-based molecular structures.

We are interested in the possible tetrahedral network structures of glasses and have developed a local rules based theory for modeling such structures. Based on the work of Berger *et al.* [5] in which local rules are utilized in modeling the formation of virus shells from their protein subunits, we have designed a simulation which, similarly, uses local rules to model the formation of networks with tetrahedral subunits. Using only information about how a given tetrahedron connects to its neighbors, we can generate large model structures quickly. A set of local rules is, simply, a description of how a given tetrahedron is connected to its neighboring tetrahedra. For example, in SiO_2 two tetrahedra meet at each corner. Therefore, a set of rules would describe, for each corner of an initial tetrahedron, the relative orientation of a single neighboring tetrahedron and the corner of that tetrahedron which will be connected to the initial tetrahedron. Our algorithm takes the information given by these rules and iteratively "grows" arbitrarily large structures. In addition to discovering possible structures, we are able to quantify such structures according to local properties such as irreducible ring counts and local cluster analysis [82]. We show that local clusters can be a useful measure in differentiating seemingly similar structures (for example, crystalline cristobalite and tridymite) and we provide local cluster analysis for both crystalline and aperiodic structures.

We begin our study by examining the local interactions in six silica crystalline polymorphs (namely quartz, tridymite, cristobalite, moganite, coesite and keatite) as well as polymorphs for Si_3N_4 and SiC. Most of these structures can each be entirely described by a single tetrahedron and its immediate connections (we refer to this as a rules set with one type). Moganite, coesite, keatite and α-Si_3N_4, by contrast, have two inequivalent tetrahedron environments and require a rules set with more than one type of tetrahedron. The irreducible ring counts and local cluster representation obtained for these silicon compound structures have confirmed and extended earlier hand-modeling results [81].

By deviating slightly from the rules for any of these crystalline structures, we are analogously able to model glasses that have similar local structure but aperiodic global structure. We use a mass-spring model to minimize tetrahedral defects (bond length deviations and X-Si-X angle deviations) by relaxing the whole structure at each incremental addition. We present glass structures obtained by deviating from these rules using two basic techniques.

The first involves an offset in the orientation of the initial tetrahedron which effects the bond angles achieved and the second is a deviation in the connection rotations. These structures locally resemble their crystalline derivatives and have been analyzed for representative local clusters, bond angle distributions, density and radial distribution function.

In addition to generating amorphous structures based on deviant rules, we model the amorphization of network structures due to a disordering event. Many crystalline ceramics can be topologically disordered (amorphized) by disordering radiation events involving high-energy collision cascades or (in some cases) successive single-atom displacements. We are interested in both the potential for disorder and the possible aperiodic structures adopted following the disordering event. In order to study the response of tetrahedral networks to radiation, we have adopted a simple model of irradiation in which all bonds in the neighborhood of a designated tetrahedron are destroyed, and we reform the bonds in this region according to a set of (possibly different) local rules appropriate to the environmental conditions. Component forces are applied that act to minimize the distance between near, compatible corners and minimize the deviation from the rules. The resulting structure is then analyzed for irreducible ring statistics, radial distribution, bond angle distributions, underconnection and density.

Keywords: amorphous silica, amorphization, topological modeling, local rules.

Thesis Supervisor: Bonnie Berger
Title: Samuel A. Goldblith Associate Professor of Mathematics

Thesis Supervisor: Linn W. Hobbs
Title: John F. Elliott Professor of Materials

Acknowledgments

This is a pretty hard thing to write. Starting from the beginning of my graduate career, I would like to thank Mike Sipser. He called me up March 7, 1991 (I remember it being my excuse to *really* celebrate my birthday) and asked me to join the theory group. He was the bearer of good tidings – tidings that changed the direction of my life. Thanks to the group formerly known as the Theory Group for being such a supportive environment and family. In particular, Tom Leighton and Charles Leiserson who have always been there to help me with problems either academic or personal.

I can't say where I would be now if it weren't for the faith and encouragement of Lenore Cowen. She taught me how to do research and gave me enough support and confidence to get results. I feel my greatest contribution to the field of mathematics was the work I did with her when she kidnapped me to DIMACS. Thanks also to DIMACS for supporting me for three weeks that were the first fruitful three weeks of research I'd ever done.

Thanks to Bonnie Berger for picking me up as an advisee when I was floundering aimlessly. She found me a project and the means to continue working. She, along with Lenore, was a most nurturing friend and mentor. She gave me the confidence to continue pushing for this degree, and she made me believe in myself and that I deserve this honor.

Thanks to Vinay Pulim for just about all the implementation of the glass code. He's an amazing pseudo-code translator and he's always pulled through for me when I came to him in a panic due to some or other deadline.

For his ability to get me to work, thanks goes to Linn Hobbs. He has been a pleasure to work with these past three years, always asking the right questions and insisting on good answers. For all the writing he put into the papers that would later comprise the chapters of this thesis, I am greatly indebted to him. This thesis could never have been written without his interdisciplinary vision. And speaking of other disciplines, I also thank him for teaching

The research reported in this thesis was supported primarily by the Department of Energy (DoE) under grant DE-FG02-89ER45396. Additional support came from the Advanced Research Projects Agency (ARPA) under grant N00014-95-1-1246 and the DoE grant DE-FG02-95ER25253.

me a thing or two about *vino*.

Thanks to all my friends in the group through the years: Tom and Cliff made those lunch times more enjoyable before they up and went to Dartmouth. Marcos, Ravi, Alex, Ray, Andrew and Mike. Probably my closest friend in the group since I got here, Ethan. Too bad we were always too lazy to hang out more. Thanks to other people in and around the lab: thanks to Philip for helpful discussions when I was lost in the materials world, thanks to all the folks upstairs in AI for an easy social escape.

Thanks to the womens hockey team for being one of the main reasons I never gave up altogether and quit school. I mean, where else could I get all that ice time if I weren't a student? Thanks to Susie for being so friendly that I wasn't afraid to go out and try; thanks to Helen and Jill for being my sisters in joining the team; thanks to my great friends, Cynara, Smitty and Lisa. It's been a fun ride.

Thanks need to go to the men that put up with me (and supported me and helped keep me together). In the beginning there was Bobby. He was a great and fun friend. And he is also someone I look up to and respect. Then there was Stephen. Thanks to him I made it through my orals and my change of advisors. He continues to be a great friend and is always there for support and useful advice. And Tony. He's my partner—boyfriend or not. He's been there to share all my triumphs and failures over the past couple of years and he never once showed me that he doubted my ability to finish even for a second; he's my number one fan.

Finally I'd like to thank my family. For supporting me without nagging me, thanks mom. You give a good name to Jewish mothers everywhere. You seemed genuinely concerned with my happiness without having an agenda for my success. Thanks dad who first inspired the love of math that I have. You have been my hero since I was a girl. Thanks to my great brothers. Alex who has always been there when I'd be starting out; you were at CMU when I showed up and you stayed till I was settled; you were in MA when I showed up and so I always had a family member near when I needed one. David, my faithful hockey fan, thanks for finally moving to Boston and bringing the whole family together again...

ESTHER JESURUM
Cambridge, Massachusetts
December, 1997

Contents

List of Figures

List of Tables

Chapter 1

Introduction

As nuclear power has clearly become an economically attractive energy source, so the development of materials for reactor construction and the disposal of nuclear waste have become increasingly pressing issues. The problem of finding adequate structural and containment materials has been reduced to finding materials which are stable under different types of disordering radiation. When referring to crystals, stability is measured by amorphizability, that is, how much radiation is needed before the material in question is no longer crystalline (periodic). Recently there has been an interest in studying the stability of glasses in addition to crystalline materials. Since glasses are initially aperiodic, how do we measure their stability? This is a difficult question to answer. Because glasses are aperiodic, it is difficult to know much about their structure; standard empirical methods such as x-ray crystallography fail to give much useful information about materials that are aperiodic. In order to learn more about glass structure, we have developed a mathematical model. By examining the local topological structure of glasses, we help develop a language within which to describe aperiodic tetrahedral structures.

In addition to modeling glass structure, we are interested in modeling the *amorphizability* of crystalline networks. One way to predict amorphizability is to examine networks for available structural freedom. This topic has been extensively studied using a variety of techniques. Dove *et al.* [23] study what they refer to as "rigid unit modes" to differentiate between networks which are constrained and those that are flexible for possible insight into phase transition. Jacobs and Thorpe [68] develop an algorithm called "the pebble game" to determine "floppy modes" in structures, and these floppy modes are areas presumably easier to amorphize. Gupta and Cooper [43] attempt to characterize structural freedom globally by counting spatial freedom as a function of the structural polyhedra, connectivity and dimensionality. In Chapter 2 we investigate this approach for predicting amorphizability and uncover some possible limitations.

In order to explain the differences in amorphizability under disordering radiation of var-

ious tetrahedral networks we developed a computer model for simulating assembly and reassembly of the tetrahedral network units. We were motivated to use this approach because hand modeling had revealed useful topological insights into possible aperiodic network structures [82, 54]. Similarly, elementary constraint counting [43] had been successfully applied to predict relative amorphizabilities of crystalline structures and had revealed anomalies such as the necessity of anti-site disorder in amorphization of SiC (see Chapter 2). We use a simple algorithm to model the growth of many crystalline polymorphs which have tetrahedral components, and with this same algorithm we model the assembly of amorphous structures which are topologically feasible. The simulator uses local rules [5] to generate large tetrahedral networks relatively quickly. A current alternative, molecular dynamics-based simulations [121], yields credible results, but finding an accurate potential is often difficult, and the simulations can be computationally expensive. Our model simulates hand modeling for the purposes of analyzing the mathematical possibilities for the topologies of amorphous materials. As a first step, we have concentrated on developing rules for crystal growth (or regrowth following cascade disordering). The procedure presumes that crystal growth is directed by local interactions of the tetrahedral subunits. During the growth procedure, the orientation of a tetrahedral subunit dictates the orientation of its neighboring subunits. Different sets of local interactions, or local rules, were designed to produce different crystal topologies.

In order to model glassy, or amorphous, structures, we merely modify the rules which were used to erect crystalline models. In Section 5.1 we pursue different ways of modifying crystal rules to develop "faulty" rules sets: that is, rules which will, with the addition of optimizing springs (described in Section 5.1.2 and in more detail in Section A.5.5), generate aperiodic structures. To model the amorphization of a precursor model (Section 5.2) we simulate the local disruption caused by a disordering event (radiation). We take the simple approach of breaking all the bonds in a specified region and then reforming those bonds according to a (possibly different) set of rules.

1.1 Materials research background

1.1.1 Silica glasses

Much of this thesis is focused on the study of silica. SiO_2 is an important compound in many scientific disciplines and technical applications. A substantial portion (12%) of the earth's surface comprises silica in the form of mineral forms of quartz, quartz inclusions in other minerals, and quartzite sands. Related silicates comprise almost all the remain-

der. Mineral and, more recently, hydrothermally-grown synthetic quartz have long been used in frequency control because of the piezoelectric property of quartz [11]. Silica melts (melting point $T_m = 2001K$), cooled quickly enough through a glass transition temperature ($T_g \approx 1333K$), form vitreous silica which (like Cu, NaCl and Si) has long served structural chemists as a paradigm for a whole class of solid structures, in this case oxide network glasses [142]. Vitreous silica fibers are now the favored vehicle for optical telecommunications [91], and amorphous silica occurs widely in nature in the skeletons of radiolaria, diatoms and sponges [112] and in pyrolyzed plant matter. High-silica zeolites and clathrates [77, 89, 51] are highly porous, open framework crystalline silicas with tunnel or cage structures synthesized around template molecules and useful as absorbants, catalysts, and hosts for guest catalysts. Aerogels and xerogels of silica are also important as catalytic hosts, as precursors in various processing routes for other ceramics, and for their exceptionally low densities [9]. Silica, as an oxidation product of silicon, is the primary insulator dielectric in MOS electronic devices [2] and can form a critical diffusion-barrier layer in high-temperature corrosion scales formed on silicon-bearing high-temperature metal alloys [75].

Silica crystallizes in at least seven known compact polymorphs [47, 50] in addition to the two classes of porous framework structures; phase transformations between them are reconstructive and do not occur readily below the melting point, so that all are at least metastable at room temperature. Displacive transformations occur in several which lower symmetry from higher-temperature β forms (which may be dynamical averages) to lower-temperature α forms. In six of the compact polymorphs—tridymite and cristobalite (high-temperature forms), keatite (a hydrothermally-grown form: [74, 47]), quartz (hydrothermally-grown), moganite (also known as the mineral lutecite: [34, 90, 48]) and coesite (a high-pressure form: [13, 50]), as well as in the zeolitic silicalites [33] and clathrasils—silicon is coordinated to four oxygens to form [SiO_4] tetrahedra which share each of their four vertices with a second neighboring tetrahedron ("{4,2}-connected") to form continuous tetrahedral nets. In stishovite (another high-pressure form: [118, 50], silicon is octahedrally coordinated, with [SiO_6] octahedra sharing vertices and edges as in the rutile structure of TiO_2. Less is known about the structure of vitreous silica, although it is among the most studied glasses. Its structure is almost certainly that of a continuous three-dimensional network of largely intact vertex-sharing [SiO_4] tetrahedra [138, 137], with a low density of unshared oxygen vertices (non-bonded oxygens, or NBOs) . Vitreous silica exhibits a broad range of inter-tetrahedral (Si-O-Si) angles, as deduced from diffraction studies [92] and solid-state NMR [12], with an average value $\sim 145°$, corresponding to minimum structure energy [104] Several models have been constructed to represent the possible structure, for example by decorating with oxygen random Si networks generated by bond switching [46] or using building algorithms

based on preserving the observed mean Si-O-Si angle (from the second peak of the experimental real-space correlation function) and avoiding steric hindrances [37]; structure models have also been generated using molecular dynamics approaches [122, 121]. Crystalline quartz can be amorphized under pressure, reversibly, though with an observed hysteresis [49]. Pressure-induced amorphization, as well as $\alpha - \beta$ transitions, may be related to propagation of accordion-like rigid unit vibrational modes [23] of undistorted tetrahedra with minimal reconstruction.

At least four of the tetrahedral crystalline polymorphs of silica are known to amorphize under both displacive and ionizing irradiation (quartz: [98, 18, 62, 96, 67]; tridymite & cristobalite: [101, 102]; coesite: [39]), as well as the quartz-analogue $AlPO_4$ [115]. Neutron irradiation of quartz produces a 14% decrease in density (swelling), while neutron-irradiated vitreous silica compacts by 3% to an identical terminal density [98, 99, 100]. Radiolysis of vitreous silica likewise results in compaction [26], which has been attributed to changes in network topology [22]. The amorphizing transformation under ionizing radiation appears to involve a radiolytic mechanism [62] analogous to that proposed for vitreous silica [40] in which single Si-O bonds are severed, peroxy species are generated, and the arrangement of tetrahedra reconstructs stochastically.

1.1.2 Si_3N_4 and SiC

Silicon nitride, found in α and β crystalline polymorphs, is an important structural ceramic and fiber-reinforced composite matrix, while SiC, also found in two polymorphic forms α and β and numerous polytypic variants, is a principal reinforcing fiber, a potential high-temperature device semiconductor, and a leading candidate (in SiC–SiC fiber composite form) for near-first-wall applications in thermonuclear fusion reactors.

1.1.3 Amorphization of ceramic structures

Cascade amorphization in silicas

Radiation effects in silicas were an early focus of study [76, 99]. Both crystalline [62] and amorphous [40] forms are susceptible to radiolysis from the ionizing component of radiation, resulting in a Frenkel defect comprising an oxygen vacancy (E' center) and some form of oxygen interstitial, probably a peroxy linkage. The overall efficiency has been variously measured at ~2000 eV per stable E' center [97, 22], though transient volume expansion has been observed with an efficiency as high as 100 eV/Frenkel pair in quartz and 1000 eV/Frenkel pair in vitreous silica [120]. Crystalline silicas eventually amorphize radiolytically, for example under fast electron irradiation [62, 96, 101] after a total absorbed excita-

tion energy density of $\sim 10^{34}$ eV/m3 (0.6 TGy). They are likewise observed to amorphize collisionally during neutron or ion irradiation at a displacement density of ~0.1 displacements per atom (dpa) [135, 98, 86, 25], corresponding to about 7 eV/atom deposited into collisional processes (or $\sim 5 \times 10^{29}$ eV/m3) and accompanied by density changes which amount to 14.7% *dilatation* for quartz [135]. An analogous *compaction* of vitreous silica under neutron and ion irradiation is observed to proceed at the somewhat slower rate of $\sim 8 \times 10^{28}$ eV/m3 per 1% compaction [100, 26] and to saturate earlier at 2.7% [135, 98, 86], the density change correlating with refractive index changes [22].

A remarkable observation is that irradiated crystalline silica polymorphs and vitreous silica end up at the identical terminal density of 2.26×10^3 kg/m3 [135, 98, 86] with only small differences in radial correlations deduced from diffraction studies [110, 111, 102]. Geologically, this terminal state would be referred to as the metamict state [30], and for ease of reference we here adopt that moniker. The average Si-O-Si inter-tetrahedral bond angle can be deduced from the mean Si-Si correlation distance obtained from diffraction [92] or NMR [12]. For the terminal amorphous state it is 134° [22], which represents a decrease of 10° from that of both α-quartz (143.6°) and vitreous silica (145° [104]). The implications from both sets of observations are that various terminal amorphized structures are at least similar and distinguishable from that of vitreous silica.

Cascade amorphization of ceramics

Most crystalline ceramic and semiconductor structures can be appreciably disordered and eventually amorphized during ion implantation by radiative events involving high-energy collision cascades, occasioning significant changes in physical and mechanical properties. Different compounds exhibit wide variations in their critical responses with respect to both ion fluence and irradiation temperature. Network structures, such as Si, SiO_2, SiC—useful in many environments involving deliberate or incidental irradiation with energetic ions—are among the most susceptible. Three questions arise in considering this variety of responses: 1) Why are some compounds more susceptible and others less susceptible to disordering? 2) What is the nature of the disordered arrangement within a collision cascade? 3) What is the final overall structure of the disordered or amorphized material?

Considerations of bond type, strength and preference have long been used to arrive at an answer to the first question, with modest success. But bond criteria do not explain why, for example, SiO_2 is so easy to amorphize and Si_3N_4 so difficult, given that both structures exhibit significant covalent bonding and tetrahedral coordination of the Si; nor why phosphates, based on $[PO_4]$ tetrahedra, should be so much more susceptible than silicates based on $[SiO_4]$ tetrahedra. Amorphization represents topological disordering, in which neither translational nor rotational long-range order is preserved [42, 54]. It was shown several

years ago by Hobbs [58] that topological features of structure are consequently important when one considers disassembly and reassembly of atoms in altered arrangements, and an assessment of the structural constraints by various structure types is in fact surprisingly accurate in predicting their relative susceptibilities to radiation disordering (Chapter 2). The approach is to consider how the structural polytopes (e.g. preferred coordination polyhedra) are connected together, and from their connectivity to establish the constraints on their arbitrary rearrangement. The (meta)stability of the final disordered states derives from the stochastic nature of the rearrangement process and the topological difficulty of returning to the original or other well-ordered arrangements without wholesale atomic mobility.

An answer to the second question in binary (or higher) compounds has recently been sought in molecular-dynamics (MD) simulations of collision cascades, for example in SiC [19] and alkali borosilicate glasses [20]. Similarly, the answer to the third question has been been more thoroughly explored in MD simulations of aperiodic structural arrangements, e.g. in SiO_2 [121, 122] and Si_3N_4 [121]. Application of MD approaches to the structure of melt-quenched glasses suffers shortcomings deriving from unrealistically high quenching rates and difficulty in accounting for long-range constraints imposed by structural topology; the rapidly quenched collision cascade may in fact serve as the more appropriate model subject for the molecular dynamics approach! As an alternative to MD, a second approach for simple networks involves modeling with hand- [81, 80] or computer-based [37] building algorithms and evaluating the structural topology of the result with at least partial tessellations, such as the set of irreducible rings through a polytope and the local cluster of polytopes belonging to the ring set [81, 80].

Collision cascades are the result of stopping energetic medium- to heavy-weight ions in solids and can effect overall structural amorphization through direct impact amorphization [35] or cascade overlap to achieve a critical defect density [35, 128, 130, 129]. The cascade phenomenon represents in many ways an ideal platform for topological modeling, since the violent cascade displacements are largely uncorrelated and represent atomic randomization followed by (in compounds) reassembly into chemically-preferred groupings whose relative immediate dispositions are likely governed by the same sorts of local rules that also apply to long-range-ordered crystalline assembly. This thesis (Section 5.2) reports on application of the local-rules assembly method to model the structure of collision cascades in the network structures of SiO_2, Si_3N_4 and SiC. The objective is to explore the extent to which topological considerations alone can affect the reassembly process and provide a driving force for recrystallization or a conduit for stochastic propagation of topological disorder.

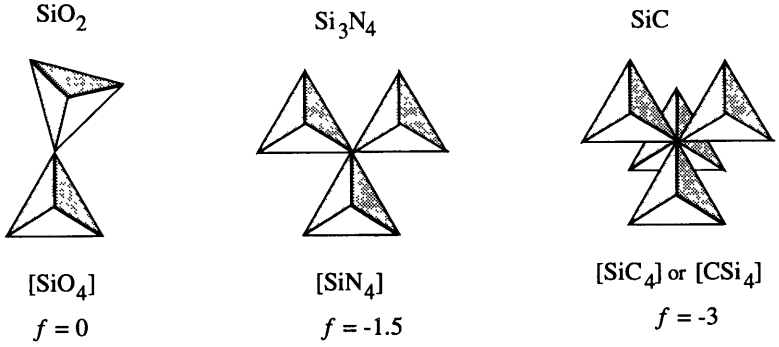

Figure 1.1: Vertex-sharing schemes for SiO_2, Si_3N_4 and SiC.

1.2 Topological representation of ceramic networks

A network is an arrangement of connected nodes that may be described mathematically as a regular graph. Polymers [24] are one class of network structures, as are most biological molecular assemblages such as virus shells comprised of assembled proteins [5]. SiO_2, Si_3N_4 and SiC are three ceramic compounds which adopt network structures featuring vertex sharing of, respectively, $[SiO_4]$, $[SiN_4]$ and $[SiC_4]$ tetrahedra. The connectivity of $[SiX_4]$ tetrahedra (X = O, N or C) in networks of the three compounds is illustrated in Figure 1.1.

In silicas, each of the four vertices of an $[SiX_4]$ tetrahedra (X = O, an oxygen atom, in SiO_2) is shared by two tetrahedra ({4,2} connectivity); in silicon nitride (X = N) by three tetrahedra ({4,3} connectivity); and in SiC (X = C) by four tetrahedra ({4,4} connectivity). Crystalline networks are topologically ordered [43] (Chapter 2), possessing long-range orientational and translational order [42], which may be described in the symmetry-based language of crystallography. The evidence from Raman spectroscopy, X-ray absorption and electron inelastic scattering fine structures, and X-ray, neutron and electron diffraction studies is that {4,2} connectivity also obtains in vitreous silica as well, which is topologically disordered, and cannot be described by symmetry operations. Alternative descriptions of both periodic and aperiodic networks are possible using the topological properties which derive from their connectivities [54].

A full topological description requires a complete tessellation, several of which have been explored [6, 123, 21, 32, 108], but an incomplete tessellation of tetrahedral networks based on one-dimensional rings nearly suffices and has been shown to differentiate the crystalline polymorphs [81]. A ring is a closed circuit along nodal connections (see Section 4.1). A network without ring closures is a tree network whose density increases exponentially with its continual branching of congruent elements; rings in networks are therefore a steric

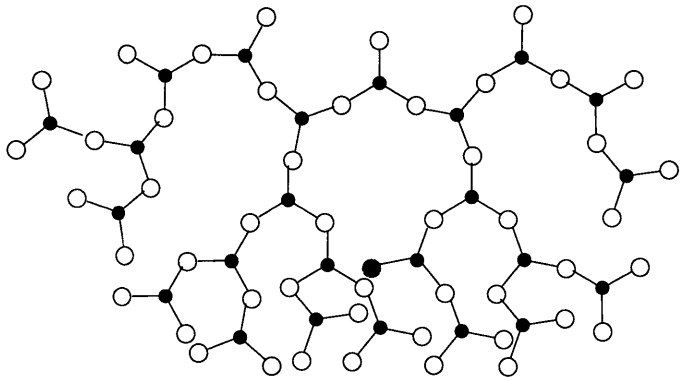

Figure 1.2: A 2-dimensional illustration of the necessity of rings in order to maintain reasonable density.

necessity. We refer to this phenomenon as the "tree density catastrophe" as illustrated in Figure 1.2. The topologically important rings are those minimal circuits which are not the sum of two smaller circuits—i.e. have no short-cuts [38]—which Marians & Hobbs [83] have dubbed primitive rings. In a two-dimensional network of vertex-sharing triangles, each node is the juncture of three connections and is associated with exactly three primitive rings whose average number of segments (size) is $n = 6$ (a consequence of Euler's theorem). This is more easily appreciated if the ring segments are equivalently taken as the triangle edges, only one primitive ring passing through each edge (Figure 1.3). In a three-dimensional network of vertex-sharing tetrahedra (where four node connections intersect at each node), many more rings can be associated with each node (or tetrahedron). For example, in the tridymite or cristobalite polymorphs of silica (Section 4.1), two 6-rings pass through each of the six edges of each tetrahedron, for a total of twelve 6-rings through each node. The set of tetrahedra (or nodes) associated with the set of primitive rings passing through a given tetrahedron (or node) we refer to as the *local cluster* [80, 54]. The local cluster serves as an analogue of a unit cell in a crystalline structure, in that it represents the local topological properties (rather than embodying the local symmetries), but is applicable to crystalline and non-crystalline arrangements alike. It is therefore a useful descriptor for silica network structures [81].

Earlier assembly exercises using hand-built models, subsequently evaluated by computer algorithms from compiled connectivity tables [81, 80], were aimed at discovering the local clusters for five of the crystalline polymorphs and exploring the extendibility of non-crystalline arrangements. Much of this kind of modeling can now be done directly in a computer of workstation size, owing to advances in both computer hardware and fast computational algorithms. Because identifying primitive rings and hand counting them in the more complex structural modifications of silica is extremely tedious and difficult to verify, we have now established computer-based algorithms to erect models of each of the crystalline

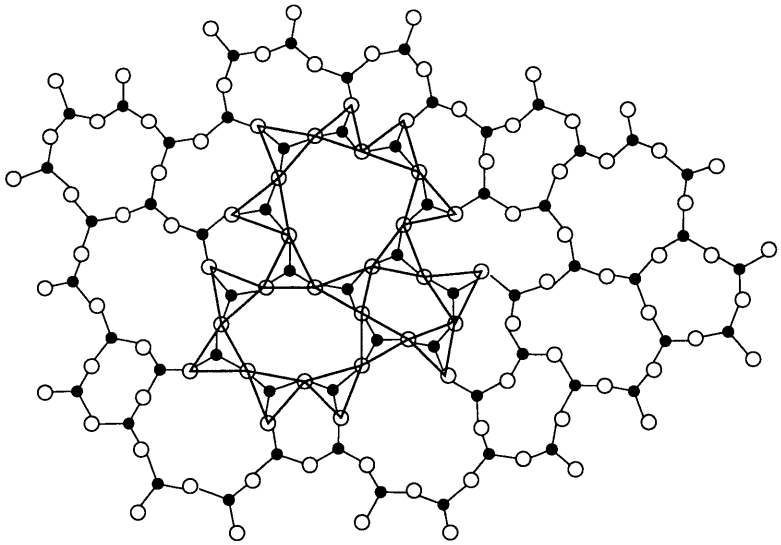

Figure 1.3: Two-dimensional continuous random network of triangular coordination polytopes with highlighted local cluster of tetrahedra comprising three primitive rings.

polymorphs and then find rings and local clusters. These algorithms, which are described in Sections 3.1 and 4.2 respectively (and in greater detail in Appendix A), have been used to complete results from earlier hand-counting of crystalline polymorphs [81] and to illustrate them with facility. The algorithms are also useful in exploring structural limits and, with modification, are equally applicable to non-crystalline constructions, whose extendibility and local clusters can likewise be assessed. Results for two non-crystalline arrangements generated are reported in Section 5.1.

1.3 Previous results and related work

The results reported in this thesis are the synthesis of two ideologies; it is the application of the theory of local rules (Section 1.3.2) to further and enhance the creation of a language within which to describe silicon compounds by their local characteristics (Section 1.3.1).

1.3.1 A language for local descriptions of tetrahedral networks

In her doctoral dissertation [82], Marians develops a precise language with which one can parameterize aperiodic structures through analysis of local characteristics. We choose to focus on local topology to be free of any limitation of global properties such as periodicity. She focused on certain questions which are also of interest to us.

- What arrangements of corner sharing tetrahedra are possible in 3D-space?

- How can we characterize and parameterize these networks?
- How are they constructed?

Marians successfully answers her first two questions through a long and arduous process of hand-modeling tetrahedral network structures, painstakingly labeling each tetrahedron and its corners to be able to correctly collect data from the models. This thesis serves to validate her results and also to complete her work on polymorphs needing larger erected model structures than was feasible by hand. By developing a local rules-based theory about the way structures assemble, we have possible answers to all these questions. We can characterize crystals by the set of rules used to generate them, we show that construction according to these rules is feasible, and we explore the realm of possible structures through the generation of different rules sets.

1.3.2 Theory of local rules

Local rules were first used to develop a language to help describe and simulate the assembly of icosahedral viruses [5]. The study of virus shell structure and assembly is crucial for understanding how viruses reproduce and how anti-viral drugs might interfere with assembly of virus shells. One of the most notable aspects of virus shells is their highly regular structure: they are generally spherical and possess strong symmetry properties without being periodic; almost all human viruses (e.g. rhinovirus, poliovirus, herpesvirus) and many plant and animal viruses are icosahedral. These icosahedral shells are constructed of repeated protein subunits–or coat proteins–which surround their condensed DNA or RNA genomes. A given shell usually consists of hundreds of copies of one protein, but sometimes copies of two or three different proteins.

At first glance, the assembly of the shells seems easy to understand because the structure is so regular, just as are two-dimensional subnetwork tilings in aperiodic silicas in which 6-rings predominate [80]. In fact, it has been difficult to determine the actual pathway though which the subunits interact to form a closed shell composed of hundreds of subunits; in icosahedral viruses this has been particularly difficult to explain because very often the same protein occurs in non-symmetric positions.

The local rule theory can also be used to explain several anomalies, such as the polyomavirus shell structure and a spiraling malformations [4]. It can also be used to model other malformations and possible aperiodic structures as a result of changing various model parameters [107].

Berger and Muir [93, 5] developed a "toolkit" to model virus shell assembly on a Silicon Graphics Indigo 2 computer. The toolkit has been used to explore the tolerance margins of

these shells and possible deformities that may result. The binding interactions and angles of the shell proteins can be varied up to 8% randomly in every direction and roughly the same shell is produced; however, if a hexagon occurs in place of a pentagon, then spiraling occurs. Berger along with Schwartz [106] has also developed a parallel implementation on the Thinking Machines CM-5 computer that substantially speeds up the algorithm. The eventual goal of this work is to develop a computer simulation that allows biologists to view and interfere with the virus assembly process on screen, a process which, like restructuring following radiation-induced disorder, cannot be observed directly in nature.

The parallels to the problem of understanding the assembly of coordination units into aperiodic arrangements in network structures, are strong, and the methodologies are fortunately already well explored. It is clear that local rules must be similarly followed and that the result is the propagation of persistent intermediate-range order (though not topological order) over long distances, as has been demonstrated by Elliott [27] and is evidenced in the first sharp diffraction peak of metamict structures. Several differences in the analogy, however, present concerns which must be addressed. First, viral shell assembly takes place on a topologically two-dimensional surface, whereas amorphization takes place within a three-dimensional volume. On the other hand, the surface is closed in three-dimensions and not initially constrained to be, and Marians [81] has shown the importance of two-dimensional subnetworks in the three-dimensional structure of network solids. Second, energy minimization is accomplished with simple spring constant response. While this may be supposed overly simplistic compared to the empirical potentials and three-body interactions employed in molecular-dynamics simulations (e.g. [121]), it must be remembered that such codes do not assume a priori information about coordination units which we know to exist in such assemblies. In fact, minimization of overall bond-length deviation proved a useful approach for study of the results of bond-switching as an initial approach to structural collapse during amorphization of quartz [69].

1.4 Contributions of this thesis

This thesis presents the motivation, and implementation of a computer simulation tool based on the theory of local rules for erecting tetrahedral network structures.

- *Theory of structural freedom analysis:* We describe a constraint counting method to predict amorphizability. Where this method alone does not suffice to account for variances in amorphizability, simple graph theory can help. We show that by taking an appropriate dual of the graph where the atoms represent vertices and the bonds represent

edges between vertices, there is a great difference between structures with identical constraint counting function values.

- *Local rules approach to modeling is viable:* We find simple rules to govern the growth of structures with various-sized unit-cells as a proof-of-concept for the theory of local rules.

- *Validation and completion of local cluster analysis:* We confirm the previous results for ring counts in silica polymorphs and complete counts for previously unanalyzed silica polymorphs as well as SiC and Si_3N_4 varieties.

- *Amorphous networks and amorphization of crystals:* We describe techniques for generating amorphous network structures as well as providing analysis of the structures produced. Additionally, we describe a simulation for collision cascade disorder.

The remainder of this thesis is organized as follows. In Chapter 2, We present the background for a structural freedom approach to the study of amorphizability as well as a graph-theoretic solution to an amorphizability question unexplained by constraint counting. In Chapter 3 we present local rules for a variety of corner-sharing tetrahedral crystalline structures. In Chapter 4 we discuss tetrahedral local structure in terms of primitive rings and local clusters. In Chapter 5 we discuss ways to generate amorphous and amorphized structures and we analyze the structures produced. In Chapter 6 we discuss future directions of this work and give some concluding remarks.

1.5 Definitions and notation

For the most part this thesis will use the notation popularly recognized in the Materials Science community when referring to crystal structure. Consequently, the $a-$, $b-$ and $c-$axis channels are equivalent to x, y and z respectively. Therefore a [110] view of a structure would be that from the $x = 1, y = 1, z = 0$ view to the origin.

A *unit cell representation* of a crystal is the smallest parallelepiped region which, if repeated, generates the entire structure.

A *ring* in a network is a closed path of nodes (tetrahedra) where each node appears exactly once.

A *primitive ring* in a network is a ring such that for each pair of nodes on the ring, the network distance between the nodes is equal to the minimum ring-distance between them.

A *local cluster* for a node n in a network is the union of all the primitive rings to which n belongs.

Chapter 2

Structural Freedom and Topological Disorder

In this chapter, we present research in constraint counting as an approach to studying the amorphizability of ceramic structures.

2.1 Background for structural freedom analysis

The long-range ordered crystalline state is usually the lowest free-energy form of elemental and compound solids. Higher-energy aperiodic states, such as melt-quenched glasses, represent a failure to crystallize, and few such metastable atomic arrangements survive over geological time scales. Irradiation-induced atomic rearrangements, such as those occurring along the trajectories of swift heavy ions or in discrete collision cascades initiated by lower-energy ion beam irradiation, can result in loss of orientational and translational order ("amorphization") in a much larger range of crystalline structure types and compositions [59] at temperatures below which thermally-activated diffusion processes can initiate epitaxial recrystallization from less disordered neighboring regions. In most solids, with low to moderate melting points, the solid may be induced to melt within a cascade and subsequently quench to an amorphous state (direct impact amorphization), though recrystallization during the rapid cooling of the cascade thermal spike may reduce or eliminate the extent of the amorphous region; in others with high melting points (such as SiC), cascade melting may not occur and the cascade region remains highly-disordered but still crystalline [19]. Amorphization may also occur with overlap of such highly defective regions. A few solids (intermetallic compounds, Si, SiO_2, SiC) may be amorphized by accumulation of single

The research reported in this chapter is joint work with Linn Hobbs, A.N. Sreeram and Bonnie Berger and was first published in [53].

atomic displacements, such as generated by above-displacement-threshold energetic electrons or by radiolysis.

Quenching of a molten cascade volume is akin to glass formation (though the melt structure is likely to be much farther from equilibrium), and there is therefore likely to be a relation between glass-forming ability and ease of amorphization. In particular, the structure of the crystal reflects the coordination preferences of the atoms involved, and the relevant question is whether these preferences can be preserved in alternative aperiodic arrangements. The melt is, moreover, formed within an envelope of crystalline material which provides crystalline nucleation points, so that the ease with which the atoms can structurally rearrange to conform to the surrounding structure is also being tested. In progressive single-displacement amorphization, in which bonds are being broken and atoms displaced serially, one is specifically testing the redundancy of the structural constraints which specify a crystalline structure. In all three cases, what must be evaluated is the *structural freedom* of that crystalline arrangement of the constituent atoms which is stable at the conditions under which the irradiation-induced displacement occurs (including effective temperature and pressure within a cascade for a cascade damage mode) [58].

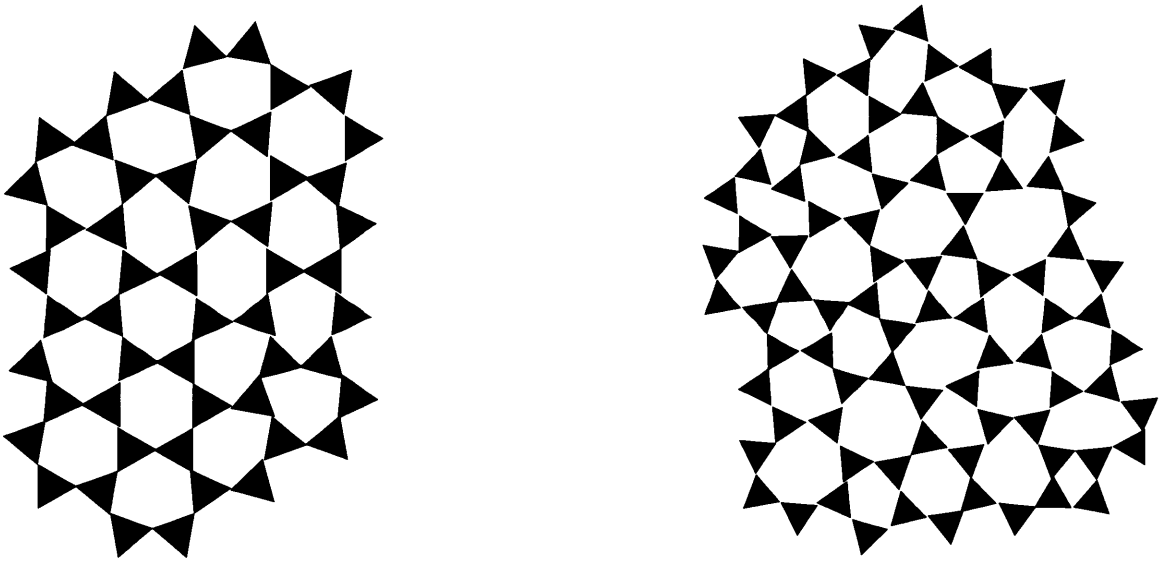

(a) (b)

Figure 2.1: Aperiodic two-dimensional structures constructed from triangle polytopes with identical connectivity, a) topologically ordered, b) topologically disordered.

Amorphization is an example of a transformation in which existing orientational and translational order are lost. Both losses are evident in electron diffraction patterns from amorphized solids which lack Bragg maxima and are radially symmetric. But, it is additionally important to distinguish *topological* disorder from simple loss of spatial correlations

which can arise from uncorrelated distortions; topological disordering implies an actual restructuring of the connections between structural elements (Figure 2.1). Most amorphized structures are probably topologically disordered, but there may be cases (amorphization of compact structures, Section 2.3) where topological order may be at least partially retained.

Amorphized structures are nevertheless not *random* and are still constrained by topological constructional rules and steric considerations which derive from the ways structural elements can be connected together [54]. The *connectivity*, that is, how elements of the structure are connected together, clearly determines the mechanical rigidity of a structure–a relationship explored 130 years ago by J. C. Maxwell [87] in considering the stability of mechanical structures–but also governs the possibility of achieving alternative *extendible* structural arrangements [54].

2.2 Connectivity and structural freedom

A starting point is the identification of characteristic structural units; these are generalized as n-dimensional ($n = 1, 2, 3$) polytopes, which represent bonding proclivities between the constituent atoms–for example, Pauling's coordination polyhedra in ordered compounds (e.g., $[TiO_6]$ octahedra in TiO_2) or polyhedra representing bonding geometries in elemental solids (e.g., regular tetrahedra surrounding Si atoms in elemental silicon, one-dimensional rods in a less-directionally bonded monatomic metal). Their connectivity can be characterized by the number of vertices in the polytope, V; the average number of polytopes sharing each vertex, C; and the relative proportions of corners, edges and faces of the polytopes shared with other polytopes. In some cases, only a single polytope is present, as in SiO_2 structures comprising corner-shared $[SiO_4]$ tetrahedra; in most cases, a single kind of polytope dominates or provides a weak link, as discussed later. Figure 2.2 illustrates some two-dimensional structures generated from one- and two-dimensional polytopes and their respective connectivities, represented as $\{V,C\}$.

A correlation exists between the extendibility of topologically-disordered arrangements and the freedom of structuring polytopes to rearrange (*structural freedom* [54]). Cooper and Gupta [14, 43, 41] have derived the relationship between structural freedom f and connectivity $\{V,C\}$, for structures containing rigid congruent regular polytopes, as the difference of the degrees of freedom (given by the structure dimensionality d) and the number of constraints imposed by neighboring structure

$$f = \delta - C\{\delta - [\delta(\delta+1)/2V]\} - (d-1)(Y/2) - [(p-1)d - (2p-3)](Z/p) \qquad (2.1)$$

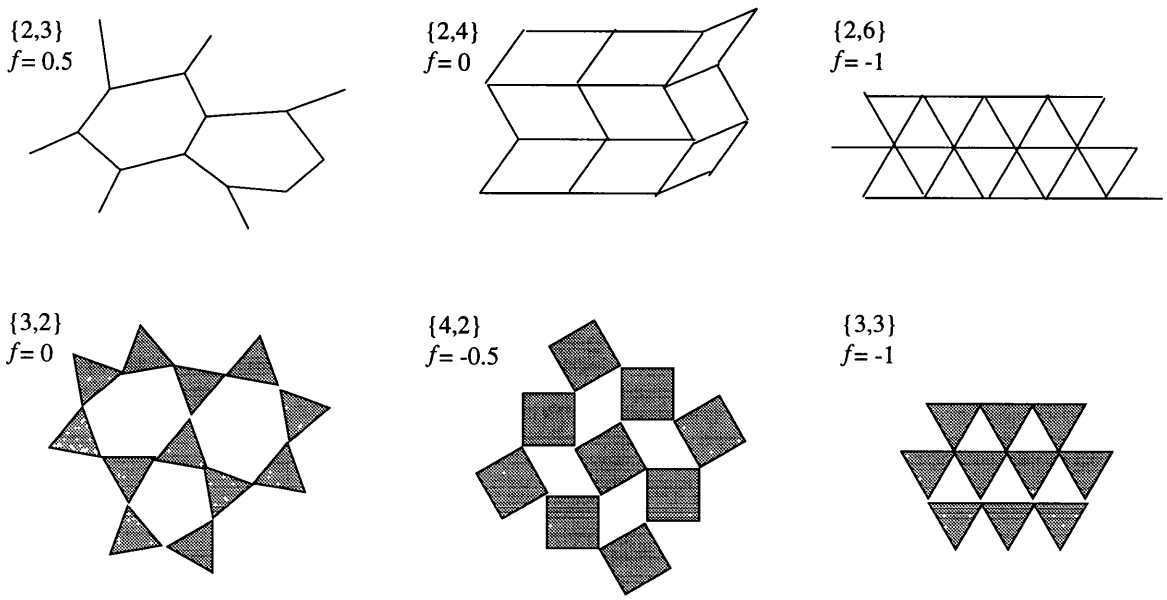

Figure 2.2: Two-dimensional networks constructed using one– and two–dimensional structuring polytopes, with respective connectivities and structural freedoms indicated.

where δ is the dimensionality of the structuring polytope itself, Y is the fraction of edge-sharing vertices and Z is the fraction of vertices sharing p-sided faces. Values of f associated with the simple two-dimensional structures illustrated are indicated in Figure 2.2. In arrangements for which $f < 0$, the number of constraints exceeds the degrees of freedom, and the structure is constrained to be crystalline; conversely, when $f > 0$, the structure is underconstrained, and extendible aperiodic arrangements can be propagated. When $f = 0$, a structure is exactly constrained and has excess freedom only at its peripheral boundaries. Connectivity is thus a *local* property whose consequences propagate to large distances.

Values of f calculated from Equation 2.1, or from a critical subset of the local connectivities as discussed below, for a wide range of ceramic structure types are listed in Table 2.1. Solids whose energetically favored short-range atomic arrangements yield $f \ll 0$ are overconstrained and therefore unlikely to form topologically disordered states from the melt or in rapid cooling of collision cascades; the redundant constraints are likewise difficult to remove in single displacement events or in the overlap of highly defective but still crystalline cascades. Solids whose preferred short-range atomic arrangements yield $f > 0$ are certain to be easily amorphizable, if indeed they can be crystallized to begin with, but are also likely to recover that crystallinity with minimal thermal activation at lower temperatures. Because too much freedom provides a means to reorder easily into lower-energy crystalline arrangements, structures with $f > 0$ are therefore more likely to retain amorphizability to higher temperatures.

Hobbs and Sreeram [58, 55, 63] have shown that a remarkable correlation exists be-

tween these calculated structural freedoms and the collisional damage energy expended per atom (as calculated from TRIM codes [143] for the ion, ion energy, target involved, and the measured critical ion fluence) required for ion-irradiation-induced amorphization in simple ceramic structures. The damage energy was taken to be the energy deposited by the primary ion into primary knock-on atoms less the losses to ionization and phonons in the subsequent collision cascades. The correlation should, of course, more properly be made with the critical number of displacements per atom (dpa), but because displacement thresholds are only poorly known for most ceramic compounds the critical collisional energy expended on displacements is at least the more calculable quantity. Many authors quoting critical amorphization thresholds in dpa regrettably omit mentioning the displacement energy assumed. The damage energy expenditure figure calculated from TRIM is fortunately relatively insensitive to choice of displacement energy in the code.

The present contribution integrates the earlier compilations with further data which have come available more recently, particularly on more complex structures, and from the behavioral trends established attempts to identify the critical structural features which govern the susceptibility to amorphization.

2.3 Simple compact structures

MgO (rocksalt), $MgAl_2O_4$ (spinel), UO_2 (fluorite), Al_2O_3 (corundum) and TiO_2 (rutile) represent the major classes of what could be called *compact* ceramic structure types. In these structures, the structuring polytopes are typically larger units (octahedra, cubes) with large number of vertices (V = 6,8) and high-connectivity (C = 3-6), sharing edges and faces. The structures are therefore vastly overconstrained ($f < -4$) and amorphization, either from quenching of molten cascades or from progressive removal of constraints by single displacement events or critical overlap of highly-defective regions, is least likely. In fact, although ion-beam-induced amorphization has been reported in MgO [88] and α-Al_2O_3 [88], there are in both cases uncertain contributions from the implanted ion [144] or surface modifications [3], and for most practical purposes these highly-constrained structures are unamorphizable. Rock-salt structure halides cannot be amorphized at all by the single anion displacements (and subsequent secondary cation displacements [52]) effected by radiolysis, even to levels of thousands of dpa at liquid-helium temperatures [57]. Neither can CaF_2,, which is likewise susceptible to efficient radiolysis [56, 131], and UO_2 has yet to be amorphized by ion irradiation at low temperature [127]. The coordination propensities determined by the highly ionic bonding tenaciously constrain these structures to crystalline states, as in the two-dimensional {2,6} or {4,2} connectivities illustrated in Figure 2.2.

The redundancy of constraints in close-packed metals similarly discourages amorphization. The $f = -3$ value calculated for a three-dimensional {2,12} structure is certainly an *over*estimate, because steric packing considerations additionally constrain the permissible angular distributions of the twelve interatomic vectors; the same is true of lower-coordinated body-centered cubic metals ($f < -1$). In fact, an amorphous phase in metallic glasses can be sustained only with the addition of additional stabilizing elements, e.g. P in otherwise b.c.c. Fe and Si in otherwise f.c.c. Ni [134].

The spinel structure, in contrast to the simpler rocksalt, fluorite and corundum structures, has two distinguishable cation sites and two distinguishable structuring polytopes, octahedra and tetrahedra. Its conventional radiation resistance [31] derives from that structural complexity, its chemical complexity (six atoms in a stoichiometric unit), and large unit cell (56 atoms), but its resistance to amorphization arises from the considerable structural redundancy in its backbone of structuring octahedra, half of whose edges are shared. Both $MgAl_2O_4$ [141, 141] and $(Fe,Mg)(Cr,Al)_2O_4$ [126] oxide spinels have nevertheless been amorphized at low temperature, the latter at least under conditions where influence of an implanted ion is minimal. Displacement-induced cation chemical disorder [15, 109] distributed over the normally-allowed cation sites (and even the large number of interstitial sites available to cations) appears to lead progressively to significant distortion of the close-packed oxygen sublattice framework and removes many or even all symmetry elements [140]; thus, it is possible that the amorphized structure retains a *topologically* ordered oxygen sublattice without necessarily retaining long-range spatial correlations.

2.4 Multiple polytope structures

Most other multi-cation ceramic structures are considerably more susceptible to amorphization than spinels [124], suggesting that complexity alone is not a reliable indicator of resistance to amorphization. In fact, not all the structural complexity may be relevant to the possibility of restructuring, and only certain structural elements may need to participate. But which elements are critically important? The measured relative ease of amorphization can provide a clue.

A good example is the surprisingly amorphizable [103] perovskite structure of $CaTiO_3$, which comprises a cage of corner-sharing$[TiO_6]$ octahedra into which large Ca^{2+} ions are inserted. The 12-coordinated Ca^{2+} ions form $[CaO_12]$ truncated cubes which share edges with the $[TiO_6]$ octahedra, contributing an apparent high degree of constraint. The $[TiO_6]$ octahedra alone, as in the ReO_3 structure, contribute a modest structural freedom, $f = -1$, which in fact correlates quite well with the relative ease of amorphizability of perovskites.

We therefore suggest that the corner-sharing octahedra constitute a critical *weak link* for amorphization, and that the large $V = 12$ coordination units are less important in policing structural stability. The latter must have at least a steric influence, so the effective structural freedom of $CaTiO_3$ is indicated as somewhat less than that of ReO_3.

Similar considerations apply to the $[ZrO_8]$ dodecahedra in zircon, $ZrSiO_4$, which are held together by edge-sharing $[SiO_4]$ tetrahedra. The structural freedom of zircon, as indicated by its even easier amorphization [125] in Table 2.1, indeed appears to be determined by the $[SiO_4]$ tetrahedra linkages. Zirconolite, $(CaZr)Ti_2O_7$, one of three components of the SYNROC formulation for proposed long-term storage of high-level radioactive waste [29], amorphizes even more readily [73]. In this complex structure, the Ca and Zr (and actinide) ions, with their larger coordination polyhedra, occupy sites between sheets of corner-sharing $[TiO_6]$ octahedra; the latter, again as in $CaTiO_3$, appear to serve as the weak link in structural reorganization. Wollasonite ($CaSiO_3$) presents an analogous situation in a still more amorphizable structure, in which chains of edge-sharing octahedra are are linked together by $[SiO_4]$ tetrahedra which share only corners with each other, accounting for an amorphizability similar to that of exclusively corner-sharing structures.

The distinguishing structural feature of oxide spinels, and of their eventual amorphization, is the cation occupation of tetrahedral and octahedral sites in the cubic close-packed arrangement of oxygen anions. All O^{2-} anions are equivalent, each being part of 3 octahedra and 1 tetrahedron; each O is also part of three critical shared edges, and local removal of oxygen eliminates shared edges. Removal of an O anion removes one of these shared edges. The $[MO_4]$ tetrahedra are isolated from each other and share only corners with $[MO_6]$ octahedra in [4,4] connectivity; the associated partial structural freedom is $f = -3$. The $[MO_6]$ octahedra, with half their edges shared (Y_0 = 12), expectedly contribute most to structural redundancy, with an associated partial structural freedom $f = -5.5$. A simple population-weighted average for both tetrahedral and octahedral structural elements yields an overall structural freedom $f = -4.7$, appropriate to its relative amorphizability in Table 2.1.

Forsterite, Mg_2SiO_4, which has the olivine structure (a hexagonal analogue of the cubic spinels) is nearly two orders of magnitude easier to amorphize than its cubic counterparts [28]. This structure introduces the additional complication that its $[SiO_4]$ tetrahedral polytopes, which are also isolated from each other, share three out of their six edges and one corner with chains of $[MgO_6]$ octahedra. These octahedra, as in spinel, share half of their edges, and their O vertices are again connected to 3 octahedra and 1 tetrahedron, yielding an overall structural freedom $f = -4.8$, globally about equivalent to spinel. Removal of the tetrahedral Si atoms yields octahedron connectivity $\{6,3\}$, but reduces the fraction of shared edges Y_0 from 1/2 to 1/3, raising f to -3.33, still only slightly higher than for spinel with tetrahedra similarly removed. Unlike spinel, the O anions are not all equivalent: 1/4 of

them are part of three structurally-critical shared octahedron edges, while the remaining 3/4 are part of only one shared octahedron-octahedron edge and two less critical tetrahedron-octahedron edges. Removal of the former, which comprise only 1/4 of the O complement, thus destroys 3/4 of the critical octahedron-octahedron edge sharing. and this inhomogeneous distribution of these structural elements provides the first clue to the susceptibility of the olivine structure to amorphization.

In spinel and olivine, the same fraction of polytope edges is edge-shared, which explains the failure of a single *globally* averaged value of structural freedom to predict the large observed difference in amorphizability. What is very different in the two structures is the *spatial distribution* of the structural constraints, in this case edge sharing, a difference most easily revealed by a graph-theoretical approach.

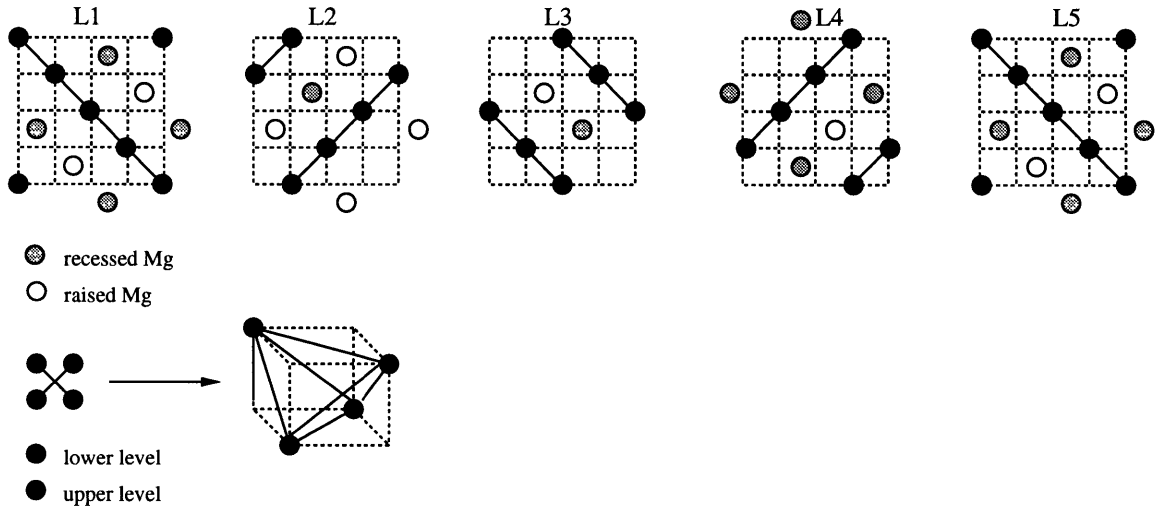

Figure 2.3: This is a layered representation of the dual structure of spinel. An edge exists between two polyhedral centers when they share an edge in the original structure.

Constraint counting in this case is not a strong enough measure to account for the wide difference in amorphizability between the two network structures. We offer a very different analysis which seems to give more insight into the real discrepancy. If we represent each tetrahedron and octahedron by a node and connect the nodes wherever there is edge sharing of adjacent polyhedra (note that there can be multiple edges shared, and therefore, this describes a multigraph), we see in this representation that in spinel, while the tetrahedron nodes remain isolated, the octahedron nodes form a strongly connected graph. Even removal of *all* tetrahedral cations still leaves a rigid $\{6,3\}$-connected network of octahedra intact, without disturbing the edge-sharing of half the octahedron edges, with a remanent structural freedom $f = -3.5$ (see Figure 2.3). For olivine, on the other hand, the analogous edge-sharing graph is highly disconnected. There are two orientations for octahedra (compared to spinel, in which there is only one), which occur in alternating blocks, and the border

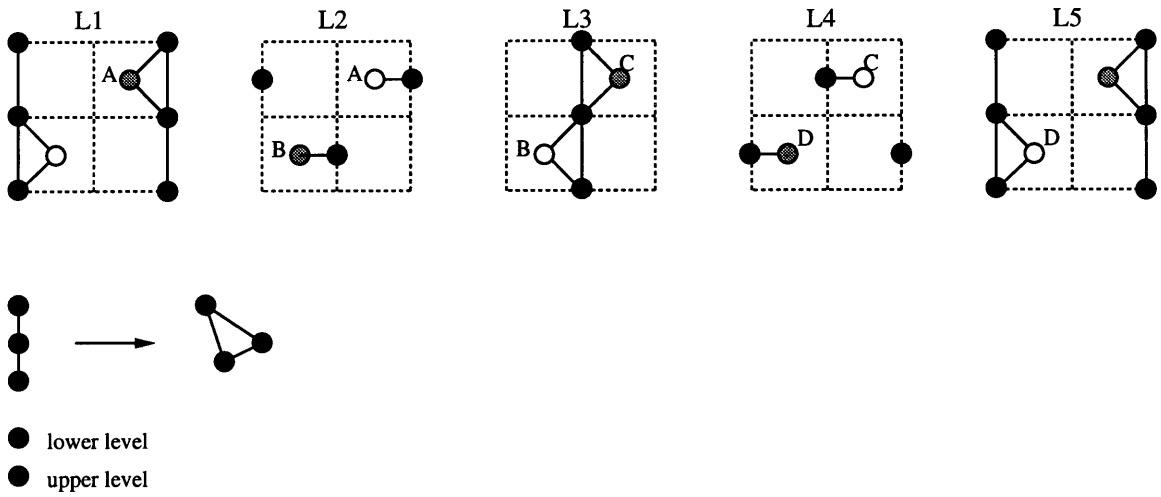

Figure 2.4: A layered representation of the dual structure of olivine.

octahedra are connected to the next block only through corner sharing (see Figure 2.4). By breaking only corner-shared connections, the olivine structure can be disconnected; thus, there are *planes* of structural weakness between the octahedral blocks. We therefore suggest that these planes of *corner*-shared linkages provide the weak link for amorphization, and an effective *local* value of f closer to that for other exclusively corner-sharing networks.

Ewing *et al.* [28] have compared the amorphization behavior of Fe_2SiO_4 in both its spinel and olivine polymorphs with the result that the g spinel form is actually slightly *more* amorphizable than the α olivine form. The spinel polymorph was synthesized under pressure and is unstable with respect to the olivine structure. What the experiment thus illuminates is that, in enumerating the structuring elements on which to evaluate structural freedom, it is the *preferred* bonding arrangements which are relevant. We also speculate that under disordering irradiation a solid will move towards that structural alternative with the *greater* structural freedom.

2.5 Network structures

It has for some time been known that more open network structures are more susceptible to amorphization [25] and that the susceptibility correlates with decreasing ionicity [10]. Coordination involving directed covalent bonds is, of course, lower than that about highly charged ions, so the real arbiter is not density or bonding but, again, structural freedom through more positive values of f as connectivity decreases. The archetypal covalent compound cited is SiO_2 which, in all crystalline and aperiodic forms but one high-pressure poly-

morph, comprises extended three-dimensional networks of corner-sharing [SiO_4] tetrahedra, for which arrangements $f = 0$. The combinatorial geometry of such tetrahedral networks has been explored by Marians and Hobbs [54, 55, 81, 80], who have shown they can be characterized by a single one-dimensional parameter, the primitive ring. The structures of network silicas are dominated by 6-rings for higher-temperature polymorphs like cristobalite, tridymite, and vitreous silica; and by 8- and larger rings for lower-temperature polymorphs like quartz. SiO_2 is easily amorphizable by neutrons, ions, post-threshold electrons and radiolysis at a displacement dose equivalent to about 0.1 dpa.

$AlPO_4$ (berlinite) [8, 115] and Be_2SiO_4 (phenakite) [28] offer two multi-cation variants, berlinite being isostructural with the SiO_2 quartz polymorph and comprising a network dominated by 8-rings of alternating [AlO_4] and [PO_4] corner-sharing tetrahedra, and Be_2SiO_4 comprising 4– and 6–ring network arrangements of [SiO_4] and [BeO_4] corner-sharing tetrahedra. $AlPO_4$ (which also radiolyzes, and more efficiently than silicas [8, 115]) and Be_2SiO_4 are scarcely less susceptible to ion-irradiation-induced amorphization than is quartz, we surmise because of their common $\{4,2\}$ connectivity and $f = 0$ structural freedom. It is revealing to compare phenakite with olivine-structure Mg_2SiO_4 in which tetrahedra share edges as well as corners with other structural elements. As expected from consideration of its greater structural freedom, Be_2SiO_4 is easier to amorphize, but it also recovers more readily in higher temperature irradiations [28]; this more facile recovery is also consistent with its greater structural freedom.

B_2O_3, which comprises corner-sharing [BO_3] *triangles* with $\{3,2\}$ connectivity, exhibits considerably more freedom than such corner-sharing tetrahedral networks ($\{3,2\}$ networks in *two* dimensions have $f = 0$, as seen in Figure 2.2, and in three dimensions have one degree of freedom more). It is, however–like the $\{2,2\}$ two-dimensional network in Figure 2.2—so *un*constrained that it does not crystallize (presumably because of the entropic contribution to the free energy), although crystal-like [B_3O_6] boroxyl 3-rings appear to comprise more than 70% of the structure [45].

Graphite is, effectively, another two-dimensional network, comprising sheets of carbon atoms which are 3-connected. The $\{3,2\}$ connectivity listed in Table 2.1 requires some explanation. As for elemental metals, one could describe this elemental structure with one-dimensional rod polytopes, in this case with $\{2,3\}$ in-sheet connectivity and $f = +0.5$; but the sp^2 hydrid bonding orbitals require a 120° C-C-C bonding angle which provides an additional constraint. This constraint can be better accounted for by considering instead a triangular structuring polytope centered on a C atom with vertices at the bond mid-points; the connectivity of this polytope is thus $\{3,2\}$, like B_2O_3, which in the two-dimensional sheets yields $f = 0$. The measured amorphizability of graphite (15 eV/atom [1]) falls only just above that of other $f = 0$ solids; the added three-dimensional constraint of the weaker

bonding between two-dimensional sheets would be expected to reduce the structural freedom slightly, and the amorphizability with it as observed. Silicon is the three-dimensional elemental analogue, which could be described as a {2,4} network of rod polytopes (with $f = +1$), but the strong tetrahedral sp^3 bonding makes non-coordination tetrahedra centered on the Si atoms with vertices at bond midpoint the appropriate choice to account accurately for the bond-angle constraints. The resulting {4,2} connectivity yields $f = 0$, in keeping with the observed [78, 79] amorphizability.

P_2O_5, comprising corner-sharing networks of $[PO_4]$ tetrahedra, exhibits less freedom than other tetrahedral networks, because only *three* of the four tetrahedron corners are shared, so the average connectivity is only C = 1.75. P_2O_5 is an inconveniently deliquescent solid, but lead pyrophosphate, $Pb_2P_2O_7$ ($2PbO{\cdot}P_2O_5$), retains the same {4,1.75} $[PO_4]$ connectivity, is a facile glass former, and can be grown as stable micaceous crystals. The crystalline form amorphizes [116, 117, 105] an order of magnitude more easily than fully-connected tetrahedral networks like SiO_2 and $AlPO_4$, which is entirely consistent with the reduced connectivity, but also suggests that the presence of the Pb ions, which coordinate as $[PbO_8]$ and $[PbO_9]$ polyhedra [94], has minimal influence on the amorphizability. As with $CaTiO_3$ or $CaSiO_3$, the connectivity of the smaller polytope appears ultimately to govern the overall structural freedom.

Si_3N_4 and SiC complete the discussion of network structures. While each compound exhibits two polymorphs, all feature connected tetrahedra, $[SiN_4]$ and $[SiC_4]$ (or $[CSi_4]$) respectively, which are connected three to a vertex in Si_3N_4 and four to a vertex in SiC. The additional tetrahedron in the {4,3} connectivity of silicon nitride compared to the {4,2} connectivity of silica adds significant constraint ($f = -1.5$), and Si_3N_4 has not been able to be amorphized for ion fluences corresponding to damage energies at least as high as 700 eV/atom [144] in the absence of implanted ions. By this logic, {4,4} SiC ($f = -3$) should be extremely difficult to amorphize, but in fact it amorphizes easily, by ion irradiation below about 400 K [113, 133] and fast electron irradiation below room temperature [65, 85, 66, 64], with only about five times more difficulty than for $f = 0$ structure types.

There are two possible explanations for this apparent delinquency from topological imperative: 1) the structure is especially vulnerable to displacement of a vertex atom (all atoms in the structure can be considered vertex atoms in one representation or another), four tetrahedral polytopes being destroyed in a single displacement event; and 2) the possibility of antisite disorder in displacement cascades removes the distinguishability of Si and C, so that the *average* topology becomes that of the Si structure (and for β-SiC exactly the Si structure). The first possibility must occur in Si_3N_4 as well, but without apparent effect. The second is supported by recent simulations [19] which suggest that antisite defects (about twice as common on the C sublattice as on the Si sublattice) are by an order of magnitude

the most common defect present in the cascade; anti-site disorder has been implicated already in electron irradiation-induced amorphization of SiC [113, 133]. SiO_2 in its cristobalite polymorph is but a decoration of the Si structure (O atoms at bond mid-points) and β-SiC a substituted silicon, so one might intuitively suppose that such a family resemblance would extend as well to structural freedoms. The fact that SiC is amorphizable only below 400 K suggests that the calculated $\{4,3\}$ $f = -3$ connectivity is still the governing one outside the collision cascade and as antisite defects anneal within it, so that the enhanced resistance to amorphization at higher temperatures is in this case due to the serious topological overconstraint, rather than to facile recovery arising from fewer constraints.

2.6 Discussion about amorphizability results

A topological assessment of structural freedom appears to serve as a surprisingly accurate criterion for amorphizability over a wide range of ceramic structure types, so much so that assessment is highly predictive and the anomalies noted–in graphite, Si, Mg_2SiO_4 and SiC—call attention to singular structural constraints or special irradiation features: the importance of angular constraints in bonding orbitals, the special weakness of critically-distributed corner sharing, the implication of high antisite inventory. In structures exhibiting multiple cation environments, it is possible on this basis to identify weak links representing increased local structural freedom and controlling the susceptibility to amorphization. A more quantitative estimate of amorphizability for structures exhibiting such heterogeneously distributed connectivities can be supplied using a network fault tolerance approach, which we are presently pursuing. Structural topology is thus a principal arbiter of the propensity for amorphization, affecting both restructuring of initial disorder following a thermal spike or cascade overlap and the dynamic recovery of crystallinity during higher-temperature irradiations. The (smaller) variations of amorphizability with compositional changes in the same structure are as likely to be attributable to corresponding changes in displacement thresholds and damage cross sections as to modification of structural parameters, and the amorphizability of polymorphic compositions appears to be governed by the structural topology of the more stable polymorph.

Structure	Polyhedra : sharing	{V, C}	f	Amorphization dose (eV/atom)[a]
MgO	Octahedra : edges	{6,6}	-10	5000 [88]
UO_2	Cubes : edges	{8,4}	-7	> 3000 [127]
α-Al_2O_3	Octahedra : faces, edges	{6,4}	-6.25	3400 [88]
$MgAl_2O_4$	Octahedra : edges; tetrahedra : corners	{4,4} {6,4}	-4.7	1600 [140]
TiO_2	Octahedra : edges, corners	{6,3}	-4	[b]
c.p. metal	Rods : ends	{2,12}	<-3	[b]
SiC	Tetrahedra : corners	{4,4}	-3	16 [94]
Si_3N_4	Tetrahedra : corners	{4,3}	-1.5	>700 [144]
$CaTiO_3$	Octahedra : corners[c]	{6,2}[c]	<-1	66 [103]
ReO_3	Octahedra : corners	{6,2}	-1	[b]
b.c. metal	Rods : ends	{2,8}	<-1	[b]
Mg2SiO4	Octahedra : edges; tetrahedra : edges, corners[c]	{6,4} {4,4}	-4.8[c]	38 [28]
$ZrSiO_4$	Dodecahedra : edges; tetrahedra : edges[c]	{4, 2.5}[c]	<-0.75[c]	36 [125]
$CaZrTi_2O_7$	Octahedra : corners[c]	{6,2.67}[c]	<-0.33[c]	30 [73]
SiC	*Tetrahedra : corners*	{4,2}	< 0	*16* [94]
C (graphite)	*Triangles : corners*	{3,2}	< 0	*15* [1]
$CaSiO_3$	Octahedra : edges; tetrahedra : corners[c]	{4,2}[c]	< 0	11 [25]
Be_2SiO_4	Tetrahedra : corners	{4,2}	0	11 [28]
Si	*Tetrahedra : corners*	{4,2}	0	*11* [78]
$AlPO_4$	Tetrahedra : corners	{4,2}	0	10 [115]
SiO_2	Tetrahedra : corners	{4,2}	0	7 [25]
Si	Rods : ends	{2,4}	< +1	11 [78]
$Pb_2P_2O_7$	Tetrahedra : corners[c]	{4, 1.75}[c]	< +0.38[c]	< 0.5 [105]
P_2O_5	Tetrahedra : corners	{4, 1.75}	+0.38	[b]
B_2O_3	Triangles : corners	{3,2}	+1	[b]

[a] Low-temperature values of critical energy density required for amorphization.

[b] Not measured.

[c] Weak-link connectivity.

Italicized entries based on atom-centered polytopes which are not coordination polyhedra.

Table 2.1: Coordination, connectivity, structural freedom and amorphizability for some common structures

Chapter 3

Local rules based theory for modeling crystal growth

Berger *et al.* [5] develop modeling exercises for the very analogous case of self-assembly of proteins into virus shells according to local structural rules and using simple energy minimization routines. Many viral shells appear to assemble with only limited aid from cellular machinery: they seem to "self-assemble" or spontaneously polymerize and take shape in the host cell environment. Attempts have been made to explain the assembly based on the icosahedral symmetry, focusing on assembly of protein subunits which form hexamer and pentamer building blocks with very similar neighborhoods, but some experiments have revealed that assembly does not take place by this route and that the focus on the final symmetry has in fact impeded understanding how the proteins really assemble into complex structures. The approach has been, instead, to consider what an individual protein "knows" from an information-theoretical point of view: it might appear that each protein needs to know something about the global structure, but in fact if the proteins assume different conformations during the assembly process depending on their relative positions, each protein has enough local information to "know" where to bond. Thus a protein needs to know nothing about what is going on in the rest of the structure in order to form icosahedral shells; a combinatorial set of local rules can explain the assembly of any icosahedral virus. In fact, for each virus structure there is a set of local rules which, starting with a single interaction between two proteins, uniquely determines all the other interactions necessary to assemble the entire structure.

We have adopted a similar local rules-based approach for rapid self-assembly of crystal structures and adapted many of the codes developed for self-assembly of virus shells, using tetrahedra as the building blocks instead of protein units, with several modifications.

The research reported in this chapter is joint work with Bonnie Berger, Linn Hobbs and Vinay Pulim, and was first published in [72].

Whereas virus-shell formation requires that proteins form a basically spherical shell (with topologically two-dimensional rules governing assembly), we have to provide rules governing connections in three dimensions. On the other hand, the surface is closed in three dimensions and does not have to be initially constrained to be so. (Concurrent work [106] has rendered the virus shell codes similarly more adaptable for general final conformations and general assembly subunits.) Unlike the bounded virus shell which is all surface, topologically three-dimensional structure models need to be large enough that surface properties do not dominate. In Section 4.1 we define the local cluster of a tetrahedron node; if we consider any node whose local cluster intersects the surface (and thus includes underbound nodes) as comprising part of the surface [84], then in structures such as quartz (with 63 nodes in the local cluster) quite large structural models are required. By this definition, a 1000-tetrahedron model of quartz would comprise 78% surface and clearly needs to be larger–well beyond the bounds of convenient hand modeling.

3.1 Local rules for self-assembly of tetrahedral networks

We first explain how to generate a set of rules governing the self-assembly of a tetrahedral crystalline network and how simulated growth of the crystal is effected using these rules. The approach is applicable to other than network structures, with coordination polyhedra other than tetrahedra, but the treatment here will confine itself to tetrahedral networks germane to [4,n]-connected silicas (where $n = 2, 3, 4$). The rules provide instructions of the following sort:

- **Number of types.** This instruction informs the simulator how many types of inequivalent tetrahedra exist; each type, while still geometrically identical to all other tetrahedra, follows its own set of rules. It is sometimes convenient to identify more than one of type when, in fact, all tetrahedra are topologically identical, for example when chirality is present or because it is easier to conceptualize the self-assembly with more types.

- **Connectivity.** This instruction defines the type of polyhedron in terms of the number of vertices (in this case "4" for a tetrahedron) and the number of additional polyhedra connected per vertex (in this case "1", "2", or "3" for O, N, and C respectively).

- **Orientation of the initial node.** We define arbitrarily a canonical orientation of the regular tetrahedron, inscribed in a unit cube centered at the origin, with vertices des-

ignated 0,1,2,3 at the four cube corners defined by Cartesian coordinate vectors [-0.5, -0.5, 0.5], [-0.5, 0.5, -0.5], [0.5, 0.5, 0.5] and [0.5, -0.5, -0.5] (see Figure 3.1). A rotation is applied to this tetrahedron to define the orientation of the initial node, defined by rotations about the x, y, z axes of the unit cube.

- **Rules for each vertex.** For a given vertex, this instruction informs the simulator about the relative orientation and type of the neighboring tetrahedra to which this vertex connects, as well as the vertex designation of those neighbors whose vertices it then shares.

In summary, given an initial tetrahedron, we need to know the rules governing the interactions at each vertex. With vertex-sharing silicas, for instance, the rules for each vertex will dictate the position of one neighboring tetrahedron.

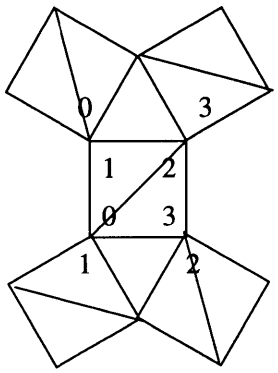


```
Quartz
1
4 1
REGULAR
;
0 1   z 60 ;
0 0   z -60 ;
0 3   z 60 ;
0 2   z -60 ;
```

$\theta = 155.6°$

Figure 3.1: Local rules for assembly of idealized quartz, depicting the canonical orientation of the initial tetrahedron and the assembly scheme for first five tetrahedra,with x-axis horizontal, y-axis vertical, z-axis orthogonal to the plane of the illustration.

Figure 3.1 illustrates a rules file for growing idealized quartz. The first line tells the simulator how many node types there are, where each node-type represents locally-identical tetrahedra (in this case, there is only one type (type "0"), because every tetrahedron in quartz follows identical rules). The second line gives the basic network connectivity; "4 1" signifies a structure in which each subunit has four vertices and each vertex seeks one neighbor (equivalently, two tetrahedra meet at each vertex). The third line indicates whether the polyhedron is regular (if it is not, we must additionally specify the initial coordinates of its vertices). The fourth line specifies any rotation applied to the initial canonical node resolved into rotations about x, y and z (in this case, there are none). The remaining lines specify rules for each vertex. The first of these provides rules for vertex 0 (in this case, vertex 0 is connected to a tetrahedron of type 0 at its vertex 1), and then the rotation applied to that

neighboring tetrahedron is explicitly given (in the example, vertex 0 is connected to vertex 1 rotated 60° around z).

How the simulator works

Given a rules file with a regular tetrahedron specified, the simulation begins with the initial node, inscribed in the unit cube and appropriately rotated, and looks for a vertex seeking a connection. A new tetrahedron is copied, rotated in accordance with the rules for that vertex, and translated so that its appropriate vertex presents to the vertex seeking the connection. For example, in Figure 3.1, the initial tetrahedron is unrotated from the canonical orientation and, for vertex 0 seeking a connection, a new tetrahedron is copied, rotated +60° about z, and translated so that its vertex 1 connects to vertex 0 of the initial tetrahedron. This process is then continued for each initial vertex and then for each added tetrahedron in turn serving as an initial tetrahedron. This process is an abstraction of what might occur chemically. We create the rules file to adhere to certain properties such as Si-X-Si bond angle and density. Simulations and their subsequent analyses were carried out for the most part on a Silicon Graphics Onyx work station incorporating an efficient graphical user interface which we developed specifically for the purpose. See Appendix A for details about the simulator.

3.2 Tetrahedral crystalline polymorphs and rules describing them

Having described the basis for the modeling simulation, we now describe the rules for six of the crystalline forms of silica–and remark in passing on the simplicity of each rules set. The language of local rules is constructive and at least as concise as a unit cell representation based on symmetries. This is obviously true since we could simply make a rules file with one type of node for each node in the unit cell (with connections as per the unit cell). The orientation of the initial node can be manipulated to replicate a specified Si-O-Si inter-tetrahedral angle θ (Section 3.3) or density (Section 3.4).

Before giving the rules, we offer a brief overview of how one creates a rules file and what techniques are often helpful. When there was no physical model to work with, I could derive most of the information needed from diagrams given in the literature ([47] is an example of a good source). Eventually, we would like to automate the rules generation process. Ideally, a space-group description could be converted to a rules set, and then one could modify the rules set to "play" with amorphous structures.

Quartz

We have already described the rules for ideal quartz in Figure 3.1. Those for α- and β-quartz are precisely the same except for an initial rotation. Rotating the initial tetrahedron about the y-axis between 0 and 47° generates the full range of Si-O-Si bond angles obtainable without underconnection ($155.6° > \theta > 123.3°$), only a portion of which is spanned by the α- ($\theta = 143.6°$, initial *y*-offset 24°) and β- ($\theta = 150.9°$, initial *y*-offset 14°) quartz forms. Figure 3.2 compares 200 nodes of the structures generated for ideal quartz and α-quartz. By changing the initial rotation and relabeling the vertices, we can also reverse the chirality of these crystal forms.

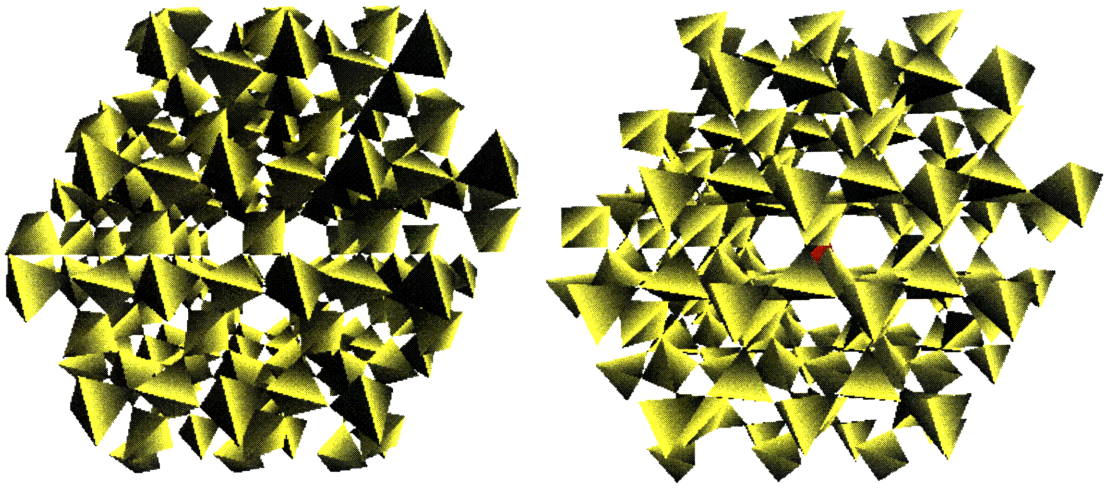

Figure 3.2: 200 nodes of (a) idealized quartz and (b) α-quartz, assembled according to the rules files in Figure 3.1, viewed along the c-axis 6-fold and 3-fold tunnels. The latter are obscured in α-quartz.

Cristobalite

High-temperature β-cristobalite and HP-tridymite are formally polytypic, consisting of similar planar sheets of 6-rings of tetrahedra alternating orientation up and down; these sheets are stacked ABCA in cristobalite and ABA in tridymite. For idealized cristobalite, for which the Si-O-Si bond angle is 180°, the initial node can be the canonical tetrahedron (Figure 3.3), with the offset rotation about *y* between 0 and 45° in the initial orientation, yielding the range of Si-O-Si angles between 180° and 109.5°. Initial offset about *y* by 23° yielded a version with $\theta = 148°$, close to that of actual β-cristobalite. The first rules file in Figure 3.3 should be compared to that for quartz, Figure 3.1, which differs only in the generation rotation angle (60° in quartz, 90° in cristobalite), though the resulting structures are vastly different crystallographically. To emphasize the planar 6-ring stacking, we can alternatively choose

an initial tetrahedron which lies flat on the *x*,*y* plane by offsetting the canonical orientation by -45° about *x*, nearly -145° about *y*, and 90° about *z*. The rules file in a second setting corresponding to this alternative initial offset is then shown in Figure 3.3, and 200 nodes of the structure generated by either rules set are reproduced in Figure 3.4.

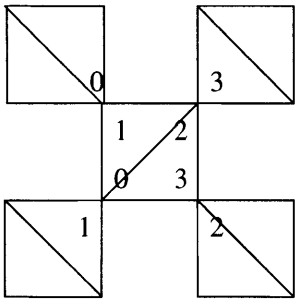


```
Cristobalite
1
4 1
REGULAR
;
0 1   z 90 ;
0 0   z -90 ;
0 3   z 90 ;
0 2   z -90 ;
```

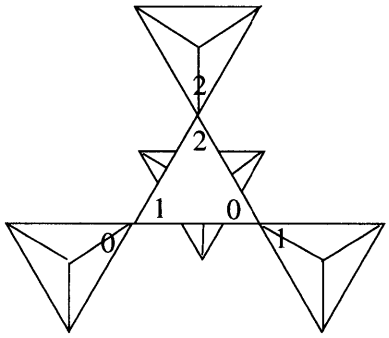


```
Cristobalite
1
4 1
REGULAR
x -45 y 35.2 z -90 ;
0 1   x 180 ;
0 0   x 180 ;
0 2   x 180 ;
0 3   x 180 ;
```

Figure 3.3: Two settings of the rules file for idealized cristobalite. The first setting, viewed along [100], begins with the initial tetrahedron in the canonical orientation and differs from the Figure 3.1 rules for quartz only in the 90° assembly rotations. The second setting, viewed along [111], emphasizes the planar stacking, as illustrated in the depicted assembly of the first five tetrahedra.

Tridymite

The rules file for idealized tridymite (Figure 3.5) is nearly the same as for idealized cristobalite, except that vertex 3 is connected to vertex 3 rotated 180° about *y* instead of about *x*. Vertex 3 is the vertex which connects the sheets in tridymite, and rotating 180° about *y* instead of *x* ensures that the orientation of consecutive sheet levels is inverted. One can visualize the difference by viewing down the c-axis and noticing (in comparing Figures 3.3 and 3.5) that, whereas for cristobalite the node connected to vertex 3 can be seen, in tridymite it cannot. 200 nodes of the idealized structure have been assembled in Figure 3.6.

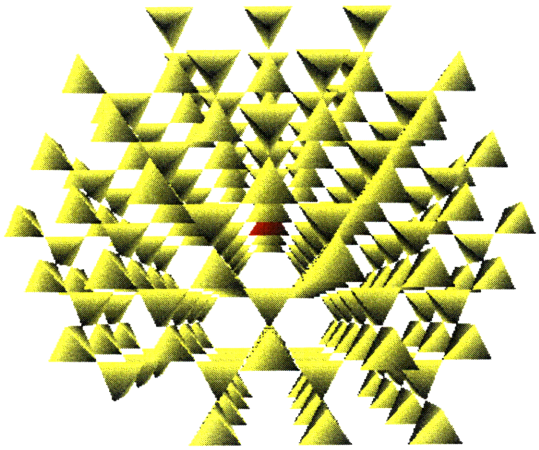

Figure 3.4: 200 nodes of idealized cristobalite, assembled according to either rules file in Figure 3.3 and viewed along [111].

A version closer to actual HP-tridymite can be generated by decreasing the initial tetrahedron offset about z from 90° to 68.1° (average $\theta = 149.5°$).

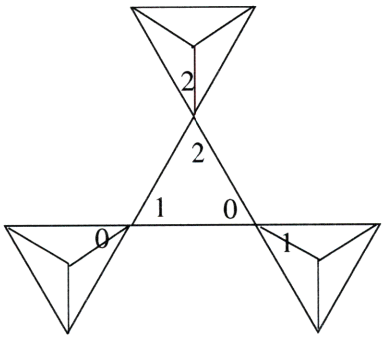


```
Tridymite
1
4 1
REGULAR
x -45 y 35.2 z -90 ;
0 1  x 180 ;
0 0  x 180 ;
0 2  x 180 ;
0 3  y 180 ;
```

Figure 3.5: Local rules for assembly of idealized tridymite, to be compared to the second setting of cristobalite rules in Figure 3.3. The depicted projection obscures the position of the fifth tetrahedron behind the initial tetrahedron.

Moganite

Moganite has been envisioned as alternating unit-cell slices of left- and right-handed quartz [47] and superficially resembles quartz. Topologically, it is quite distinct. There are two topologically inequivalent tetrahedron sites and four distinct tetrahedron orientations, but we have chosen to assemble the structure with six types in the rules file (Figure 3.7) to render the conceptualization easier. The rules for adding to each vertex may call for any of the six types, as stipulated in the first column of the last four lines of each rules set. For idealized

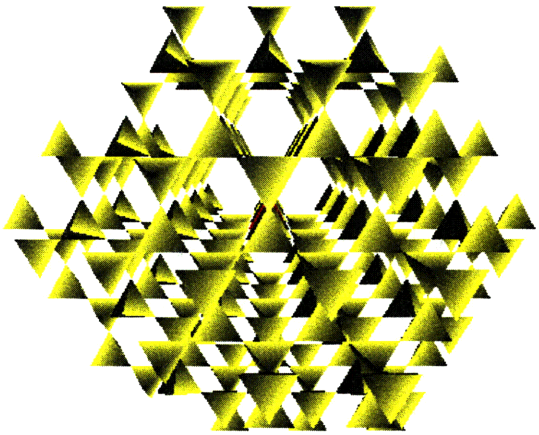

Figure 3.6: 200 nodes of idealized tridymite, assembled according to the rules file in Figure 3.5, viewed down the c axis.

moganite, the initial node orientations are the canonical one and one rotated 90° about x. We can additionally describe "β-" and "α-" moganite variants by using initial offset rotations for quartz of 14° and 24° respectively about y. Figure 3.8 shows 200 nodes of the idealized structure.

Keatite

Establishing rules to generate keatite proved significantly more difficult than for the other polymorphs. Keatite is unique among compact crystalline silica polymorphs in that it is composed of odd-size rings. (The open-framework clathrate silicas may also have odd rings to generate the curvature necessary to form their cages: [119]). Also, whereas quartz forms 3-fold and 6-fold spirals, keatite makes 4-fold spirals. Like moganite and coesite, there are two topologically-inequivalent tetrahedra, which we have chosen to model with three types in the assembly rules file (Figure 3.9). 200 nodes of the assembled structure are shown in Figure 3.10.

Coesite

Coesite is the densest vertex-sharing silica polymorph. Its structure consists of chains of 4-rings comprising two topologically distinct tetrahedra. The easiest way to formulate the assembly rules appears to require four node types, pairs of which are identical with respect to local topology and their local clusters. The major task presenting itself was to arrive at a simple set of rules to generate the chains of 4-rings, then to establish augmented rules leading to proper chain interconnection. The resulting rules file appears in Figure 3.11, and

200 nodes of the assembled structure in Figure 3.12.

SiC

The rules for silicon carbide require that each corner find three neighboring tetrahedra. For β-SiC there are actually no rotations necessary since every tetrahedron lies in the same relative orientation. Therefore, the rules for β-SiC which can be seen in Figure 3.13 are the simplest. Figure 3.14 illustrates a 200 tetrahedron model. For α-SiC, notice in Figure 3.15 that corner 3 (the connection between sheets) has its neighboring tetrahedra rotated 180° to get the two different orientations of tetrahedra. Figure 3.16 illustrates a 200 tetrahedra on model.

Silicon Nitride

β-Si_3N_4: It was surprising to discover that a crystal with a significantly larger unit cell needed only one node-type to define its rule set. These rules can be seen in Figure 3.17 with the corresponding assembly shown in Figure 3.18.
α-Si_3N_4: The rules to generate α-Si_3N_4 are more complicated than those for β-Si_3N_4. We have found that four node-types are needed to describe this particular topology. The rules for this structure are in Figure 3.19 with the corresponding assembly shown in Figure 3.20.

3.3 Bond-angle limitations for silica

The advantages of computer-based self-assembly over hand-built modeling are numerous and apparent. Apart from being faster and less cumbersome, the simulation automatically yields the complete adjacency matrix from which all topological information can be easily derived. Because the coordinates of all atoms in a given structure have been recorded, it is easy to compute and display bond-angle distributions and pair-correlation functions (also known as radial distribution function, this is the distribution of distances between pairs of atoms). The topology is also readily accessible, as pursued in Section 4.1. In particular, it is straightforward to explore the limits on bond angles within a given topology. The intra-tetrahedral O-Si-O bond angle is 109.5° unless the [SiO_4] tetrahedra distort, which is a consideration in ensuring connectivity in our models of amorphous silicas presented in Section 5.1. The energy of the inter-tetrahedral Si-O-Si bond angle θ is relatively invariant over the range $130° < \theta < 180°$ [104] which spans the topological units of 3-rings ($\theta = 130.5$ for three oxygens and three silicons in a plane) to the regular (but slightly puckered) 6-rings ($\theta = 180°$) of idealized β-cristobalite and HP-tridymite. Larger rings exhibit $\theta < 180°$, and

further puckering otherwise reduces θ. Table 3.1 lists the Si-O-Si angles resulting from our choice of rules files.

Polymorph	Node	Si-O-Si θ°	Ave Si-O-Si θ°	Model Density $\times 10^3 kg/m^3$
ideal-Cristobalite	0	180	180	1.92
β-Cristobalite	0	148	148	2.17
α-Cristobalite	0	145.3	145.3	2.33
ideal-Tridymite	0	180	180	1.92
HP-Tridymite	0	138.8 (3), 180	149.5	2.22
x-Tridymite	0	123.7 (3), 180	137.8	2.54
ideal-Quartz	0	155.6	155.6	2.37
β-Quartz	0	150.9	150.9	2.51
α-Quartz	0	143.6	143.6	2.77
Keatite	0	147.8, 150.5 (2), 164.0	154.6	2.61
	1	147.8 (2), 164.0 (2)		
ideal-Moganite	0	143.6	152.7	2.24
	1	180 (2), 143.6 (2)		
β-Moganite	0	139.8 (2), 146.5 (2)	149.5	2.39
	1	139.8, 148.5, 165.9 (2)		
α-Moganite	0	125.2 (2), 143.9 (2)	137.5	2.72
	1	125.2, 143.9, 146.3 (2)		
Coesite	0	140.9, 144.7, 148.9 (2)	150.8	2.82
	1	144.7, 148.9 (2), 180		
β-Si_3N_4	0	109.5, 120, 125.1×2	119.8	3.29
α-Si_3N_4	0	110.6, 114.2, 117.2, 118.1		
		118.2, 118.4, 119.6, 124.9		
	1	111.7, 113.1, 116.8, 120.3		
		120.6, 122.2, 123.0, 124.9	118.3	3.22
	2	110.5, 115.6, 116.9, 117.3		
		117.8, 117.8, 117.8, 124.8		
	3	111.7, 113.1, 117.1, 117.7		
		117.9, 118.4, 119.6, 124.5		
β-SiC	0	109.5	109.5	3.21
α-SiC	0	109.5	109.5	3.24

Table 3.1: Si-X-Si Angles and Densities for Rules-Generated Crystal Polymorphs

The topological limits on quartz deduced from our modeling are $123.9 < \theta < 155.6$. Experimentally, θ in β-quartz is somewhat less (150.9°) than the extremum and drops to 143.6° well below the $\alpha - \beta$ transition temperature [139]. For cristobalite, the topological limits are $109.5 < \theta < 180$. In tridymite, a structural distortion yielding all identical Si-O-Si angles $\theta < 180°$ (as in β-cristobalite, $\theta = 148°$) appears impossible to achieve; attempts

using initial offsets deviating by 10° about x and 17° about z from the idealized configuration yielded $\theta = 148°$ for all Si-O-Si bond angles and preserved tetrahedra but resulted in underconnection. Connectivity in our model of HP-tridymite was achieved by maintaining one Si-O-Si angle at $\theta = 180°$, while the applied offset rotation of 68.1° about z lowered the other three to $\theta = 138.8°$, resulting in an average ($\theta = 149.5°$) intended to replicate the measured average for actual HP-tridymite ($\theta = 149.2°$). An extreme tridymite version can be generated in the same way by decreasing the initial tetrahedron rotation about z still further to 60°, yielding the minimum Si-O-Si angle ($\theta = 123.8°$) obtainable without puckering of the sheets.

Keatite, moganite and coesite each exhibit several Si-O-Si angles; our model averages were $\theta = 154.6°, 152.7°$ and 150.5° respectively for the idealized forms. Moganite achieves one (physically unrealistic) minimum bond angle of $\theta = 92.6°$ as a limit at an inflection point of 47° offset about y (by inflection, it is meant that by altering the initial offset angle any further, the angle begins to increase again). The geometrical constraints in keatite appeared to preclude much latitude in the choice of initial node offset or consequent bond angles.

3.4 Density

Model densities are calculable from the the Si-O distance, the number of tetrahedra in the model, and the model structure volume. Two methods were employed. In the first, the volume of the convex hull (largest polyhedron with triangular faces containing all the nodes) of the entire model structure was determined by summing the volumes of the pyramids defined by each surface triangle and an interior point. This method consistently overestimated the volume for the model sizes used. In the second, a sphere somewhat smaller than the convex hull was centered randomly in turn on 10 interior nodes and the number of tetrahedra enclosed by the sphere in each case counted and averaged. With both methods, large models provide a more accurate measurement than smaller models because of the difficulty in calculating the volume contribution of tetrahedra lying near the spherical surface, and models comprising at least 1500 tetrahedra were employed for density determinations.

Model densities calculated by the second method, using an Si-O bond distance of 0.161 nm [36] for all models, are reported in Table 3.1. Our self-assembled model of β-quartz, with the initial offset chosen to replicate the observed Si-O-Si bond angle $\theta = 150.9°$, yielded a density of 2.51 g/cm^3 compared to the experimental value of 2.53. Our self-assembled model of α-quartz, with the initial offset chosen to replicate the observed Si-O-Si bond angle $\theta = 143.6°$, yielded a slightly higher density (2.77) than the experimental value (2.65). The density of our model of b-cristobalite with $\theta = 148°$ was only slightly smaller (2.17)

than the experimental value (2.21). The density of our HP-tridymite model (2.22) was also fortuitously close to the experimental value (2.18). Density was in all cases found to depend sensitively on initial offset; for example, the extreme version of tridymite, with an initial node offset only 8° greater about z than for our HP model, yielded a density of 2.54. To compute the density of the Si_3N_4 models we used bond length of 0.173 nm and found the density of the α-Si_3N_4 model to be 3.22 and the β-Si_3N_4 to be 3.19. For SiC we used a bond length of 0.188 nm to yield a density of 3.21 for the β-SiC model and 3.24 for the α-SiC model.

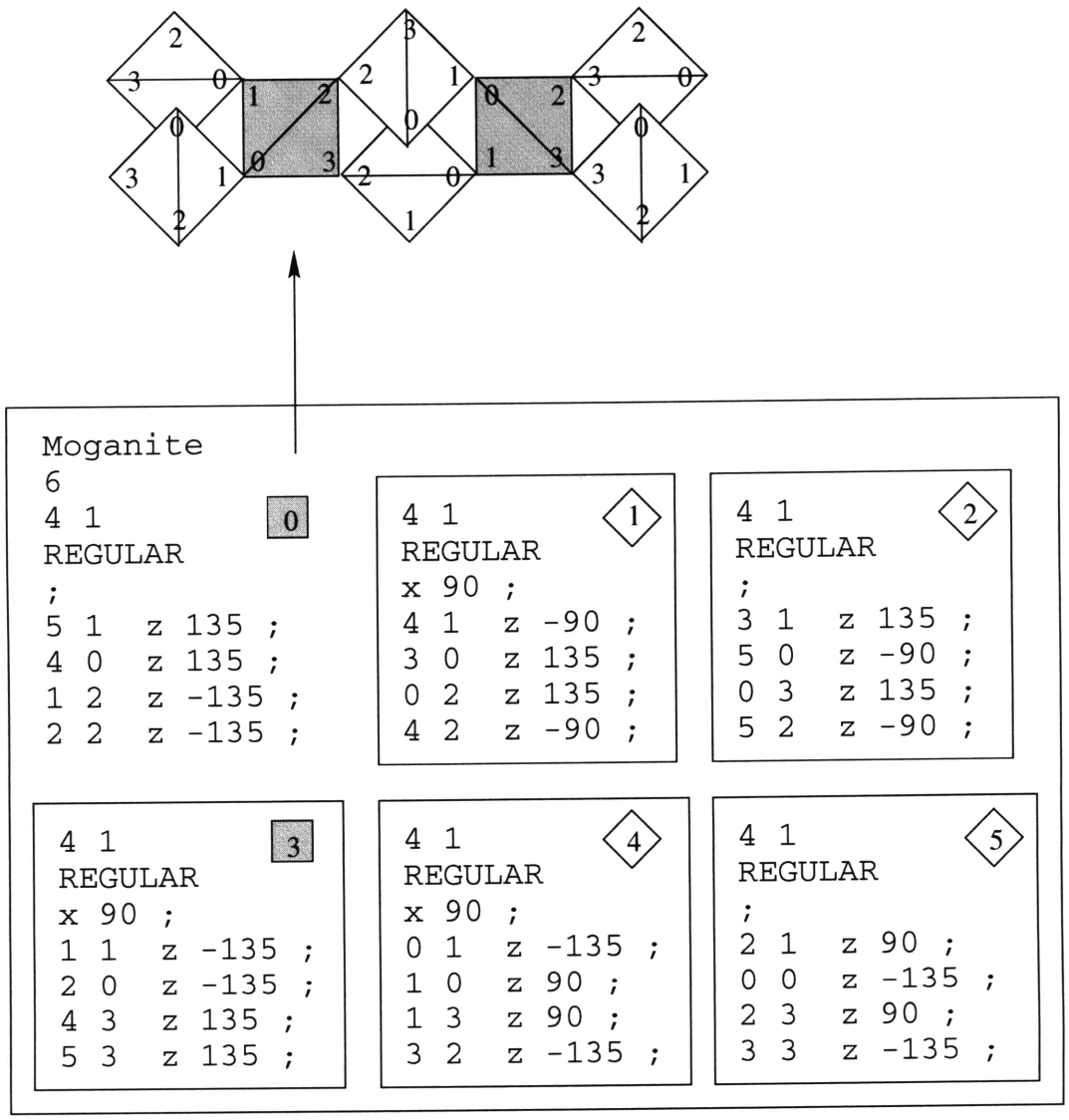

Figure 3.7: Local rules for assembly of idealized moganite using six node types corresponding to two inequivalent tetrahedron environments (shaded and unshaded). Two initial tetrahedron orientations are used, related by a 90° rotation about the horizontal x-axis.

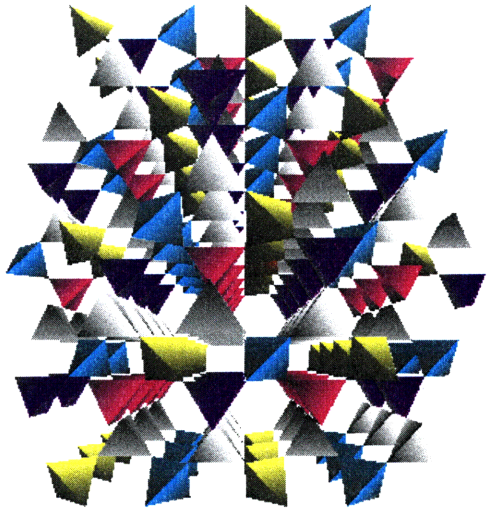

Figure 3.8: 200 nodes of idealized moganite, assembled according to the rules file in Figure 3.7 and viewed down the b axis, in which projection tunnels remain, whereas the c-axis tunnels analogous to quartz are blocked. The colors correspond to the six different node rules in the rules file.

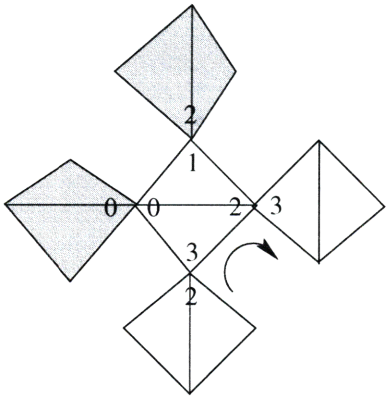


```
Keatite
3
4 1                    0
REGULAR
z 45 y -24 ;
1 0   z 180 ;
1 2   z 90 ;
0 3   z 90 ;
0 2   z -90 ;
```

```
4 1                    1
REGULAR
x -20 z 45 ;
0 0   z 180 ;
2 0   y 180 z 90 ;
0 1   z -90 ;
2 1   y 180 ;
```

```
4 1                    2
REGULAR
z 45 y -24 ;
1 1   z -90 y 180 ;
1 3   y 180 ;
2 3   z 90 ;
2 2   z -90 ;
```

Figure 3.9: Local rules for assembly of keatite, using three node types corresponding to two inequivalent tetrahedron environments (shaded, unshaded). The arrow represents a four-fold spiral out of the plane of the illustration.

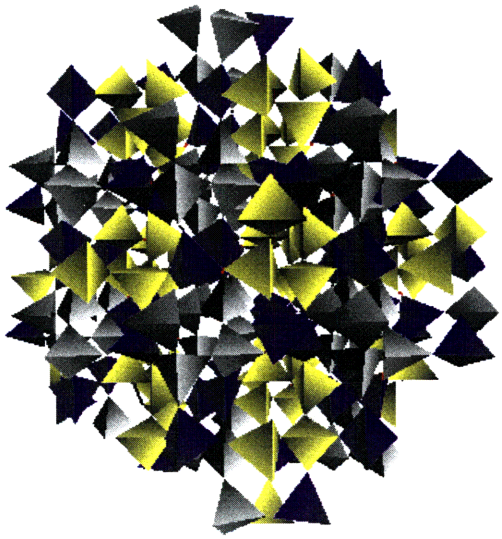

Figure 3.10: 200 nodes of keatite, assembled according to the rules file in Figure 3.9, viewed down the four-fold spiral. The three colors correspond to the three different node rules in the rules file.

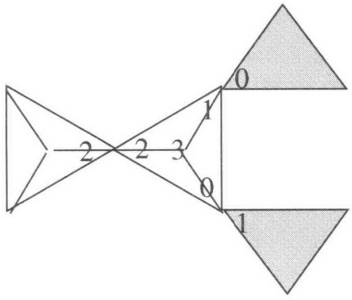


```
Coesite
2
4 1                                    0
REGULAR
x -45 y -138 ;
1 1   z -90 ;
1 0   z 90 ;
0 2   z 180 ;
3 3   z 90 ;
```

```
4 1                                    1
REGULAR
x -45 y 180 ;
0 1   z -90 ;
0 0   z 90 ;
3 2   z 180 ;
2 3   z -90 ;
```

```
4 1                                    2
REGULAR
x -45 y -138 x 180 ;
3 1   z 90 ;
3 0   z -90 ;
2 2   z 180 ;
1 3   z -90 ;
```

```
4 1                                    3
REGULAR
x -45 y 180 x 180 ;
2 1   z 90 ;
2 0   z -90 ;
1 2   z 180 ;
0 3   z -90 ;
```

Figure 3.11: Local rules for assembly of coesite, the densest [4,2]-connected network silica, using four node types corresponding to two inequivalent tetrahedron environments (shaded, unshaded).

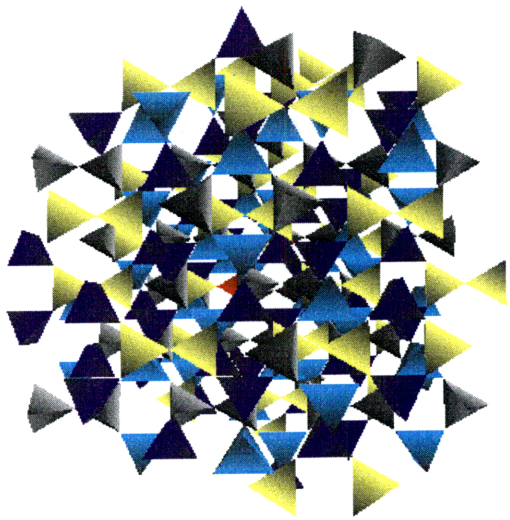

Figure 3.12: 200 nodes of coesite, assembled using the rules file in Figure 3.11. The four colors correspond to the four different nodes rules in the rules file. The planes containing the strings of 4-rings are parallel to the plane of the illustration.

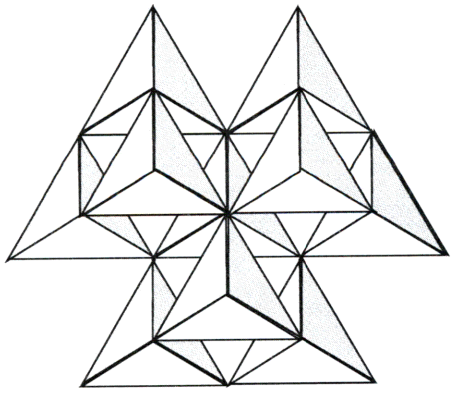

```
Beta-SiC
1
4 3
REGULAR
;
0 1  ;   0 2  ;   0 3  ;
0 0  ;   0 2  ;   0 3  ;
0 0  ;   0 1  ;   0 3  ;
0 0  ;   0 1  ;   0 2  ;
```

Figure 3.13: Local rules for assembly of β-SiC, the simplest [4,4]-connected network silicon compound

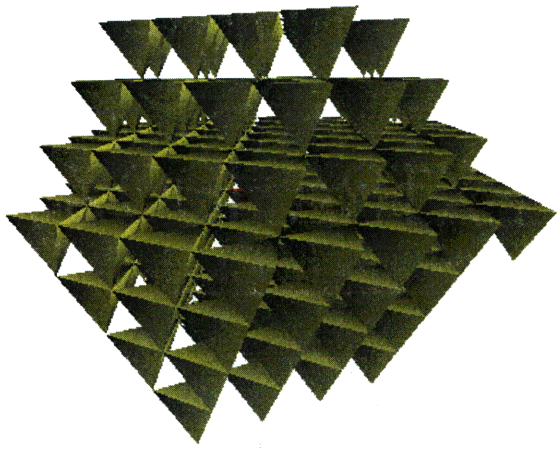

Figure 3.14: 200 nodes of β-SiC, assembled using the rules file in Figure 3.13.

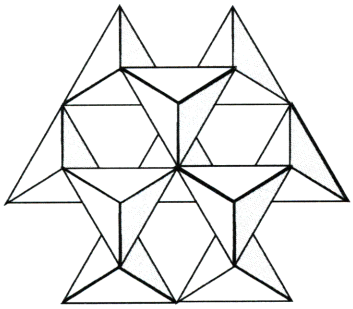

```
Alpha-SiC
1
4 3
REGULAR
x -45 y -144.8 z 90 ;
0 1       ;  0 2       ;  0 3   z 180 ;
0 0       ;  0 2       ;  0 3   z 180 ;
0 0       ;  0 1       ;  0 3   z 180 ;
0 0 z 180 ;  0 1 z 180 ;  0 2   z 180 ;
```

Figure 3.15: Local rules for assembly of α-SiC

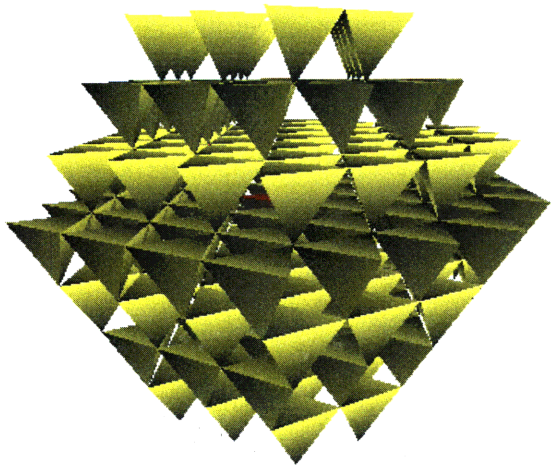

Figure 3.16: 200 nodes of α-SiC, assembled using the rules file in Figure 3.15.

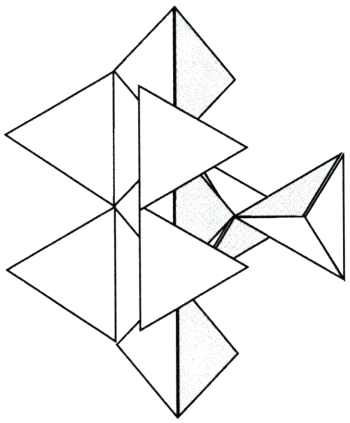

```
Beta-Si3N4
1
4 2
REGULAR
z 45 ;
0 1  y  60 ;   0 2  ;
0 0  y -60 ;   0 2  y  -60 ;
0 1  y  60 ;   0 0  ;
0 3  y 120 ;   0 3  y -120 ;
```

Figure 3.17: Local rules for assembly of β-Si_3N_4

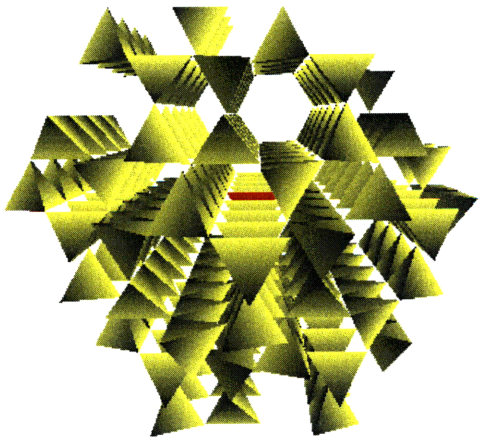

Figure 3.18: 200 nodes of β-Si_3N_4, assembled using the rules file in Figure 3.17.

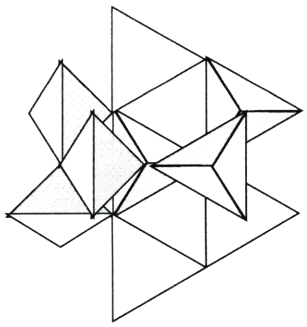

```
Alpha-Si3N4
4
4 2
REGULAR
x -45 y 29 ;
1 0  ;        2 2  y  -60 ;
1 1  ;        3 2  y   60 ;
2 0  y  60 ;  3 0  y  -60 ;
0 3  y 120 ;  0 3  y -120 ;
```

```
4 2
REGULAR
x -45 y 29 x 180 ;
0 0  ;        2 2  y  -60 ;
0 1  ;        3 2  y   60 ;
2 1  y  60 ;  3 1  y  -60 ;
1 3  y 120 ;  1 3  y -120 ;
```

```
4 2
REGULAR
x -45 y 29 x 180 ;
3 0 y -120 ;  0 2  y  -60 ;
1 1 y -120 ;  1 2  y  -60 ;
0 0  y  60 ;  1 0  y   60 ;
2 3  y 120 ;  2 3  y -120 ;
```

```
4 2
REGULAR
x -45 y 29 ;
2 0  y 120 ;  0 2  y   60 ;
2 1  y 120 ;  1 2  y   60 ;
0 1  y  60 ;  1 1  y  -60 ;
3 3  y 120 ;  3 3  y -120 ;
```

Figure 3.19: Local rules for assembly of α-Si_3N_4

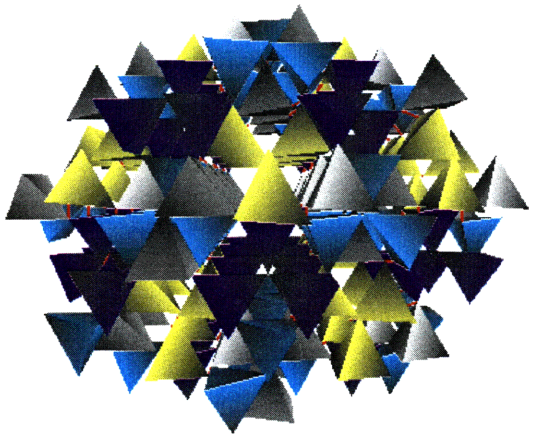

Figure 3.20: 200 nodes of α-Si_3N_4, assembled using the rules file in Figure 3.19.

Chapter 4

Analysis of the structures produced

The advantages to using computer hand modeling over hand modeling [82] are numerous. Aside from being faster and less cumbersome, the simulation automatically yields the adjacency matrix from which most analyses can be easily performed. Because we have recorded the coordinates of all the atoms in a given structure, we can easily compute bond angle distributions and pair-correlation functions. Another way to describe network structures is by analyzing the irreducible rings. However, often times ring distributions are not enough to differentiate structures, so we would like to get information about individual local clusters [82].

4.1 Rings and local clusters

With hand modeling, rings need to be identified by tedious inspection, and it is often difficult to ascertain if they are indeed primitive. Ring analysis can be carried out more efficiently and accurately by computer using ring-finding and testing algorithms. For hand modeling, these require first establishing connectivity tables for the models; for computer-based self-assembly, the adjacency matrix provides the connectivity information directly.

Global ring distributions are usually what are computed for glass structure models but are seldom adequate to describe the full topological properties of a given network and are not sufficient to differentiate structures; both tridymite and cristobalite contain only primitive 6-rings, for example. More useful is a description of the local topology provided by the set of tetrahedra associated with the primitive rings which pass through a given node (tetrahedron). We define this set as the local cluster of a tetrahedron [80].

The research reported in this chapter is joint work with Bonnie Berger, Linn Hobbs and Vinay Pulim. Some of the material first appeared in [72]. The other results on silica local clusters appeared in [61] and results for SiC and Si_3N_4 first appeared in [71]

4.2 Ring-finding algorithms

Three formal definitions are required in order to establish a consistent enumeration of network ring content; we use those of [80]. A *ring* is a connected sequence of either edges or tetrahedra (nodes); formally, a ring in a network is a closed path where each node on the path appears exactly once. For vertex-sharing tetrahedra, rings through the edges of the tetrahedra and rings through the center of the tetrahedra (nodes) are topologically equivalent; the former must be defined to exclude the tetrahedra themselves (*i.e.* no more than one edge of a tetrahedron can be part of a ring). A *local cluster* of a node n is the union of all nodes that are in some primitive ring of node n.

There are several different definitions extant for what we refer to as *primitive rings*, which has caused confusion in the literature. One definition often used is the following: given node n and a neighboring node m, for each neighbor k of node m, a primitive ring through n can be found by taking the shortest path (or paths, if there is more than one of that shortest length) between n and k which does not use m. Such rings have been called "minimal rings" by Guttman [44]. Marians' [82] definition is less restrictive and more inclusive: a ring in a network is primitive if at least one of the two paths between any pair of nodes of the ring is a minimal path. This is effectively the same definition adopted by Goetzke and Klein [38], although their their terminology differs from ours (they define as a "ring" what we call a primitive ring, and a "cycle" to be what we call, in general, a ring.)

The formal definition adopted for a primitive ring is constructive in that it yields directly the following simple approach to finding the local cluster. First, we enumerate all rings which include n. This enumeration can be achieved by conducting a breadth-first search (enumeration of closest nodes first [17]) from node n and finding all simple paths terminating at node n, where a simple path has no node appearing more than once. We confirm that a ring is primitive as follows: For each pair of nodes on the ring, we ascertain that the graph distance between them is equal to the minimum ring distance between the two nodes (there are two paths between each pair of nodes on a ring). By eliminating all non-primitive rings, what remains is the local cluster for node n.

Goetzke & Klein suggest an efficient algorithm for determining all the (primitive) rings in a network, which proceeds as follows:

1. Compute a distance matrix such that the graph distance between nodes i and j appears in row i column j. They suggest computing these distances by computing all pairs of distance 1 (first neighbors), then all pairs of distance 2, then all pairs with distance 3, etc.

2. Fix an edge e and perform step 3 (below). Remove e from the graph. If fewer than 3 edges remain, finish. Otherwise, examine the distances in the new graph; if a distance between the two nodes is greater than their distance in the previous graph, change the respective value in the distance matrix to the value "infinite." Repeat step 2.

3. Determine all rings containing e. Start with rings of length 3 and stop if length $(2d+2)$ has been reached (where d is the maximum distance in the distance matrix, also called the diameter of the graph). For determination of rings with length λ, the following procedure is used: Mark one of the two nodes of the fixed edge e as a starting point; choose an arbitrary node not yet considered with distance $\lambda/2$ to the the starting point. Try to find two distinct paths between the chosen node and the starting-point, alternating step-by-step from one path to the other.

Goetzke & Klein do not provide a rigorous running-time analysis for their ring-finding algorithm; however, it is easily sketched out. Step 1 requires, by use of a simple data structure, $O(n^3)$ time, where n is the number of nodes of the network, since it computes approximately an $n \times n$ matrix of distances, and finding the shortest path can take as long as $O(n)$. Step 2 merely cycles though the edges and checks the distance matrix and possibly recomputes the distance matrix (requiring $O(mn^2)$ time, where m is the number of edges in the network). Step 3 requires, for each distance λ, a search of the distance matrix for nodes of distance $\lambda/2$ from the chosen endpoint of e; then finding an appropriate ring containing this edge and another node (for which $O(d^2+n^2)$ time can probably be achieved by sorting the distances and not having to search the entire matrix for each length). Altogether, for large networks, the initial computation of the distance matrix is most time-consuming and the limiting factor.

Since we would rather concentrate on what Goetzke & Klein refer to as "rings of interest," we let the user define the maximum length of a ring to search for (where maximum length < 20 appears reasonable). Also, instead of computing all the rings in the entire structure, we simply compute the local clusters for individual nodes (in other words, we ignore step 2 and do only step 3). Our algorithm then proceeds essentially as follows:

1. Define $N_i(n)$ to be the number of nodes of graph distance i to node n. For a chosen n, compute an all-pairs distance matrix of size $D \times D$, where $D = \sum_{i=1\ldots d} N_i(n)$ and d is half the user-specified maximum ring length. The $D \times D$ matrix includes all-pair distances for nodes within distance d of node n. We may use an all-pairs shortest path algorithm of our choice; we chose a variation of Dijkstra's algorithm for simplicity [17].

2. Find a ring containing n. This is done by performing a breadth-first search from n back

to n; if the search is longer than the longest ring of interest, start a new search. Ascertain that this ring is primitive by comparing the shortest ring distance between each pair of nodes to their actual shortest distance as computed in Step 1. If it is primitive, enqueue the ring.

For our Step 1, the running time for computing the distance matrix is $O(D^3)$, using a simply implemented data structure. Generally, we have restricted our "rings of interest" to length 15, which means $d = 8$, so this step is rather fast. In our Step 2, enumerating all rings is related to the square of the size of the local neighborhood D (sum of all the nearest neighbors up to N_d). Eliminating rings that are not primitive takes time related to the square of the length of the ring (to look up the distances of all pairs on the rings).

Goetzke & Klein do not provide a formal proof of the correctness of their algorithm for finding primitive rings. We suggest that such a proof is not necessarily obvious from their algorithm. In their Step 3, they use a time-saving technique. They offer that enqueuing all the rings and then dequeuing all that are not primitive is too expensive, so they look for primitive rings as they go. However, the technique they use, while certainly finding only primitive rings, may fail to find all primitive rings. The discrepancy arises because, in considering a ring of length λ, they find the "chosen point" at distance $\lambda/2$ from the starting point. They then find two non-intersecting paths of length $\lambda/2$. There is, however, allowance in the definition of a primitive ring for one path on the ring to be larger than the shortest path distance. It is not clear how their procedure will find these rings as well (for example, for another chosen edge e in a future iteration of their Step 3), whereas ours surely does because we enumerate all rings for each node in turn.

4.3 Local clusters of silica polymorphs

Our contention is that all topological information is embedded in the local cluster defined by the set of primitive rings passing through a node. Certainly, for crystals, we have shown in Section 3.1 that the local rules contain all the information for the entire structure, so certainly the local cluster (which is larger than the set of tetrahedra necessary to describe the local rules) contains that information. What local clusters provide that local rules do not is a language to describe non-crystalline structures. The rules for generating non-crystalline structures may, in fact, also be simple (Section 5.1), but the optimization applied to the rules to obtain connected structures will, in most cases, occasion different local clusters at each node. Obtaining a complete local topology, as represented by the local cluster, is therefore essential for non-crystalline arrangements and of interest for crystalline arrangements. The

local cluster functions somewhat as does the unit cell for a crystal in specifying the local environment; a larger, more inclusive non-primitive unit cell is often the more intuitive choice for representing local symmetries, and in the same way the local cluster is the more intuitive choice for distinguishing the local topologies, even in crystals. The local clusters for non-crystalline structures specifically define the critical intermediate-range order.

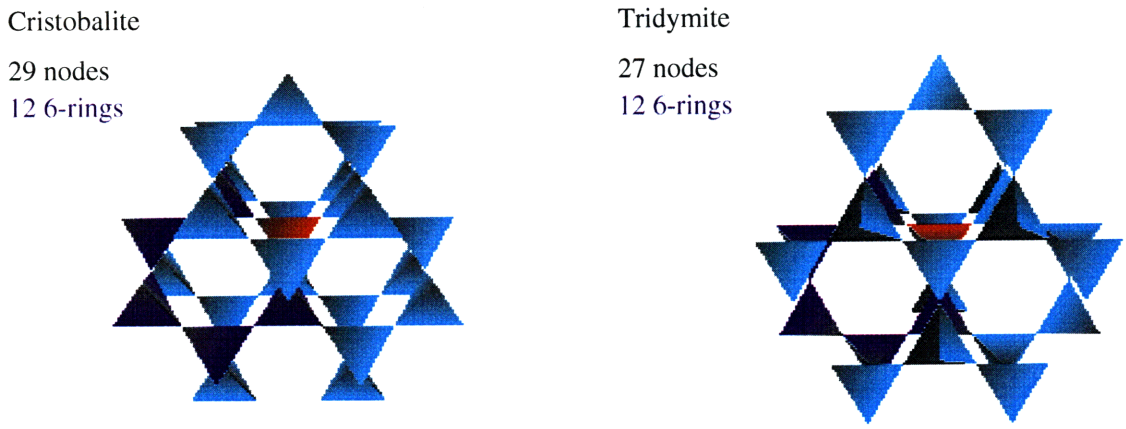

Figure 4.1: Local clusters for cristobalite and tridymite, viewed down [111] and the *c* axis, respectively. The red tetrahedron is the central node. The clusters both contain 12 6-rings through the central node, one of which is highlighted, but differ in number of tetrahedra.

The local clusters for tridymite and cristobalite are illustrated in Figure 4.1. Every tetrahedron in either structure is equivalent, and each local cluster comprises 12 6-rings (one of which is highlighted), two through each edge or 12 through each node. The sizes of the two clusters are different and distinguish the two polymorphs: the local cluster of tridymite contains 27 nodes, while that of cristobalite contains 29. These are the two least dense compact crystalline forms.

In quartz, the structure is dominated by 8-rings (Figure 4.2), with a local cluster of 63 equivalent tetrahedra comprising 6 6-rings and 40 8-rings. The 6-rings are joined in two distinct non-contiguous locations, and this conjunction—together with the requisite bond angles—forces the structure to have 8-rings. The 8-rings (one of which is highlighted) are more highly convoluted than is possible for 6-rings; that convolution is responsible for the denser packing of tetrahedra in quartz. Moganite has a structure closely related to that of quartz, but with the *c*-axis channels filled owing to the presence of 4-rings. In each of its two inequivalent local clusters (Figure 4.3), 8-rings dominate, but 6-rings (highlighted) define much of the structural framework. The two clusters are very different in size, the larger second cluster having 50% more 8-rings.

Keatite has a very different local structure from that of quartz, with two inequivalent tetrahedra. It was found that keatite was easier to model with three sets of tetrahedra, two

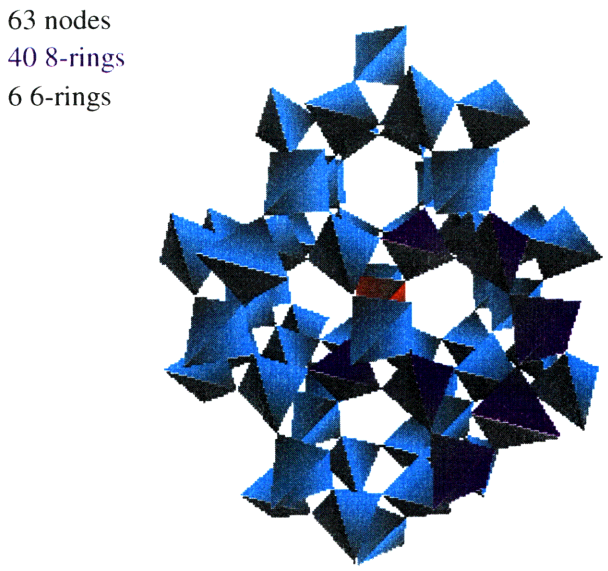

Figure 4.2: The local cluster of quartz, comprising 63 nodes and containing 40 8-rings and 6-rings. A convoluted 8-ring is highlighted.

of which were discovered to be equivalent; the local clusters associated with these two inequivalent sites are depicted in Figure 4.4. The ring contents comprise 3 5-rings, 5 7-rings and 6 8-rings for one site, and 4 5-rings, 4 7-rings and 4 8-rings for the other. Like moganite, while each local cluster features the same kinds of rings, the two clusters are very different in size. The existence of 5- and 7-rings in crystalline keatite is noteworthy because of the more customary association of odd-membered rings with aperiodic networks.

Figure 4.5 illustrates the two inequivalent local clusters for the densest tetrahedral crystalline form, coesite, associated with respectively 75 and 81 tetrahedra and each comprising 4-, 6-, 8-, 9-, 10-, 11- and 12-rings. The last two dominate, and examples are highlighted.

Table 4.1 lists the number of first through fourth (N_1–N_4) network neighbors, local cluster content and network dimension, and primitive ring content for the compact crystalline silica polymorphs in order of decreasing density. Tetrahedra in all tetrahedral polymorphs will have 4 first neighbor tetrahedra, 12 second neighbor tetrahedra (N_2) unless 3- or 4-rings are present, $3 \cdot N_2$ third neighbor tetrahedra (N_3) unless 5- or 6-rings are present, and $3 \cdot N_3$ fourth neighbor tetrahedra (N_4), unless 7- or 8-rings are present. The local clusters, which all truncate within the fifth neighbor shell, are quite compact, the large number of 8-rings in quartz and even larger rings in coesite being responsible for the higher number of tetrahedra in their local clusters.

Polymorph		Stability Regime	Density	Primitive Ring Content	N_1	N_2	N_3	N_4	Local Cluster	Cluster Dim.
Coesite	(node 0)	high pres. (3.55-7.6 GPa)	3.01	2 4-rings, 2 6-rings, 2 8-rings, 8 9-rings, 2 10-rings, 10 11-rings, 9 12-rings	4	10	22	47	75	6
	(node 1)			2 4-rings, 1 6-ring, 2 8-rings, 10 9-rings, 3 10-rings, 12 11-rings, 9 12-rings	4	10	23	47	81	
Quartz		low temp. ($< 1140K$)	α 2.65 β 2.53	6 6-rings, 40 8-rings	4	12	30	52	63	4
Moganite	(node 0)	low temp.	2.62	2 4-rings, 4 6-rings, 12 8-rings	4	10	24	40	33	4
	(node 1)			1 4-ring, 4 6-rings 18 8-rings	4	10	24	41	45	
Keatite	(node 0)	low temp.	2.50	3 5-rings, 5 7-rings, 6 8-rings	4	12	29	50	43	4
	(node 1)			4 5-rings, 4 7-rings 4 8-rings	4	12	26	48	31	
Cristobalite		high temp. (1743-2001 K)	α 2.33 β 2.21	12 6-rings	4	12	24	42	29	3
Tridymite		high temp. (1140-1743 K)	"α" 2.26 HP 2.18	12 6-rings	4	12	25	44	27	3
Metamict		low temp.	2.26	$n \sim 6$						
Vitreous		high temp. ($T_g \sim 1333K$)	2.21	$n < 6$						

Table 4.1: Silica Polymorph Topology

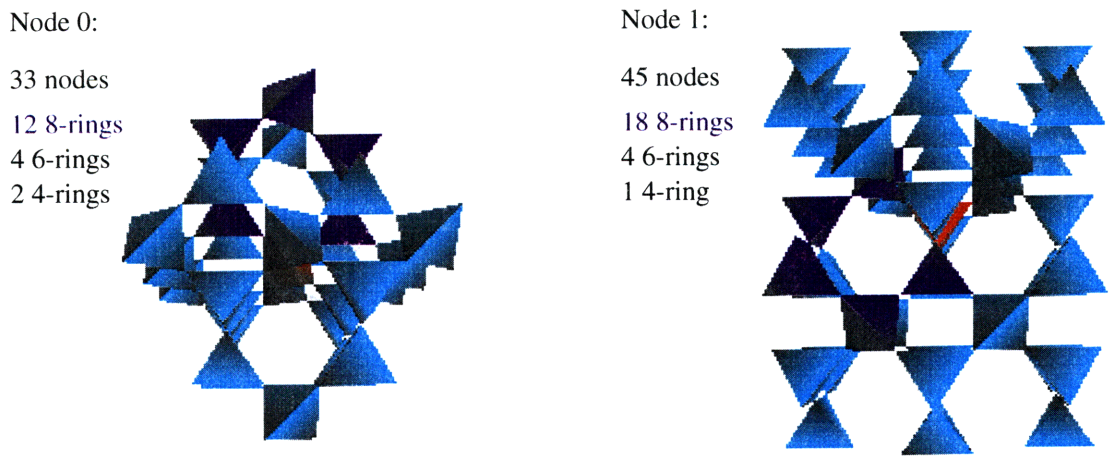

Figure 4.3: The two local clusters of moganite, corresponding to the two inequivalent tetrahedron environments. The clusters both contain 4-, 6- (highlighted) and 8-rings, with the latter dominant, but differ in ring counts and number of tetrahedra.

4.4 Local clusters for SiC and Si_3N_4

Local clusters may also be used to describe the local structure of silicon carbide and silicon nitride. Because of the higher branching involved with the breadth-first search in the ring-finding algorithm, sometimes it is easier to restrict the size of "rings of interest" even further. Because the branching factor is so much higher in SiC and Si_3N_4 (that is, the degree of their underlying graphs is higher and therefore, the nearest neighbor numbers N_i are much higher than those in SiO_2) the local neighborhoods in these structures are bound to be much higher. In order to save time, we restrict our rings of interest in Si_3N_4 to those of length 10 and in SiC to those of length 6. For the crystalline versions, it is the case that there are no primitive rings of length greater than 4 in SiC or 7 in Si_3N_4 but for amorphous experiments (Chapter 5) finding longer rings is usually an indication of underconnection in the structure.

In both α- and β- silicon carbide, the local clusters consist of 19 tetrahedra composed of 12 3-rings and 12 4-rings. These clusters are compared in Figure 4.6.

The local clusters for the α- and β- versions of Si_3N_4 are vastly different, with β-silicon nitride being dominated by 6-rings and α- by 5-rings. Figures 4.7 and 4.8 illustrate the clusters for both polymorphs.

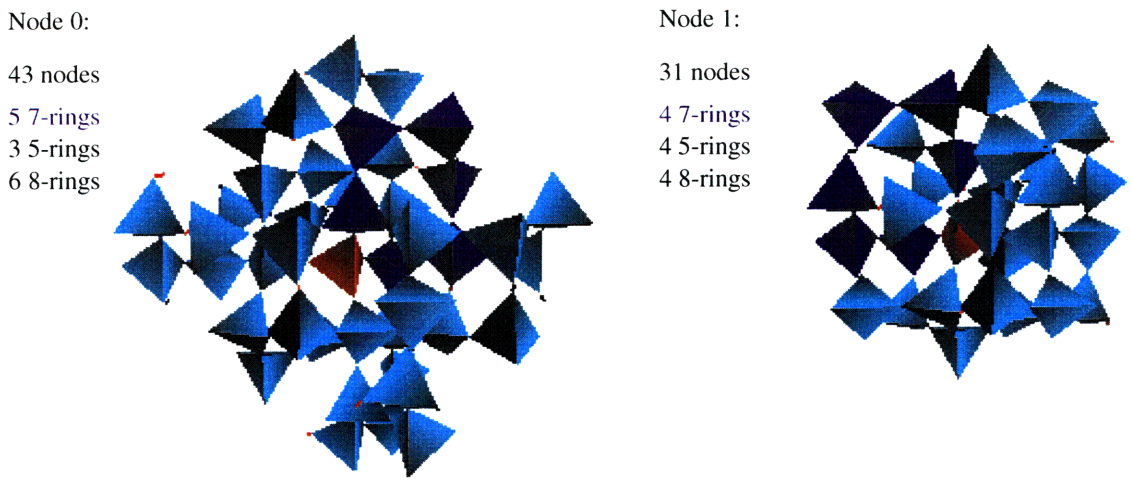

Figure 4.4: The two local clusters of keatite, corresponding to the two inequivalent tetrahedron environments. Both contain odd 5- and 7-rings, in addition to 8-rings. Two 7-rings are highlighted.

4.5 Rings and density

Table 4.1 suggests a correlation between density and ring size. The 6-rings for cristobalite and tridymite yield the lowest density minimum, because 6-rings are still rather rigid and close to planar rings, whereas larger rings–such as the 8-rings in quartz–can more easily double back on themselves to effect more efficient tetrahedral packing [82, 54]; rings smaller than 6-rings represent closer packing only within the ring itself. Coesite's much higher density is thus largely a consequence of the presence of much larger primitive rings. The twelve 6-rings in cristobalite and tridymite represent a global minimum, because local clusters of 13 6-rings are found to lead to serious steric crowding while 11 6-rings represent a step towards the tree density catastrophe [82]. The position of vitreous silica in Table 4.1 strongly suggests dominance of 6-rings in the structure, while the 3% higher density associated with the radiation-induced reconstruction of vitreous silica to the radiation-amorphized (metamict) state suggests creation of larger rings from smaller ones.

Node 0:

75 nodes

2 4-rings
2 6-rings
2 8-rings
8 9-rings
2 10-rings
10 11-rings
9 12-rings

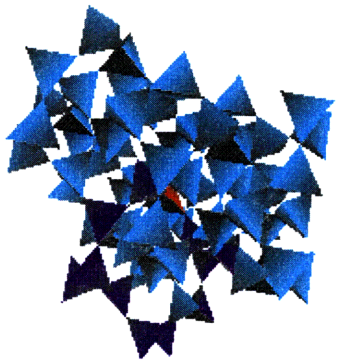

Node 1:

81 nodes

2 4-rings
1 6-ring
2 8-rings
10 9-rings
3 10-rings
12 11-rings
9 12-rings

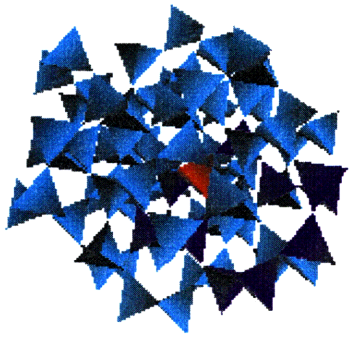

Figure 4.5: The two local clusters of coesite, corresponding to the two inequivalent tetrahedron environments. Both clusters are very large and contain up to 12-rings. A 12-ring and an 11-ring are respectively highlighted.

α–SiC

19 nodes
12 3-rings
12 4-rings

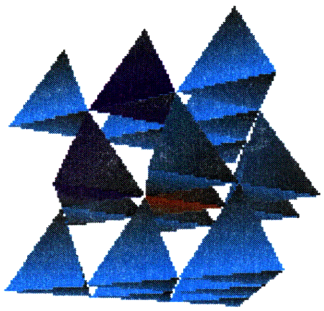

β– SiC

19 nodes
12 3-rings
12 4-rings

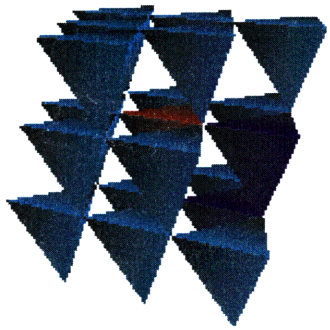

Figure 4.6: The local clusters of α- and β- SiC. Both clusters contain 3- and 4-rings. 3-rings are highlighted.

27 nodes
3 3-rings
8 4-rings
20 6-rings

Figure 4.7: The local cluster β-Si_3N_4.

Node 0:

40 nodes
4 3-rings
4 4-rings
13 5-rings
1 6-ring
9 7-rings

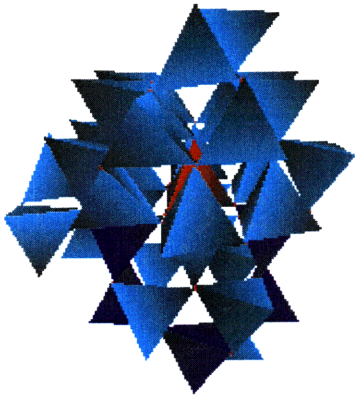

Node 1:

29 nodes
2 3-rings
12 4-rings
12 5-rings
1 6-ring
3 7-rings

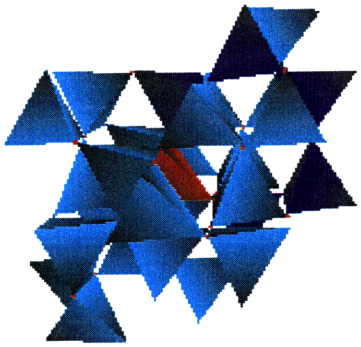

Figure 4.8: The local clusters of α-Si_3N_4.

Chapter 5

Producing amorphous structures

There are two general approaches to generating aperiodic structures. We say that a model is *amorphous* when it is constructed using deviant rules and we say that a model is *amorphized* when it was the result of a simulated collision cascade disordering event. The former involves using a set of faulty rules (those which do not describe a crystal and therefore propagate defects), and the latter technique simulates irradiation of a previously generated crystal structure.

5.1 Amorphous silica networks

For the sake of brevity, we here define a structure as amorphous when it lacks topological order [41]. Amorphous silica networks can, for example, result from quenching the liquid, irradiating crystalline polymorphs, oxidizing silicon, depositing from a vapor, or dehydrating gels; the resulting structures are distinct [102] and depend on their modes of formation. The power of local topological modeling comes into its own for such non-crystalline arrangements, since neither local rules-based assembly nor local-cluster descriptions rely on periodicity or symmetry properties, and self-assembly can mimic the stochastic routes responsible for topological differences. In an amorphous network, the local cluster will vary from node to node in the network, as is easily appreciated from the two-dimensional continuous random network illustrated in Figure 1.3, but the ring-finding algorithms operate analogously to the crystalline cases discussed in Section 4.1.

Assembly rules can be based on slightly faulty versions of the assembly rules appropriate to crystalline polymorphs stable at the ambient conditions of temperature and pressure obtaining during formation of the amorphous phase. For example, cristobalite-like local

The research reported in this chapter is joint work with Bonnie Berger and Linn Hobbes and was first published in [72] and subsequently published in [61, 60, 71, 70]

rules might be appropriate for rapid cooling from a high-temperature collision cascade in radiation-amorphized silicas, while tridymite-like rules could be relevant to slower cooling through a lower temperature ($1333K$) glass transition. Quartz- (or moganite- or keatite-) like rules are apposite to formation routes nearer room temperature. Two rules modifications are possible: a change in the initial-node offset, and deviations from assembly rotations applied to successive nodes; effects of these modifications are illustrated in Section 5.1.1. Their continued propagation results in structural defects which eventually alter local topology and impart topological disorder. Additional optimization routines are necessary to preclude steric crowding and ensure connectivity while minimizing tetrahedron distortions; these routines are discussed in Section 5.1.2 and in greater detail in Section A.5.5.

5.1.1 Deviant local rules

Initial node offset

In one approach to generating a quartz-like a-SiO_2 structure, an initial node offset of 5° about x was chosen with the same rotation rules as in Figure 3.1 for ideal crystalline quartz. (In the coordinate system chosen, offset rotations about y alter only θ, as in the α–β transition, while offset rotations about z have no effect because the rules rotations are defined about z). The first 200 nodes of the model exhibited only small differences from ideal quartz (Figure 3.2) and so are not illustrated here. However, a distribution of Si-O-Si angles θ (Figure 5.1) appeared, centered just below θ for ideal quartz. Even more importantly, the local clusters at the initial as well as further nodes exhibited topological differences from quartz and from each other; those for the initial and three other randomly-selected nodes are illustrated in Figure 5.2. Larger offsets generated increasing topological disorder. The density for the 5° offset structure was 6% higher than that for ideal quartz, but lower than that for α-quartz.

Rules rotation modification

Small changes in the rotation rules have a more significant impact than offsets on structural topology, because it is the exactness of these rotations that generates periodicity. Owing to the 90° rotations in the first setting of cristobalite rules (Figure 3.3, initial node offsets around x or y affect only θ, as in the α–β transition, and around z have no effect because the rules rotations are defined about z. We were therefore, in fact, constrained to alter the rotation rules instead of the offset in our attempt to generate an aperiodic cristobalite-like a-SiO_2. A β-cristobalite offset was chosen, and the deviant rotation rules used are compared to those of β-cristobalite in Figure 5.3. Figure 5.4 compares the first 200 nodes of the resulting decidedly amorphous structure to those of β-cristobalite. Again, a breadth in Si-O-Si angle

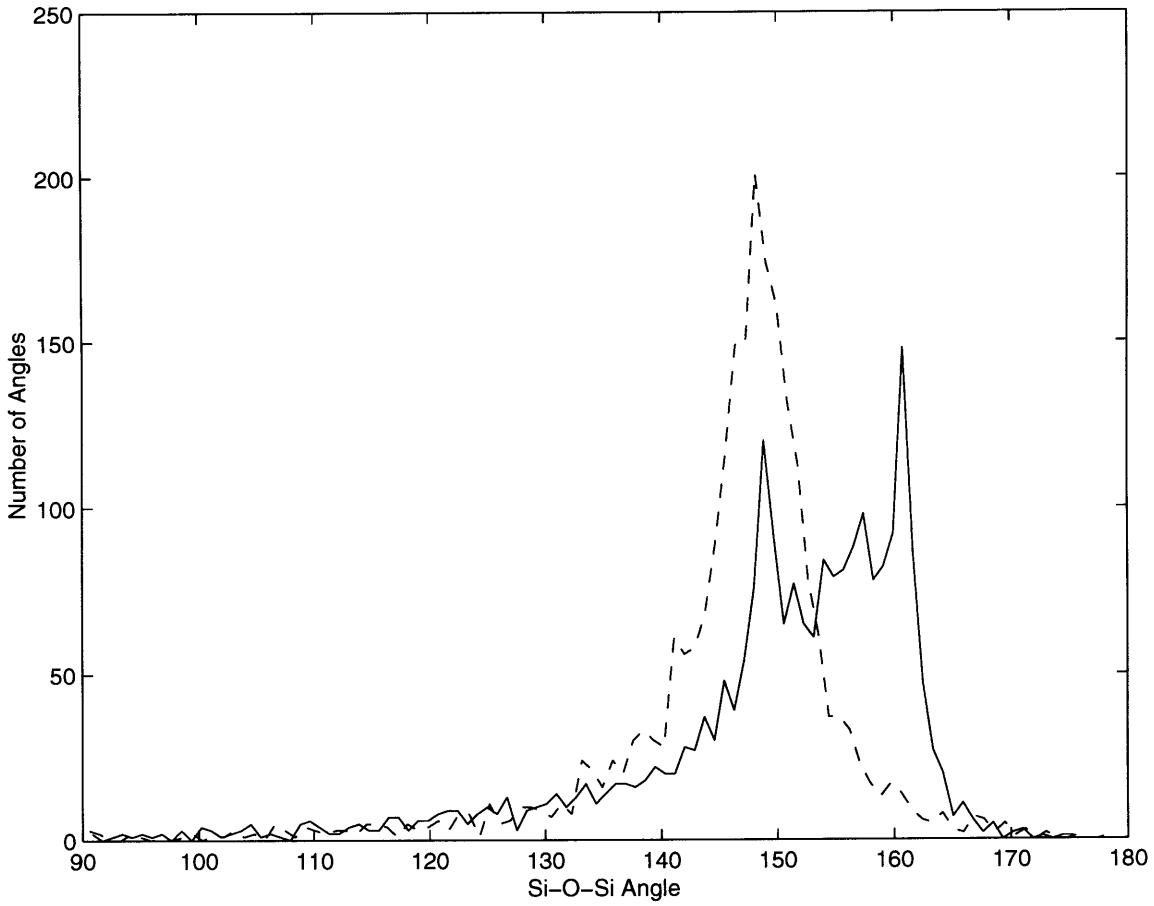

Figure 5.1: Si-O-Si angle distributions for the cristobalite-like (broken line) and quartz-like (solid line) 1500-node models of amorphous SiO2. Both distributions peak near the angles for the respective crystal structures from which the deviant rules were derived. The distribution for the cristobalite-like model, assembled using a 5 rotation deviation, has a broader tail than does that for the quartz-like model, assembled with a 5° node offset.

accrues, centered just below θ for β-cristobalite (Figure 5.1), and local clusters exhibited topological differences (Figure 5.5). The density (2.29) was 5% larger than for our model β-cristobalite (2.17) and 4% different from the densities of actual β-cristobalite or vitreous silica (2.21).

5.1.2 Optimization routines

Because, with deviant rules, tetrahedra do not connect up invariantly, as in crystals, neither rules alteration would function without additional algorithms to ensure connectivity and avoid intersection of tetrahedra. To optimize connectivity, shared vertices in adjacent nodes were connected by Hookeian springs (with adjustable spring constant); as each new tetrahedron was added and bonded into the network, the displacements of all springs in the

Node 0:
62 tetrahedra
6 6-rings
38 8-rings

4, 12, 30, 53

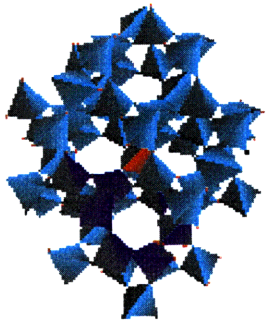

Node 221:
63 tetrahedra
6 6-rings
40 8-rings

4, 12, 30, 52

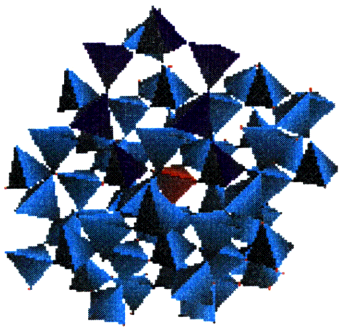

Node 403:
55 tetrahedra
5 6-rings
8 7-rings
9 8-rings
2 9-rings
1 10-ring

4, 12, 31, 45

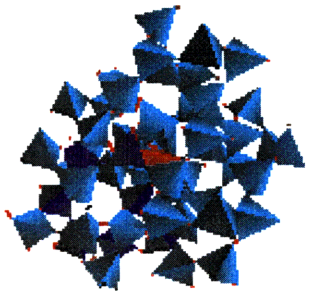

Node 585:
46 tetrahedra
5 6-rings
23 8-rings

4, 12, 22,39

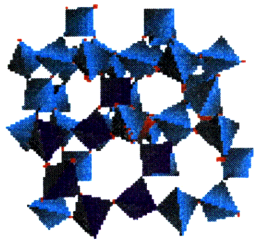

Figure 5.2: Four representative local clusters from a 1500-node mode of quartz-like a-SiO_2, assembled using a 5° node offset from idealized quartz. Some clusters are quite quartz-like, others rather different, though 8-rings continue to dominate. Red links between tetrahedra represent the remanent springs inserted between vertices which translate into tetrahedron distortions.

```
Beta-Cristobalite
1
4 1
REGULAR
y 23 ;
0 1  z 90 ;
0 0  z -90 ;
0 3  z 90 ;
0 2  z -90 ;
```

```
a-Cristobalite
1
4 1
REGULAR
y 23 ;
0 1  z 85 ;
0 0  z -85 ;
0 3  z 85 ;
0 2  z -85 ;
```

Figure 5.3: Comparison of the rules files for β-cristobalite (in its first setting) and a cristobalite-like a-SiO_2 incorporating a 5° rotation deviation (in the rules for each vertex) from β-cristobalite.

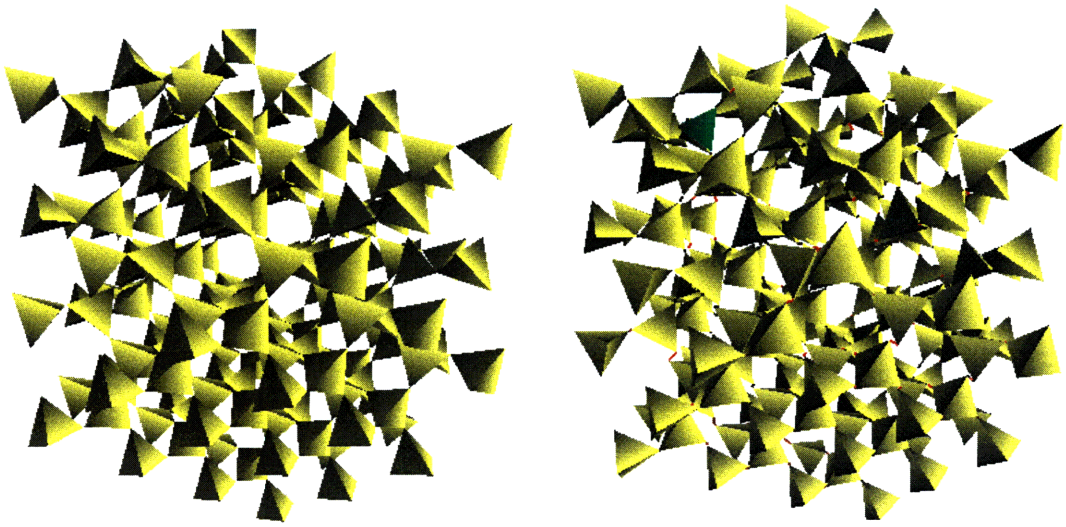

(a) (b)

Figure 5.4: Comparison of 200-node models of (a) β-cristobalite and (b) cristobalite-like a-SiO_2 assembled using the respective rules files in Figure 5.3. The single green tetrahedron represents an underbound node.

network were re-adjusted so as to minimize globally the total elastic energy stored in the springs; a damping term prevented unbounded oscillations In this optimization, a remanent non-zero spring length corresponds to distortion of a tetrahedron; such distortions were typically kept small (spring lengths 0.01-0.02 nm) but served to broaden the O-Si-O tetrahedral angle (Figure 5.6). To preclude intersections, a separate routine monitored and rejected tetrahedron intersections.

The augmented building algorithm proceeds as follows: When an unshared vertex seeks an adjacent node, a new tetrahedron is created and appropriately rotated; if the intersection test concludes there is no room locally to add a new tetrahedron, the unshared vertex looks for an available vertex in its vicinity regardless of type. If it fails to find any available vertex, the algorithm breaks an existing bond between between nodes and reconnects one of the freed vertices (the closer and better in terms of bond angle) to the previously unshared vertex, adding the other freed vertex back into the BFS queue. Underbound nodes remaining when the model structure has reached its prescribed ultimate size are colored green (as in Figure 5.4); there are few and some of these would eventually be fully bound into the structure after undergoing additional BFS in a larger model. For details on this building algorithm see Appendix A.

Node 0:
29 tetrahedra
12 6-rings

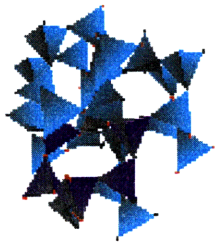

Node 46:
38 tetrahedra
7 6-rings
7 7-rings
1 8-ring
2 10-rings

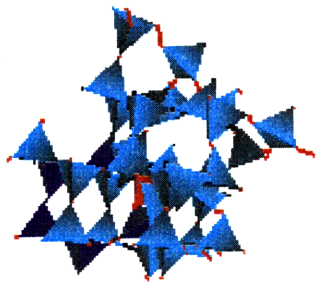

Node 170:
32 tetrahedra
5 6-rings
5 7-rings
1 9-ring

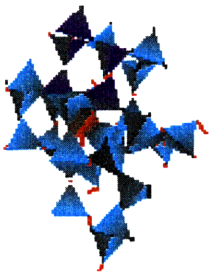

Node 641:
22 tetrahedra
8 6-rings

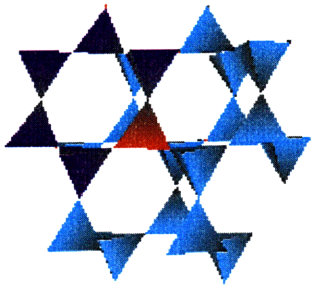

Figure 5.5: Four representative local clusters from a 1500-node model of cristobalite-like a-SiO_2, assembled using a 5° rotation deviation from the rules for β-cristobalite. Most clusters have similar size to that for cristobalite (29 tetrahedra) but exhibit very different ring counts, though 6-rings still dominate.

5.1.3 Analysis of glassy structures

Ring statistics and radial distribution functions are two traditional quantifications of topologically disordered network structure. To effect a global ring count, one could mount a Goetzke-Klein search; but we maintain that local ring relationships, as embodied in the local cluster, are a far more revealing statistic than the overall distribution of ring sizes. To provide some simple, more topologically significant comparative measure of generated amorphous structure we prefer to compute an ensemble average of ring histograms for each local cluster. Such a procedure overcounts rings from a global point of view but retains some sense of the local ring relationships. Average histograms computed from 20 local clusters of the quartz-like and cristobalite-like amorphous silicas generated are compared in Figure 5.9.

Figures 5.7 and 5.8 record the partial radial density functions (RDFs) for O-O, Si-O and Si-Si correlations for the two a-SiO_2 models. These were computed by averaging results from 50 tetrahedra randomly chosen from the center-most 10% of the structure (to avoid boundary effects). For the Si-Si RDF, we computed the distance to all other Si atoms within

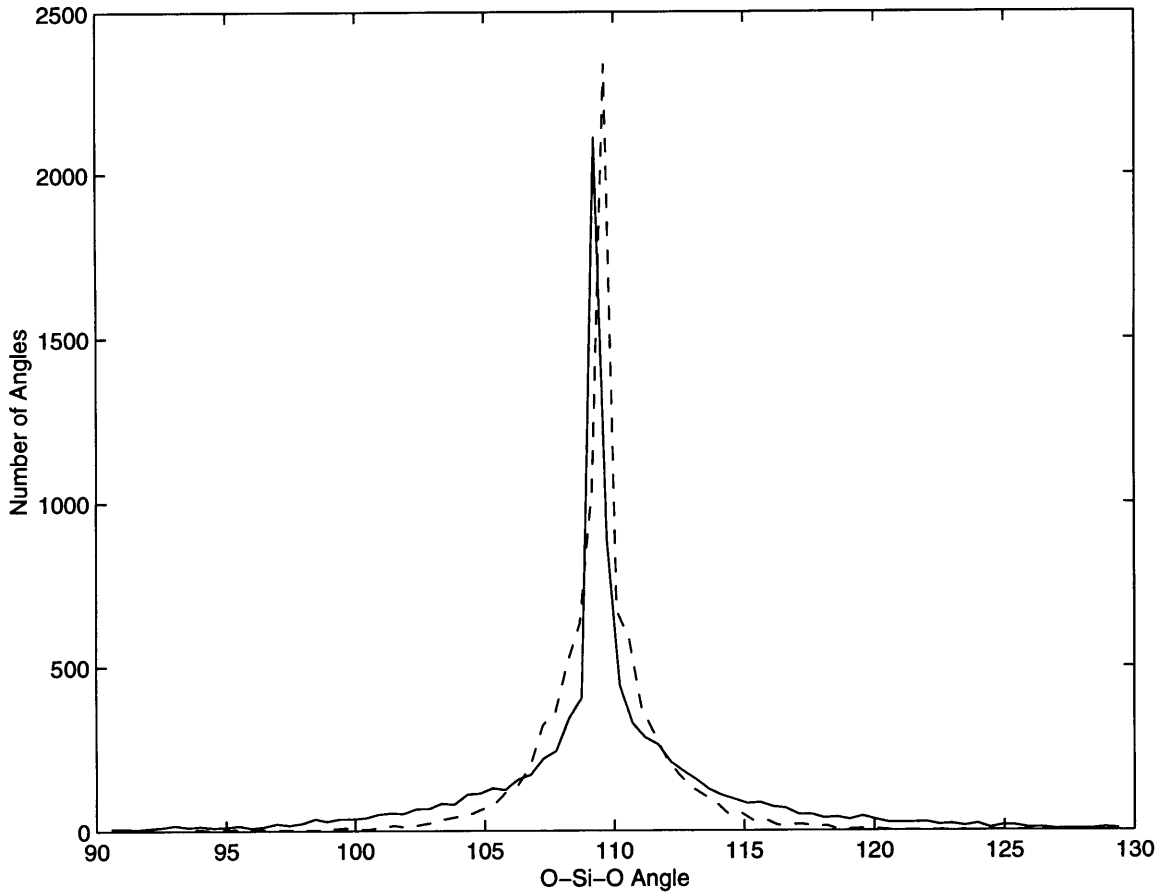

Figure 5.6: Distribution of O-Si-O angles in 1500-node models of cristobalite-like (broken line, 5° rotation deviation from β-cristobalite) and quartz-like (solid line, 5° initial node offset from idealized quartz) a-SiO_2. The angle for an undistorted tetrahedron is 109.5°.

RDF, we computed the distance from each of the vertices of the initial tetrahedron to the vertices of all other tetrahedra and divided by 8. For the small rules deviations used, the RDFs illustrated retain many of the principal features of the correlation functions for the crystals on which the rules were based. The RDF for quartz-like a-SiO_2 closely resembles the envelope of RDF peaks for the ideal quartz model. The RDF for cristobalite-like a-SiO_2 is farther removed from the RDF-peak envelope of β-cristobalite but still exhibits some broad peaks associated with the crystalline analogue.

5.1.4 Amorphous Si_3N_4 and SiC

Modified rules used for assembling amorphous versions of Si_3N_4 and SiC are given in Figures 5.10 and 5.11, incorporating 5° rotation deviations from the rules for β-Si_3N_4 and α-SiC. An assemblage of 1000 tetrahedra of a-Si_3N_4, assembled using the rules in Figure 5.10,

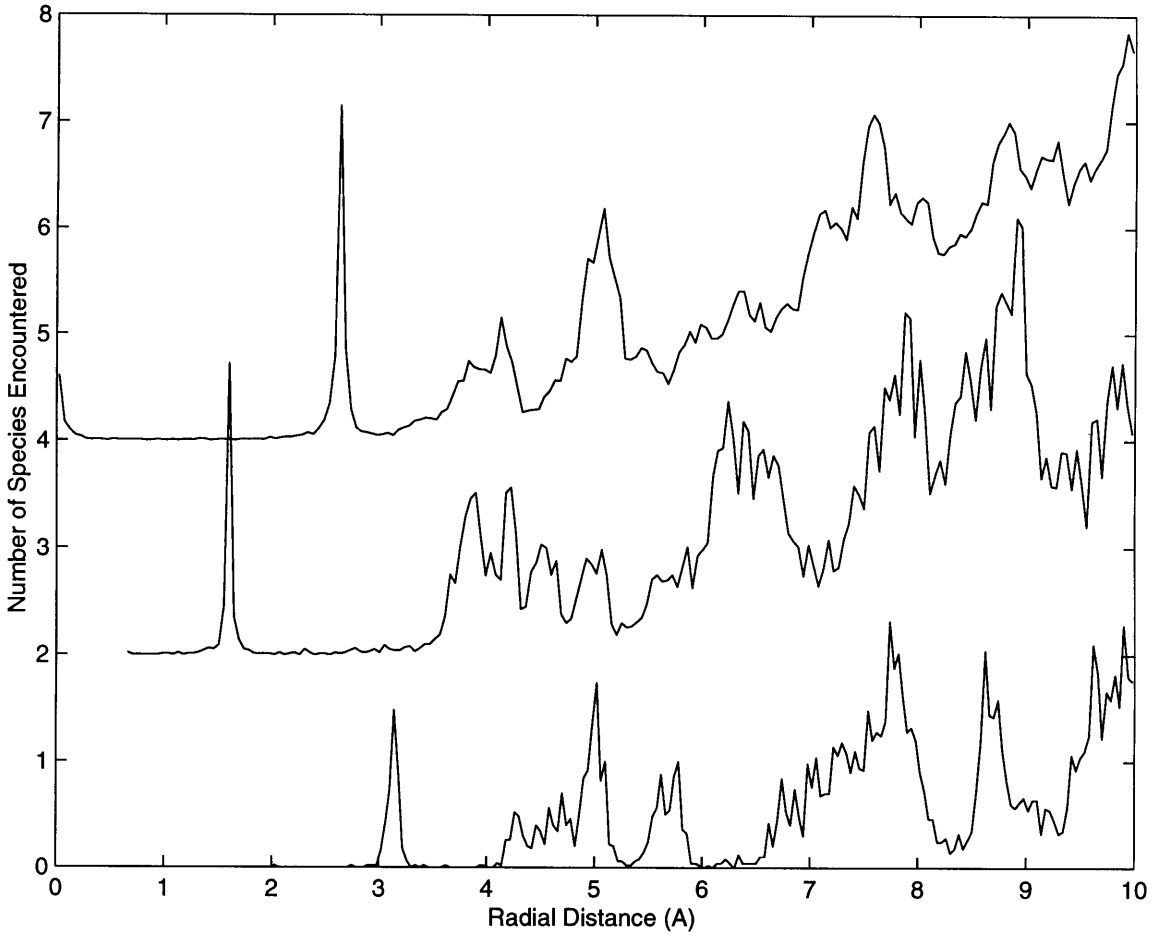

Figure 5.7: Partial radial density functions (RDFs) for O-O (top), Si-O (middle) and Si-Si (bottom) correlations in the quartz-like a-SiO_2 model with 5° initial node offset from idealized quartz. The Si-O and O-O plots have been displaced vertically by 2 and 4 units respectively. The correlation variations closely follow correlation histograms for idealized crystalline quartz.

is shown in Figure 5.12 (200 tetrahedra were insufficient to reveal significant differences from β-Si_3N_4). Even at 1000 tetrahedra, the disorder was slow to propagate, and the most striking feature of the assemblage is the underconnected tetrahedra (highlighted). Tetrahedral distortions are also present as another means of accommodating the rotation deficit, as evidenced by the breadth of the N-Si-N tetrahedral bond-angle distribution Figure 5.15, though the average (Table 5.4) remains centered on the 109.5° tetrahedral ideal. The extracted local clusters show (Figure 5.13) that local topological disorder has in fact propagated, though 6-rings still generally dominate and the computed radial density functions (Figure 5.14) remain extremely crystal-like. The three families of Si-N-Si angles found in crystalline β-Si_3N_4 persist in the topologically disordered assembly (Figure 5.16), though broadened and shifted to slightly larger angles (in contrast to silica where the average Si-O-

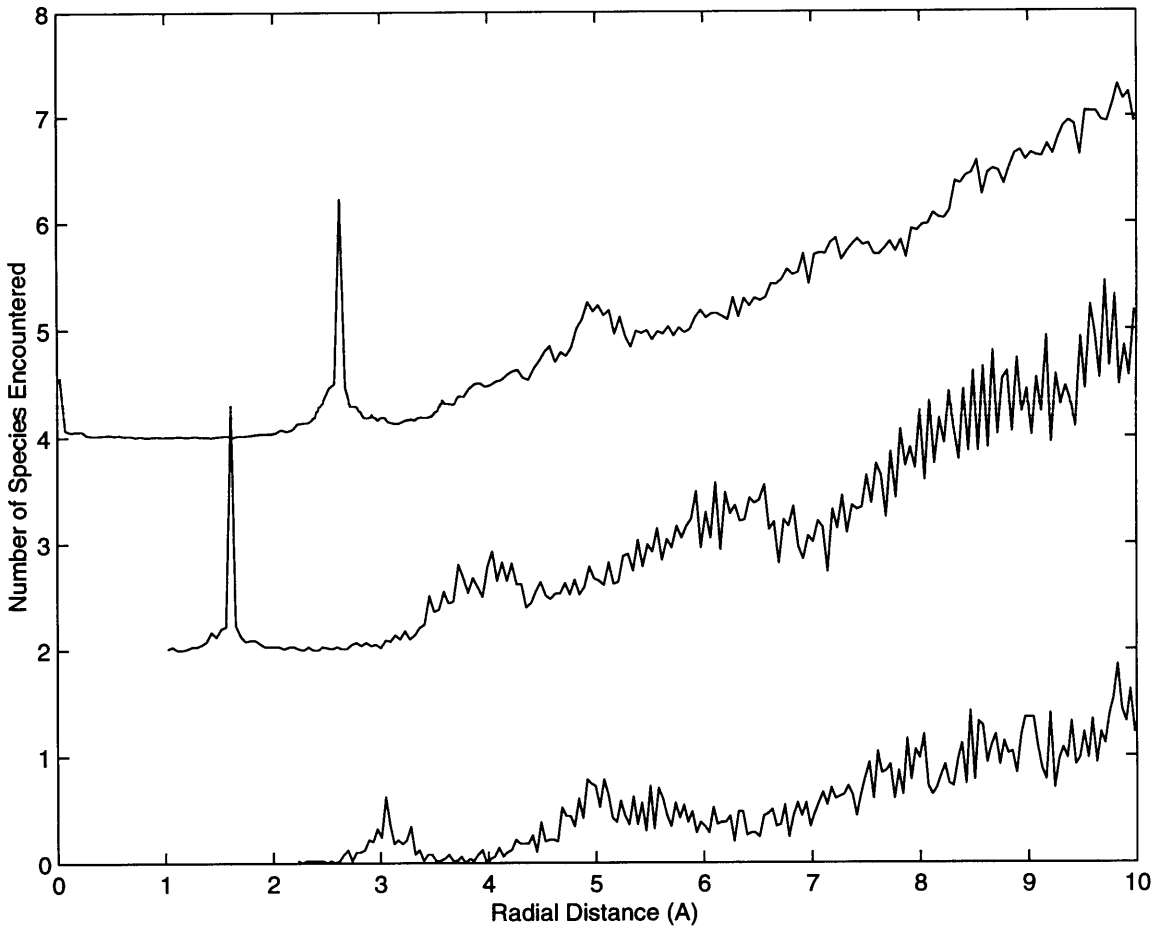

Figure 5.8: Partial radial density functions for O-O (top), Si-O (middle) and Si-Si (bottom) correlations in the cristobalite-like a-SiO_2 model with 5° rotation deviation from β-cristobalite. The Si-O and O-O plots have been displaced vertically by 2 and 4 units respectively. The correlation variations parallel but do not replicate correlation histograms for β-cristobalite and exhibit considerably less structure than do RDFs from crystalline β-cristobalite or those in Figure 5.7 for the quartz-like a-SiO_2 generated by 5° node offset.

Si angle was found to decrease).

1000 tetrahedra of a-SiC, assembled according to the rules in Figure 5.11, show in Figure 5.17 more evidence of topological disorder, but only at a cost of extensive underconnection and substantial tetrahedral distortion. The distortion is evidenced by long inter-vertex springs in the assemblage and a broad C-Si-C (Figure 5.15) angle distribution–or equivalently by the broad Si-C-Si angle distribution (Figure 5.16), since in this {4,4} structure the Si-C-Si inter-tetrahedral angle is also the C-Si-C intra-tetrahedral angle. Because we have elected to define [SiC_4] units as the tetrahedra, instead of [CSi_4], the average C-Si-C angle remained close to tetrahedral, but the average Si-C-Si angle θ, which should be equivalently tetrahedral, has shifted by 2.5° to 112°, corresponding to a large distortion of

[CSi_4] tetrahedra. Though the radial density functions (Figure 5.19) persist in crystal-like intermediate-range correlations, the local clusters (Figure 5.18) differ markedly from those of β-SiC, largely in the dominant appearance of 5-rings from the opening up of 3- and 4-rings as a consequence of the pervasive underconnection.

The degree of underconnection in all models was quantified by counting unbonded tetrahedron vertices and tabulating the percentage of underbound tetrahedra by number of missing connections (Table 5.1). The quantitative result confirms the qualitative impression from inspection that the a-SiC model is substantially less connected than are a-SiO_2 and a-Si_3N_4 models. A sizeable (and unquantifiable with the present counting algorithms) fraction of these underconnected tetrahedra are underbound because they reside at the surface. A rough estimate of the surface contribution can be made by enumerating all tetrahedra bound to the structure through only two vertices (those tetrahedra in SiO_2 missing two connections, in Si_3N_4 missing four, in SiC missing six), which are most likely to be surface tetrahedra; removing these from the total number of tetrahedra in the model leaves the interior tetrahedra, on which basis the underbound percentages can be recalculated. By this estimate, the a-SiO_2 is 86.4% connected, a-Si_3N_4 89.9% connected but a-SiC only 73.8% connected. Better estimates await an improved counting algorithm which specifically enumerates surface tetrahedra, but the substantial underconnection of a-SiC is nonetheless qualitatively apparent in the assembly depiction.

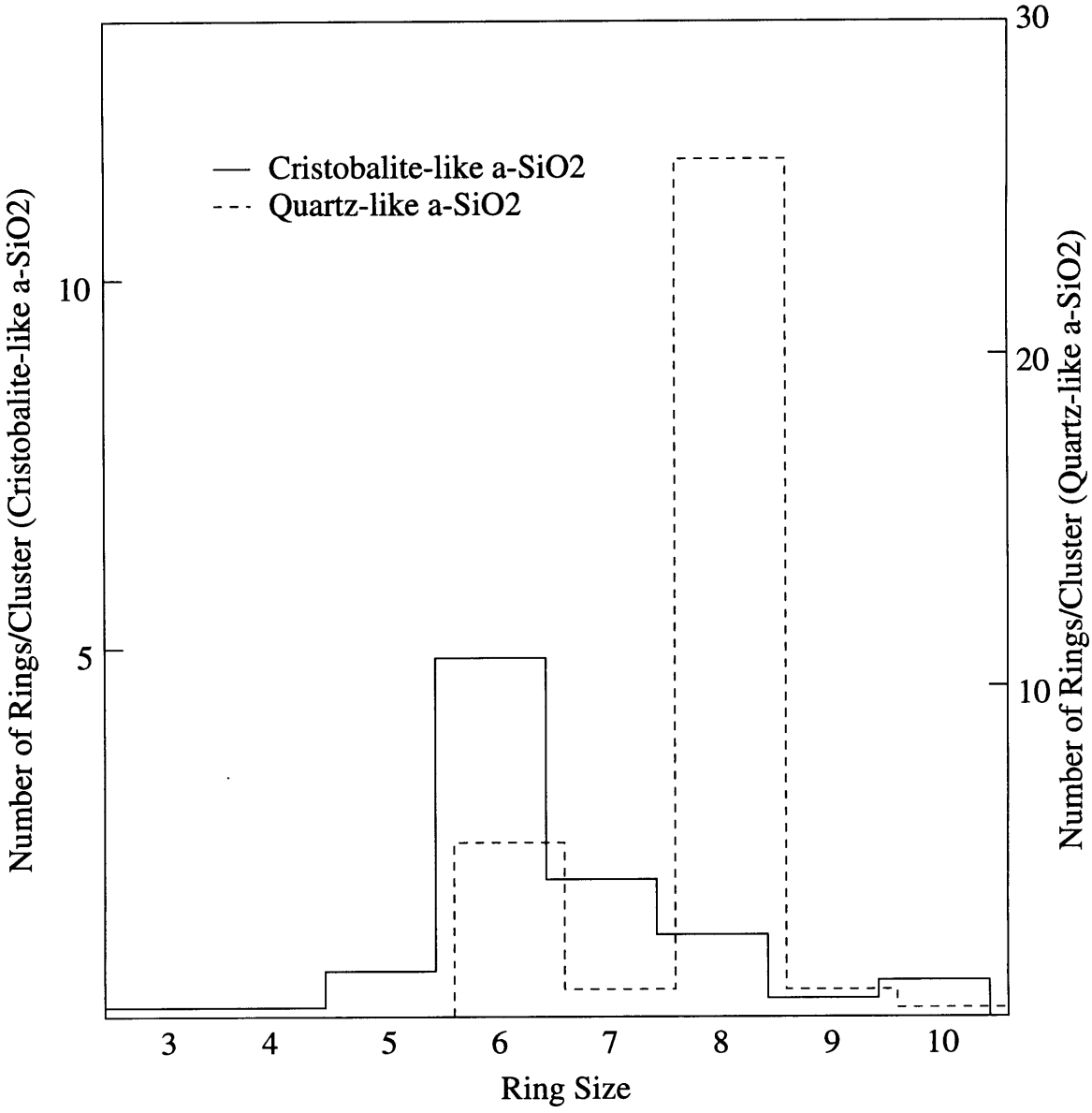

Figure 5.9: Histograms of primitive ring size distribution in local clusters of cristobalite-like (solid line) and quartz-like (broken line) a-SiO_2 averaged over 20 local clusters. Ordinate scales normalized by the size of the local cluster.

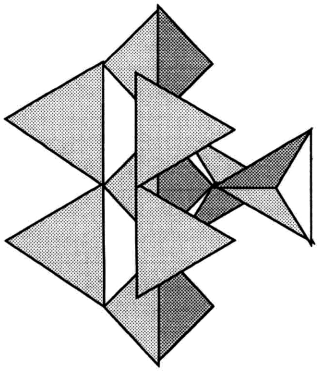

```
Beta-Si3N4
1
4 2
REGULAR
z 45 ;
0 1  y  60 ;    0 2  ;
0 0  y -60 ;    0 2  y  -60 ;
0 1  y  60 ;    0 0  ;
0 3  y 120 ;    0 3  y -120 ;
```

```
a-Si3N4
1
4 2
REGULAR
x 5 z 45 ;
0 1  y  55 ;    0 2  ;
0 0  y -55 ;    0 2  y  -65 ;
0 1  y  65 ;    0 0  ;
0 3  y 120 ;    0 3  y -120 ;
```

Figure 5.10: Deviant local rules for the formation of a-Si_3N_4.

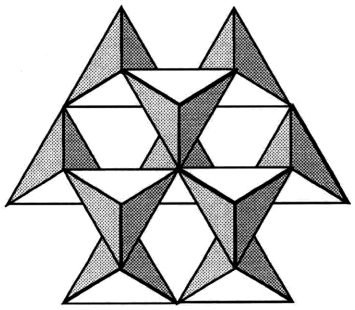

```
Alpha-SiC
1
4 3
REGULAR
x -45 y -144.8 z 90 ;
0 1       ;  0 2       ;  0 3  z 180 ;
0 0       ;  0 2       ;  0 3  z 180 ;
0 0       ;  0 1       ;  0 3  z 180 ;
0 0 z 180 ;  0 1 z 180 ;  0 2  z 180 ;
```

```
a-SiC
1
4 3
REGULAR
x -40 y -144.8 z 90 ;
0 1   x 5 ;  0 2   x 5 ;  0 3  z 175 ;
0 0  x -5 ;  0 2   x 5 ;  0 3  z 175 ;
0 0  x -5 ;  0 1  x -5 ;  0 3  z 175 ;
0 0 z -175;  0 1 z -175;  0 2  z -175;
```

Figure 5.11: Deviant local rules for the formation of a-SiC.

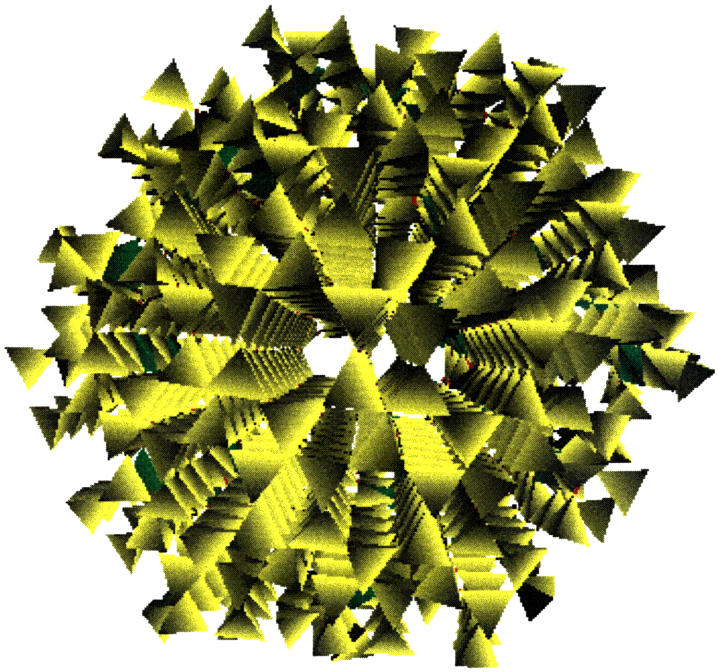

Figure 5.12: 1000 tetrahedra model of a-Si_3N_4 using the rules in Figure 3.19.

Node 100:

29 tetrahedra
3 3-rings
14 6-rings
8 4-rings
1 5-rings
1 7-ring

8,28,59

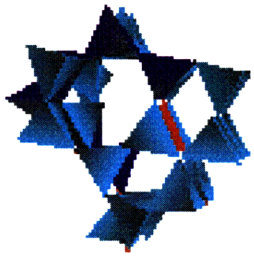

Node 180:

27 tetrahedra
3 3-rings
20 6-rings
8 4-rings

8,28,63

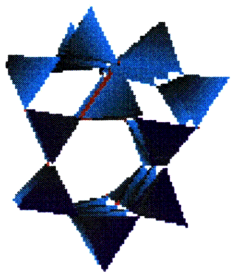

Node 409:

19 tetrahedra
3 3-rings
8 4-rings
4 5-rings

8,27,54

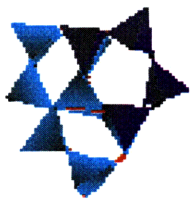

Node 604:

25 tetrahedra
1 3-ring
20 6-rings
2 4-rings
2 5-rings
1 7-ring

7,16,38

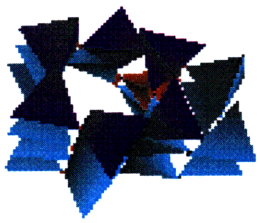

Figure 5.13: 4 sample local clusters from 1000 tetrahedra model of a-Si_3N_4 .

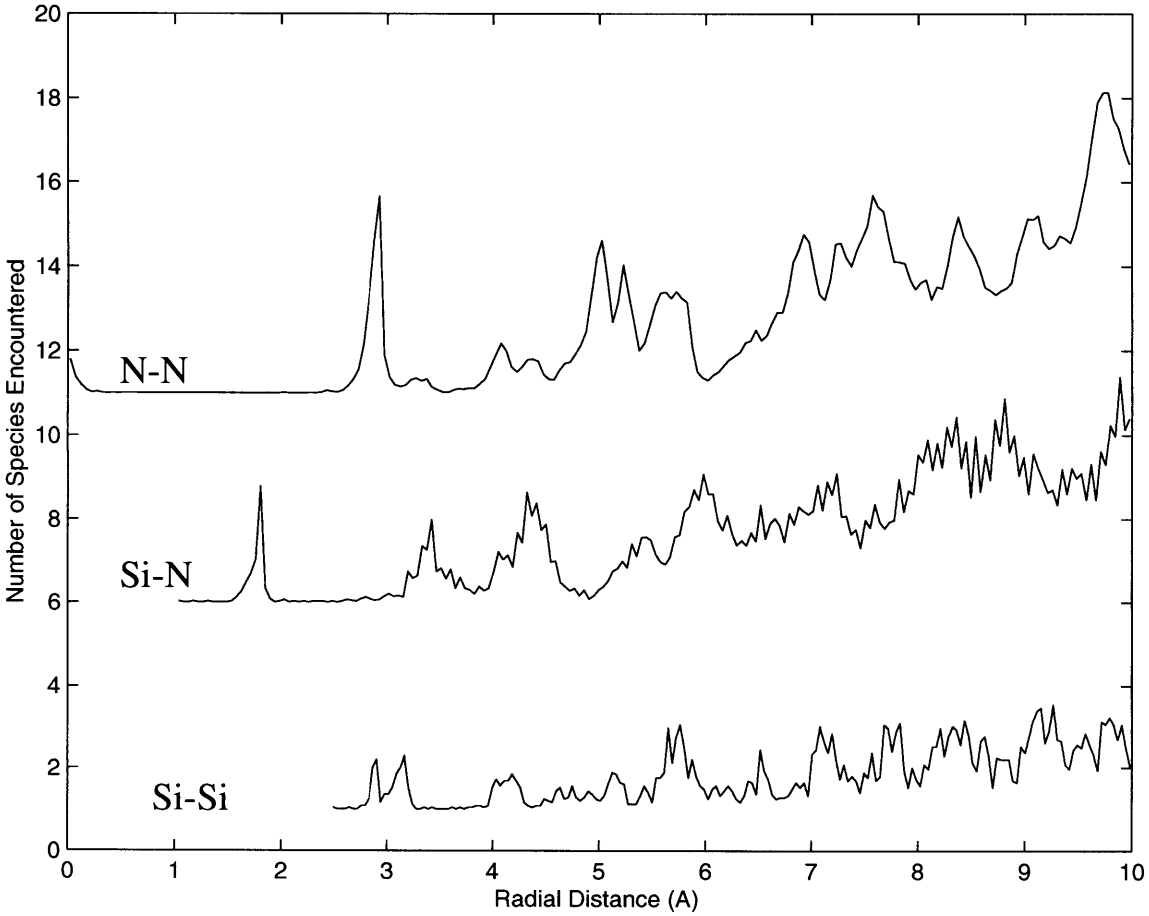

Figure 5.14: Radial distribution function for a-Si_3N_4.

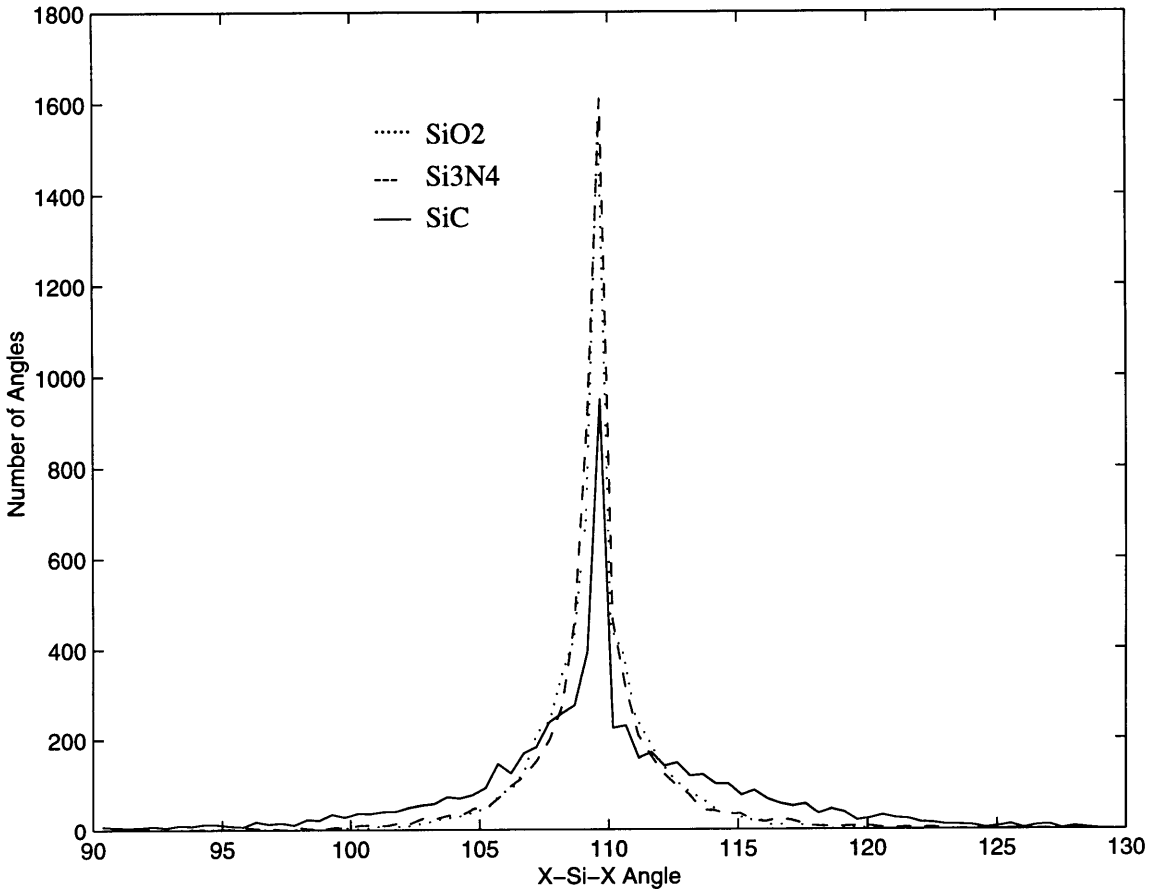

Figure 5.15: X-Si-X bond angle distributions for amorphous structures.

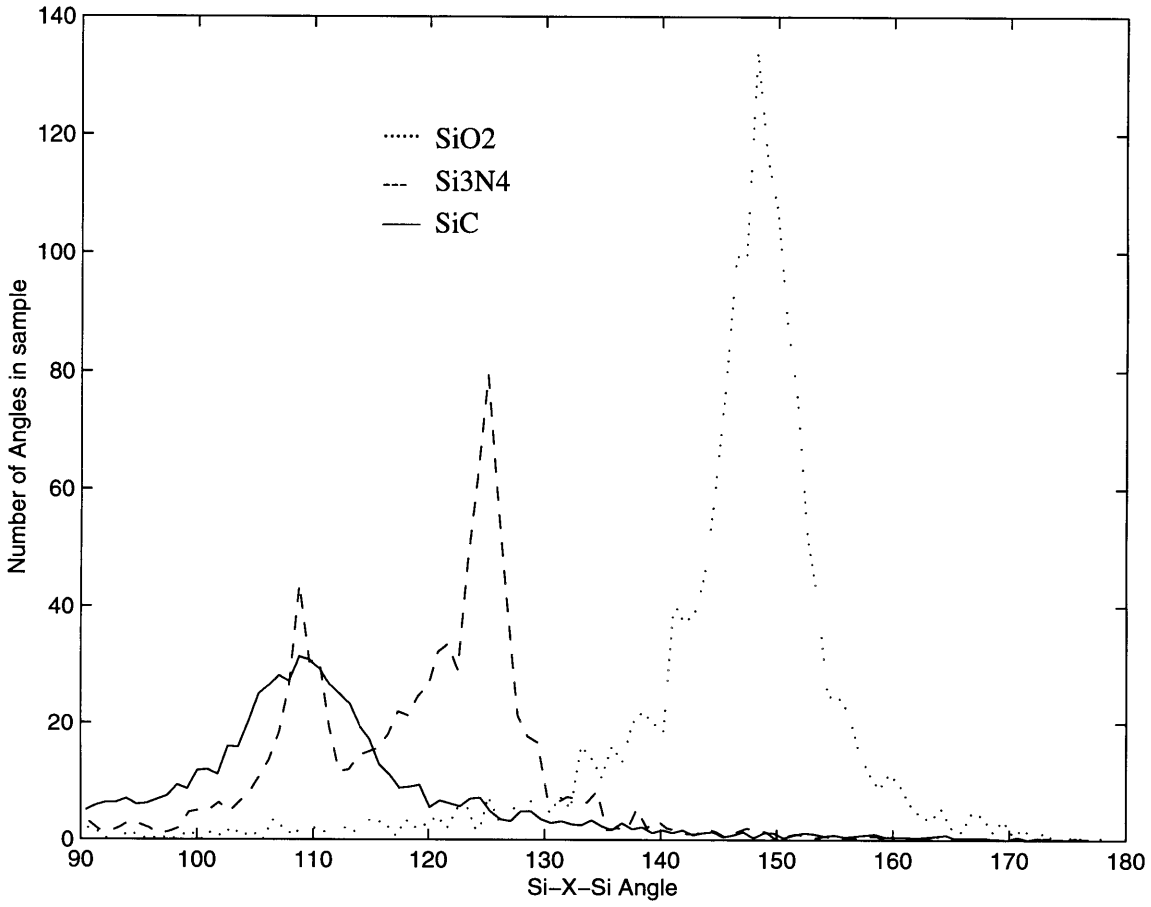

Figure 5.16: Si-X-Si bond angle distributions for amorphous structures.

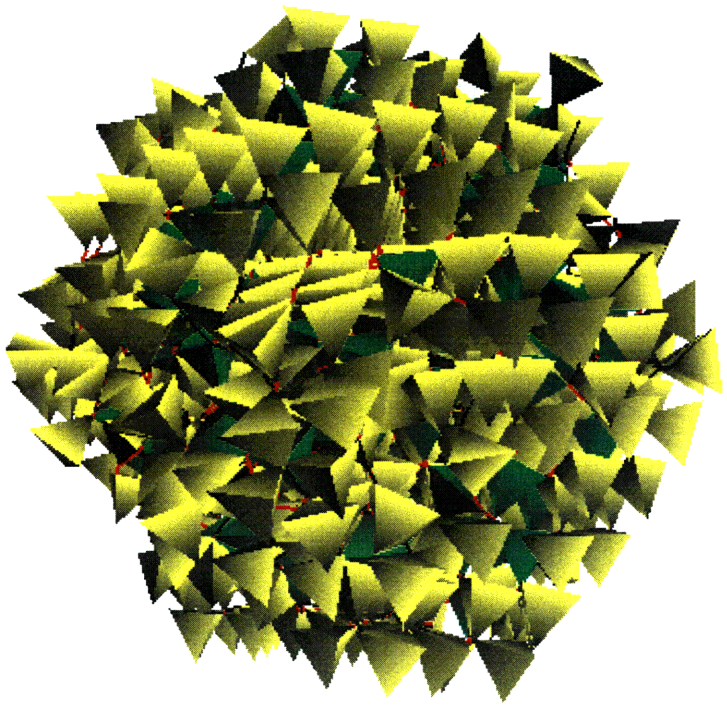

Figure 5.17: 1000 tetrahedra model of a-SiC using the rules in Figure 3.15.

Node 94:

20 tetrahedra
11 3-rings
16 4-rings
4 5-rings

12,43,90

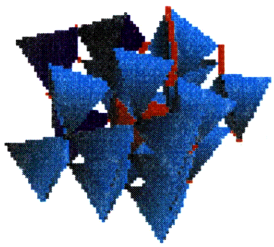

Node 248:

29 tetrahedra
9 3-rings
13 4-rings
21 5-rings

11,41,77

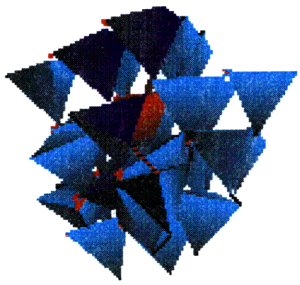

Node 496:

25 tetrahedra
5 3-rings
5 4-rings
25 5-rings
2 6-rings

8,30,71

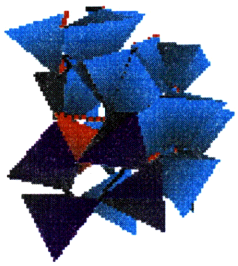

Node 619:

16tetrahedra
9 3-rings
34-rings
4 5-rings

12,34,59

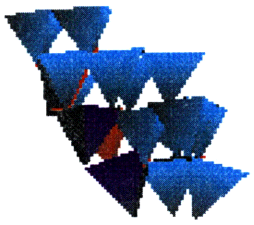

Figure 5.18: 4 sample local clusters from 1000 tetrahedra model of a-SiC .

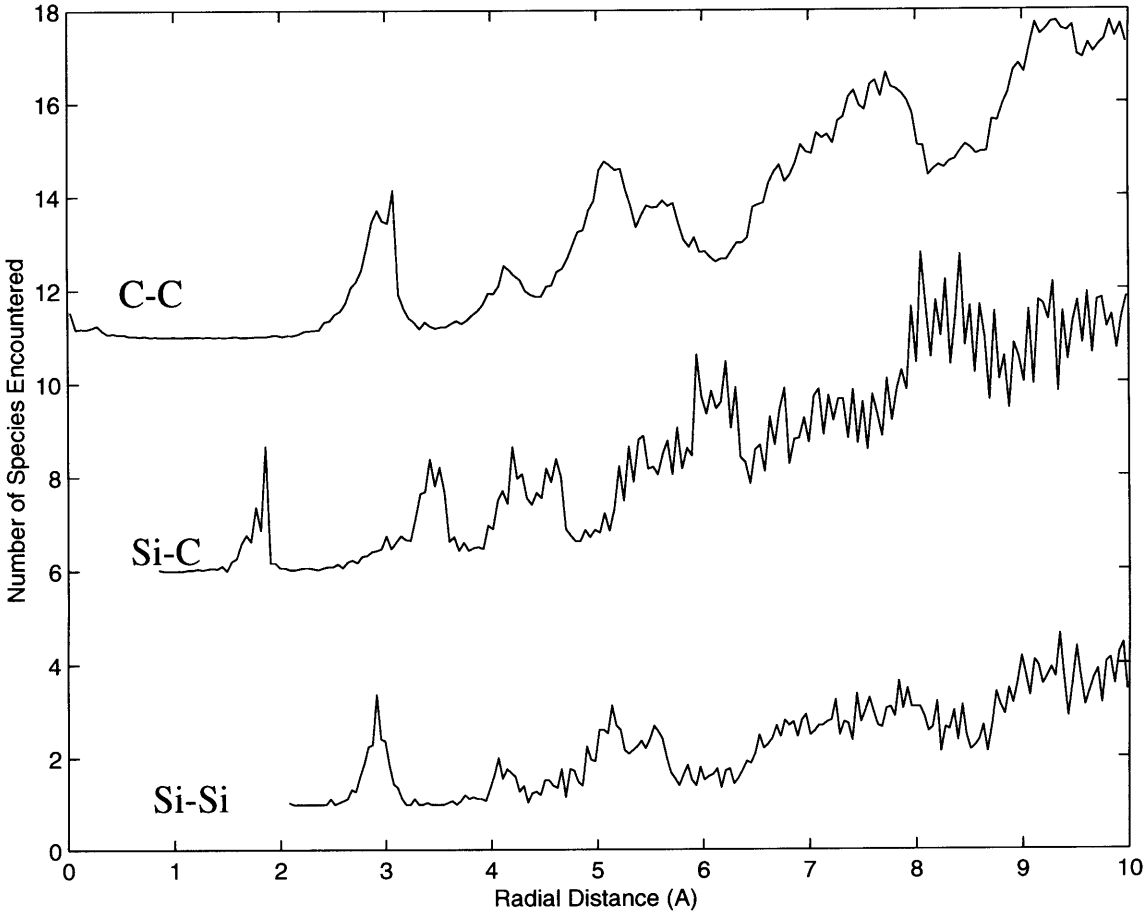

Figure 5.19: 4 sample local clusters from 1000 tetrahedra model of a-SiC .

Model	**0**	1	2	3	4	5	6	7	8	9	10	11	Σ
a-Quartz	**73.6**	3.9	9.1	13.4									**26.4**
a-cristobalite	**62.4**	9.8	8.7	19.1									**37.6**
a-Si_3N_4	**60.3**	5.5	1.1	0.2	0.9	8.7	14.7	2.9					**39.7**
a-SiC	**49.7**	11.7	4.0	1.2	0.6	0.1	0.8	1.6	6.2	8.4	9.6	6.1	**50.3**

Table 5.1: Percent underconnected tetrahedra in amorphous network models.

Polymorph/Regrowth	Average Si-O-Si Angle	Average Ring Size	Average Local Cluster Size	Model Density $\times 10^3$ kg/m^3	Actual Density $\times 10^3$ kg/m^3
α-Cristobalite	145.3	6	29	2.33	2.33
β-Cristobalite	148	6	29	2.17	2.21
α-Quartz	143.6	7.7	63	2.77	2.65
β-Quartz	150.9	7.7	63	2.51	2.53
ideal Quartz	155.6	7.7	63	2.37	–
Vitreous Silica	145	~6 ?	–	–	2.21
Cristobalite-like a-SiO_2	145.9	6.6	24.0	2.29	–
Metamict Silica	134	–	–	–	2.26
α-Cristobalite/β-Cristobalite	142.3	7.0	31.9	2.44	–
α-Quartz/β-Quartz	140.6	7.6	40.0	2.77	–
ideal-Quartz/α-Cristobalite	145.3	7.4	38.7	2.75	–
a-SiO_2/a-SiO_2	138.3	7.4	36.7	2.49	–

Table 5.2: Inter-tetrahedral Bond Angles and Densities for Silicas Modeled

Polymorph/Regrowth	Average Si-X-Si Angle	Average Ring Size	Average Local Cluster Size	Model Density $\times 10^3$ kg/m^3	Actual Density $\times 10^3$ kg/m^3
α-Si_3N_4	118.3	5.0	34.5	3.22	3.20
β-Si_3N_4	119.8	5.2	27	3.20	3.20
a-Si_3N_4	119.6	5.0	25	3.43	–
β-Si_3N_4/β-Si_3N_4	120.2	5.4	31.3	3.32	–
α-SiC	109.5	3.5	19	3.24	3.22
β- SiC	109.5	3.5	19	3.21	3.22
a-SiC	112.0	4.1	22.5	3.25	–
α-SiC/α-SiC	115.6	4.3	26.5	4.57	–

Table 5.3: Inter-tetrahedral Bond Angles and Densities for Si_3N_4 and SiC models.

Polymorph	Node	Si-X-Si Angs.	Average Si-X-Si Angle	Average X-Si-X Angle	Model Density $\times 10^3$ kg/m^3	Actual Density $\times 10^3$ kg/m^3
β-Cristobalite	0	148	148	109.5	2.17	2.21
α-Cristobalite	0	145.3	145.3	109.5	2.33	2.33
Crist.-like a-SiO_2		Crystal basis: 148	146	109.4	2.29	2.20[a]
Quartz-like a-SiO_2		Crystal basis: 155.6	153.7	109.5	2.51	2.26[b]
β-Si_3N_4	0	109.5, 120, 125.1×2	119.8	109.5	3.29	3.20
α-Si_3N_4	0	110.6, 114.2, 117.2, 118.1 118.2, 118.4, 119.6, 124.9	118.3	109.5	3.22	3.20
	1	111.7, 113.1, 116.8, 120.3 120.6, 122.2, 123.0, 124.9				
	2	110.5, 115.6, 116.9, 117.3 117.8, 117.8, 117.8, 124.8				
	3	111.7, 113.1, 117.1, 117.7 117.9, 118.4, 119.6, 124.5				
a-Si_3N_4		Crystal basis: 119.8	119.6	109.5	3.42	-
β-SiC	0	109.5	109.5	109.5	3.21	3.21
α-SiC	0	109.5	109.5	109.5	3.24	3.22
a-SiC		Crystal basis: 109.5	112.0	109.6	3.25	2.86[c]

[a] Vitreous silica, annealed at 1273 K [98]

[b] Neutron-amorphized silica or quartz [98]

[c] Neutron-amorphized α-SiC [114]

Table 5.4: Inter- and intra- tetrahedral angles and densities for rules-generated Si-X polymorphs and cascades

5.2 Modeling amorphization due to a disordering event

We have shown how the basic algorithm will create crystalline network structures. Once we have them created we may manipulate and analyze them. In this section we describe a simple way to model a disordering event such as radiation. We choose a simple approach in which, through a collision cascade, all the bonds in a given neighborhood around some node are broken. This creates a volume of temporary disorder. We may then reform the bonds in this region according to a (possibly new) set of rules as may be appropriate for this excited environment.

Collision cascades in solids result from stopping medium- to heavy-weight incident ions with energies typically in the 1-10 kev/nucleon range or primary knock-on atoms arising from stopping of fast incident neutrons. The cascade displacements are largely uncorrelated and constitute a randomization of constituent atoms, followed (in compounds) by reassembly into chemically-preferred short-range ordered coordination units. The subsequent linking up of these units is likely governed by the same sorts of local rules applying to the long-range assembly of crystals or glass described in Sections 3.1 and 5.1 and therefore modelable in tetrahedral networks by an analogous procedure. For the purposes of modeling, the tetrahedra were assumed to remain intact. Models comprising 2000 tetrahedra were first erected by application of some starting set of local rules (crystalline or amorphizing). A central volume comprising 400 tetrahedra was next chosen in which the connections between all tetrahedra were severed and the bounding periphery expanded. Tetrahedra within the central volume were randomly rotated through angles $< 20°$ and allowed to reform connections according to a chosen set of local rules. The interior and the boundary were finally settled using the optimization scheme described in Section 5.1.

The results of the following cascade experiments will be presented:

- 2000 tetrahedra of α-quartz, 400 tetrahedra regrown using β-quartz rules
- 2000 tetrahedra of α-cristobalite, 400 tetrahedra regrown using β-cristobalite rules
- 2000 tetrahedra of ideal-quartz, 400 tetrahedra regrown using α-cristobalite rules
- 1500 tetrahedra of a-SiO_2 (based on β-cristobalite), 300 regrown using the same rules
- 2000 tetrahedra of α-SiC, 400 tetrahedra regrown using the same rules
- 2000 tetrahedra of β-Si_3N_4, 400 tetrahedra regrown using the same rules

For each the cases above, we will simulate cascade disorder using the model of spinodal decomposition described below. We briefly describe this technique and another possible methodology here.

Spinodal decomposition

This technique involves disordering the region by rotating the nodes by random amounts (between 0 and 20°) and distributing them within the region through the application of some repulsive forces (in order to spread to nodes out as much as possible). If we assume that the tetrahedra will form first, we can simply scatter the tetrahedra (skipping the breaking and reformation of the individual tetrahedra).

Recrystallization by nucleation

Another technique we could adopt for regrowth in the disordered region is akin to nucleation. We could simply regrow the structure from the periphery (outside in) in a similar fashion to the way we normally grow crystals from the inside out, directly from the rules files. This would be like pretending to remove all the tetrahedra from the interior and then putting them all back one at a time.

The difference in these two views of cascade amorphization is operational: In the former, it is the magnitude of the free energy difference between topologically ordered and topologically disordered arrangements which drives epitaxial recrystallization; in the latter, the free energy difference between a far-from-optimal initial disordered arrangement and a more optimal but still topologically disordered arrangement to which the system has subsequent topological access is what drives the third stage and precludes epitaxial recrystallization.

5.2.1 Results of disordering experiments

In the cascade simulations pursued, tetrahedra were assumed for purposes of the modeling to stay intact: they thus comprise the short-range units arising in the second–or rebonding–phase of the cascade. Distortions in the tetrahedra were allowed to develop in response to their reconnection, evidenced in the graphic display by remanent connection springs of non-negligible lengths. A central volume comprising 400 tetrahedra was first chosen, in which the connections between all tetrahedra were initially broken; the periphery adjoining this volume was then expanded, and the tetrahedra within the volume were rotated through randomly selected angles $< 20°$. These "excited" tetrahedra were next allowed to reform connections according to a chosen set of local rules, e.g. a rule set for the same or another crys-

talline polymorph or a modified rule set. The interior and boundary were then settled using the optimization scheme described above.

As a first example, connections between 400 central tetrahedra were destroyed in a 2000-tetrahedra model of α-cristobalite (Figure 5.20a) and the structure regrown using rules for β-cristobalite (Figure 5.21); the choice of a high-temperature polymorphs (β-cristobalite) on which to base the reconstruction rule set was deliberate, since the temperature at which reconstruction is actually effected within a cooling cascade is expected to be high. The result (Figure 5.20b) is an amorphous reconstructed volume, substantially bonded (73%, Table 5.6) both internally and to the crystal boundary, and with little tetrahedral distortion (as evidenced by short remanent optimization springs).

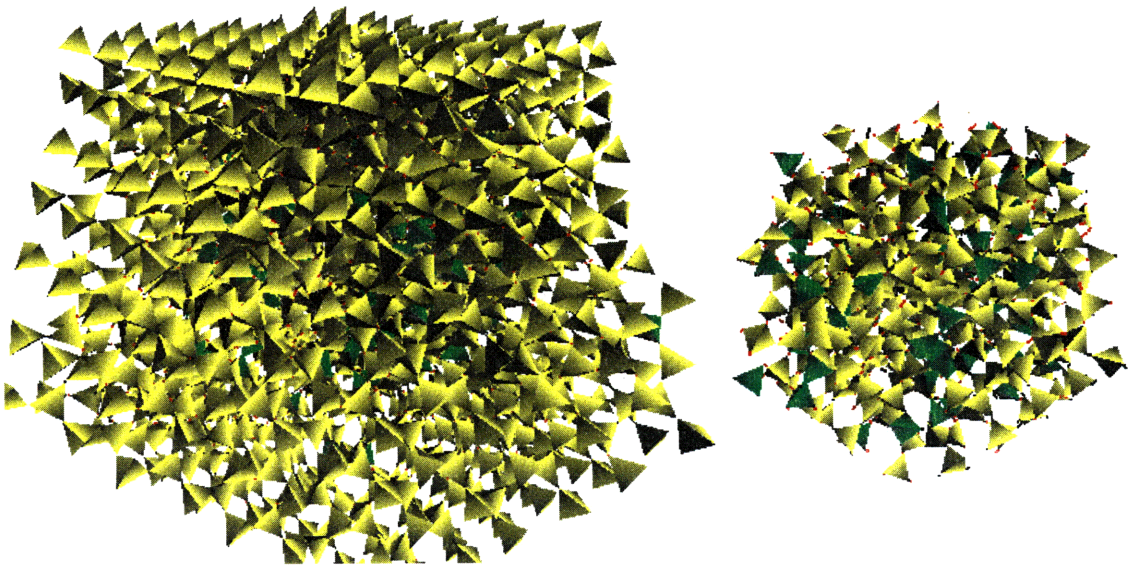

(a) (b)

Figure 5.20: The results from α-cristobalite regrwon using β-cristobalite rules. (a) is the entire resulting structure and (b) is only the regrown region.

An analogous experiment was performed using α- and β-quartz. The resulting structure (Figure 5.22) is substantially bonded (73% as the first experiment) both internally and to the crystal boundary, and also with little tetrahedral distortion.

Using a 2000 node model of ideal-quartz, the central 400 nodes were regrown after disordering using the rules for α-cristobalite (specified in Figure 5.21); the choice of a higher-temperature polymorph (cristobalite) rule set for the regrowth was deliberate (as described above), since the temperature at which reconstruction is actually effected within a cooling cascade is expected to be high. In this case, the specific pair of growth-regrowth rules was chosen to minimize volume changes because ideal quartz and α-cristobalite have identical densities (Table 3.1). The reconstructed region itself is shown separately in Figure 5.23.

```
Beta-Cristobalite
1
4 1
REGULAR
y 23 ;
0 1  z 90 ;
0 0  z -90 ;
0 3  z 90 ;
0 2  z -90 ;
```

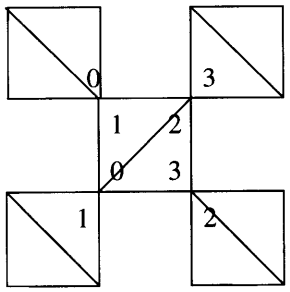


```
Alpha-Cristobalite
1
4 1
REGULAR
y 24.7 ;
0 1  z 90 ;
0 0  z -90 ;
0 3  z 90 ;
0 2  z -90 ;
```

θ = 148°

θ = 145.3°

Figure 5.21: Local rules for β- and α-cristobalite. These differ from the rules for ideal cristobalite only in the initial offset rotation.

An amorphous silica network was also chosen to cascade disorder because it is known that vitreous silica compacts by 2.7% upon fast neutron irradiation to a terminal density identical to that of neutron-amorphized quartz [108]; it was therefore of interest to compare the cascade structures in models approximating these two starting materials. 1500 tetrahedra of amorphous silica were erected, using the modified rules (Figure 5.3) for β-cristobalite, and the central 300 tetrahedra were disordered and regrown using the same rules set as the initial assembly; the initial assembly with its embedded cascade and the reconstructed region itself are depicted in Figure 5.24.

Analysis of silica cascades

Because relaxation of the boundary and optimization of the reconnections occur with no imposed potential, save that effectively supplied by the optimization springs, the computed densities of the final cascade configurations are at best only qualitatively comparable to the experimentally measured terminal density of the metamict condition. The computed densities reported in Table 5.1.4 correctly predict the densification of the a-SiO_2 model (by a somewhat larger amount, 8.7%, than experimental), but not the dilatation of α-quartz, who density has remained the same. Idealized quartz has densified by almost 17%. Perhaps more diagnostically, the data indicate densification of the two cristobalite-based models to about the same terminal density (2.44,2.49) and of the two quartz-based models to a second identical terminal density (2.77, 2.75).

Tetrahedral distortion was small in all four cascades, as evidenced by the small remanent spring lengths at all vertex junctions. The O-Si-O intra-tetrahedron angle distribution was in all cases broadened similarly from the 109.5° ideal tetrahedral angle and also with respect to the smaller angular range for the cristobalite-like a-SiO_2 model (Figure 5.25).

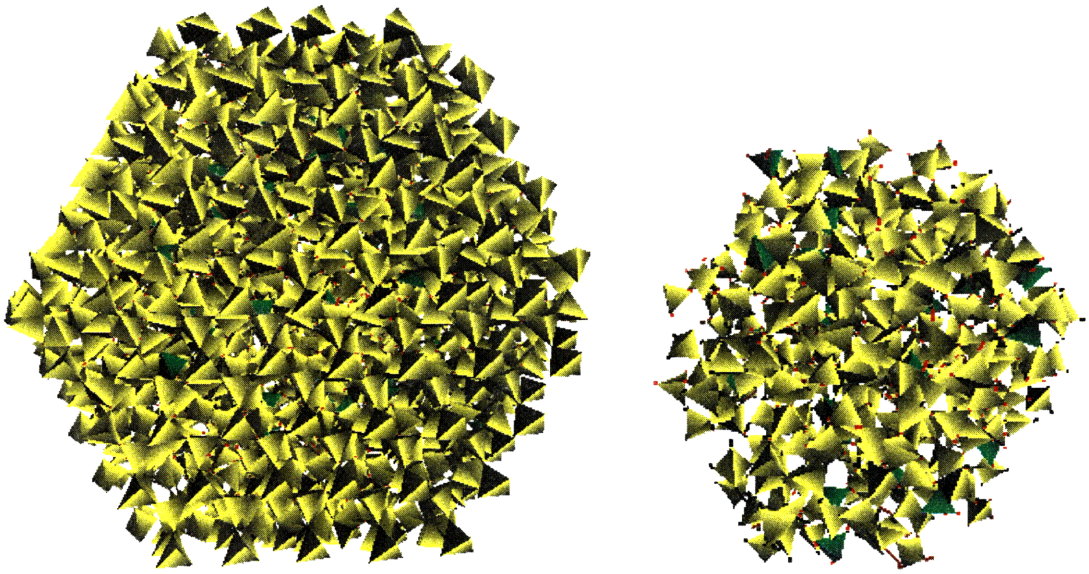

(a) (b)

Figure 5.22: The results from α-quartz regrown using β-quartz rules. (a) is the entire resulting structure and (b) is only the regrown region.

The reassembled tetrahedra were moderately well-connected; many of the most underconnected tetrahedra were sited at the interface where reattachment to the original surrounding network was made. Table 5.6 documents the extent of the underconnection for the cascades.

The distributions of Si-O-Si inter-tetrahedral angles θ were all considerably broader than for the cristobalite-like a-SiO_2 model, and the average θ was consistently and substantially shifted to smaller angles (Table 5.1.4). Figure 5.26 shows that the angular distributions were nearly identical in all four cascades, as were the averages. The peak of the distributions occurred not far from the peak for the a-SiO_2 model but at a significantly larger angle than for a-quartz.

Local clusters were computed for a representative sample of tetrahedra in each cascade. Analysis of these local clusters revealed that those that extended into the interface retained some characteristics of the precursor structure, but those removed from the boundary acquired very different–and surprisingly uniform–topologies. Interior clusters from each of the four cascades, with their tetrahedron complement and ring counts enumerated (see Figures 5.27, 5.28, 5.29 and 5.30). What is surprising is how unlike either precursor or regrowth rules structures these local clusters are; the local clusters are neither cristobalite-like nor quartz-like, but something intermediate in size and ring content and with a notable skew towards larger rings (8-, 9- and 10-rings) at the expense of smaller rings. The ring size distributions obtained by averaging the results for 20 clusters near the cascade centers are plotted in Figure 5.31. The average ring size per cluster and the average cluster size are reported

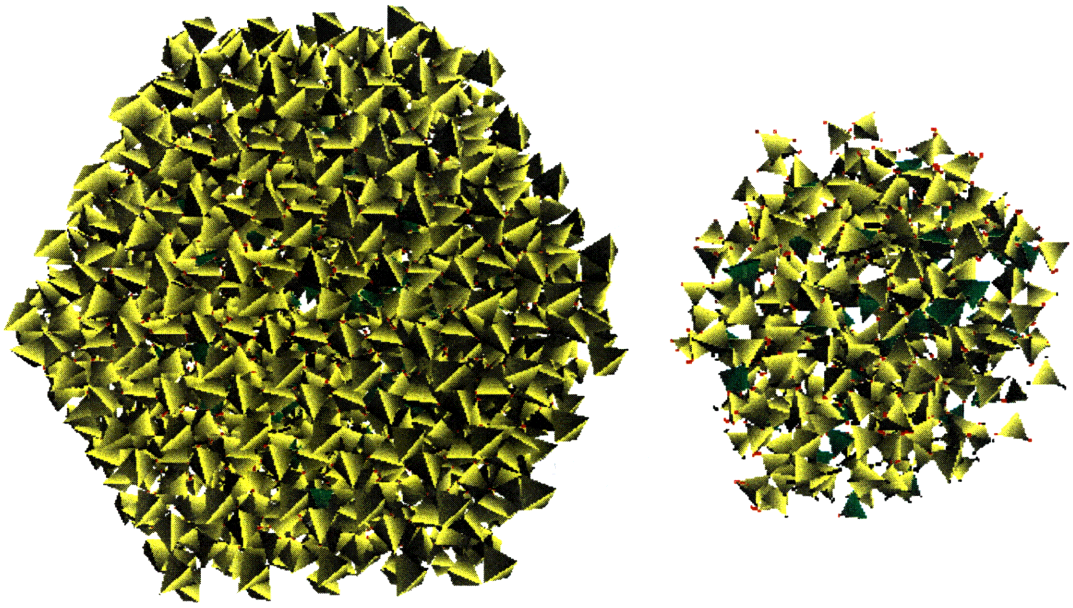

(a) (b)

Figure 5.23: The results from ideal quartz regrown using α-cristobalite rules. (a) is the entire resulting structure and (b) is only the regrown region.

in Table 5.1.4; both statistics are remarkably similar for each of the cascades and distinctly different from any of the three precursors.

Partial radial density functions (RDFs) for Si-O, O-O and Si-Si pair correlations were computed by averaging results from 50 tetrahedra randomly chosen from the centermost 10% of the cascades. The computed RDFs were all close to being identical. Figure 5.32 compares those for the a-quartz/b-quartz and the cristobalite-like glass cascades.

5.2.2 Cascades results for Si_3N_4 and SiC

To illustrate the difficulties in amorphizing Si_3N_4 and SiC (difficult because of structural freedom constraints illustrated in Chapter 2) we have simulated cascade amorphization of β-Si_3N_4 and α-SiC using the precursor rules to regrow the cascade region in both cases. These experiments are to be compared to the silica cascade experiments to illustrate the relative difficulties in amorphization of structures having $f < 0$ and silica ($f = 0$).

Figures 5.33 and 5.34 show cascade simulations for β-Si_3N_4 and α-SiC regrown with the same rules. Whereas all SiO_2 cascades were fairly well re-connected and exhibited little distortion, the regrowth volumes in β-Si3N4 and α-SiC were more poorly connected (Table 5.6), exhibiting a larger fraction of underconnected tetrahedra (39% and 44% respectively vs. 27% for SiO_2), both at the boundary and in the interior; amorphized regions for

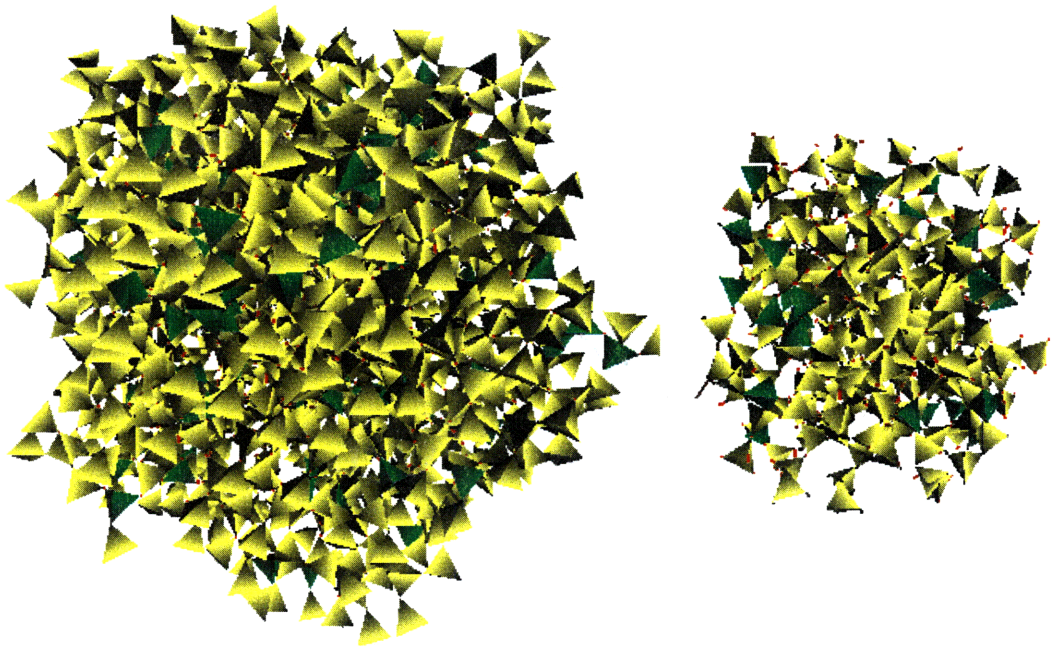

(a) (b)

Figure 5.24: The results from cristobalite-like glass regrown using the same rules. (a) is the entire resulting structure and (b) is only the regrown region.

β-Si_3N_4 and α-SiC also exhibited large optimization springs, corresponding to large tetrahedron distortions. Further optimization did not significantly decrease the underconnection or connection spring lengths.

Local clusters (Figures 5.35 and 5.36) extracted from the cascade-amorphized volumes in both simulations revealed topologies much farther removed from their precursors than in corresponding amorphous structures assembled using crystal rules modifications alone. Local clusters incorporating tetrahedra residing at the periphery mostly retained their precursor topologies (e.g., node 467 in Figure 5.35, node 532 in Figure 5.36), but those in the cascade interior developed different ring configurations. The local clusters in cascade-amorphized α-cristobalite (Figure 5.27, while substantially different from that of their crystalline precursor, nevertheless remained silica-like with little distortion, strongly resembling the local clusters of other cascade-amorphized silicas. In contrast, those in the interior of the cascades in β-Si_3N_4 and α-SiC (Figures 5.35 and 5.36) were not at all Si_3N_4- or SiC-like and exhibited large distortions.

Figure 5.37 plots the distributions of Si-X-Si inter-tetrahedral angles θ for three compounds (Si_3N_4, SiC and the α-cristobalite cascade), which are considerably broadened and shifted from the corresponding angles (Table 5.5) for α-cristobalite (145.3°), β-Si_3N_4 (109.5°, 120°, 125.1° for a 119.8° average) and a-SiC (109.5°). In particular, the average angle for

Precursor/Regrow	Si-X-Si Angles for Precursor/Regrow	Average Si-X-Si Angle in Cascade	Average X-Si-X Angle in Cascade	Cascade Density $\times 10^3$ kg/m^3
α-Cristobalite/β-Cristobalite	145.3/148	139.9	109.5	2.44
α-Quartz/β-Quartz	143.6/150.9	140.0	109.5	2.77
ideal-Quartz/α-Cristobalite	155.6/145.3	138.5	109.5	2.75
a-SiO_2/a-SiO_2	146	138.3	109.5	2.49
β-Si_3N_4/β-Si_3N_4	Avg. 119.8	120.2	110.2	3.32
α-SiC/α-SiC	109.5	115.6	110.2	4.57

Table 5.5: Si-X-Si inter-tetrahedral and X-Si-X intra-tetrahedral angles, and cascade densities for amorphized SiO_2, Si_3N_4 and SiC models.

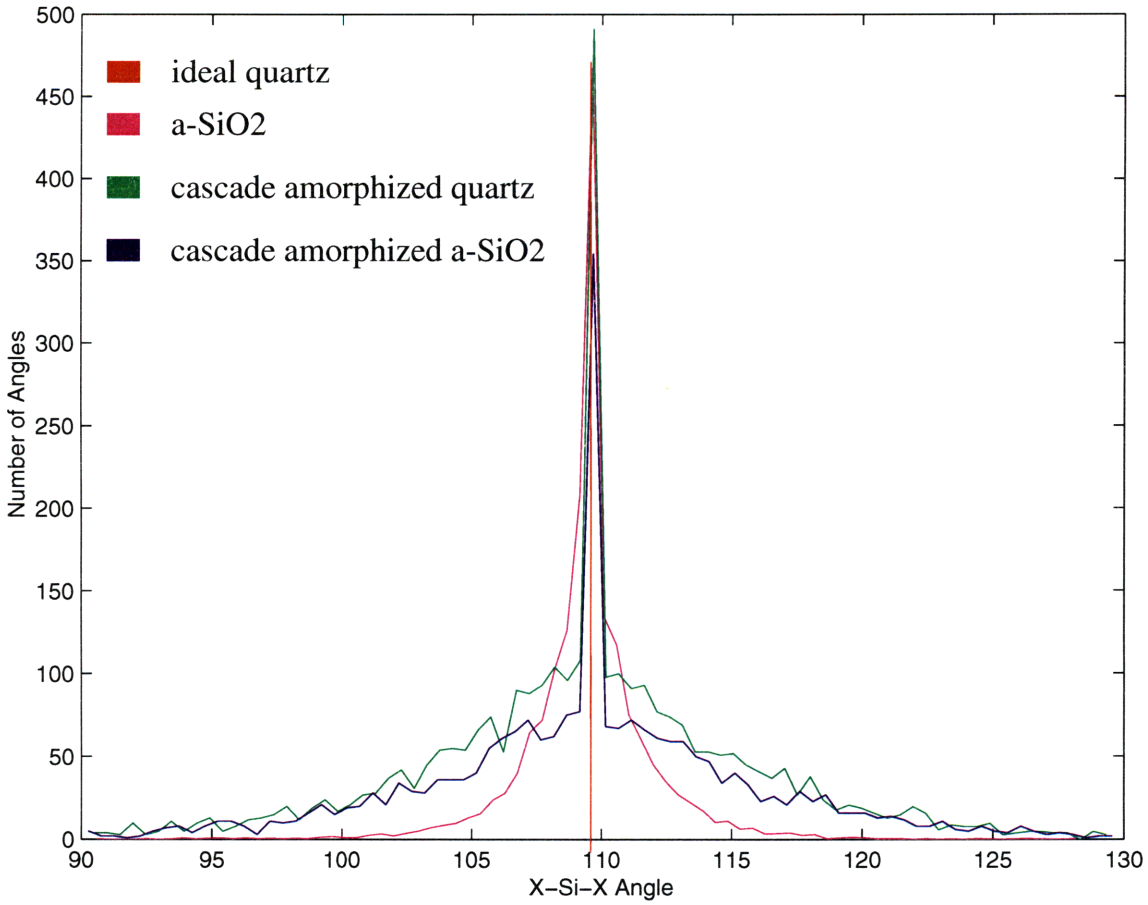

Figure 5.25: O-Si-O tetrahedral bond angle distribution for crystalline α-quartz, a-SiO_2 grown with modified β-cristobalite rules, and their respective cascades.

the SiO_2 cascade decreases from that of either precursor or regrowth template, while in Si_3N_4–to the extent that remnant evidence of the three distinct Si-N-Si angles in the crystalline precursor remain–the average of the broadened angular distribution about each increases. The extreme Si-X-Si angles ($\theta \ll$ the 109.5° tetrahedral angle) in the angle distributions for Si_3N_4 and SiC amorphized models render the configurations produced sterically unattractive.

The X-Si-X intra-tetrahedral angles are similarly plotted in Figure 5.38, and while the average angles for all three networks are close to the ideal tetrahedral angle of 109.5°, the distribution is enormously wider for Si_3N_4 and SiC than for SiO_2 and represents unacceptable definition of tetrahedral units. The Si-C-Si inter-tetrahedral angle θ (average 115.6) for [SiC_4] tetrahedra in cascade-amorphized SiC is also of interest in this context, because this angle is as well the intra-tetrahedral angle for equivalent [CSi_4] tetrahedra, again implying a considerable net tetrahedral distortion in this cascade-amorphized structure.

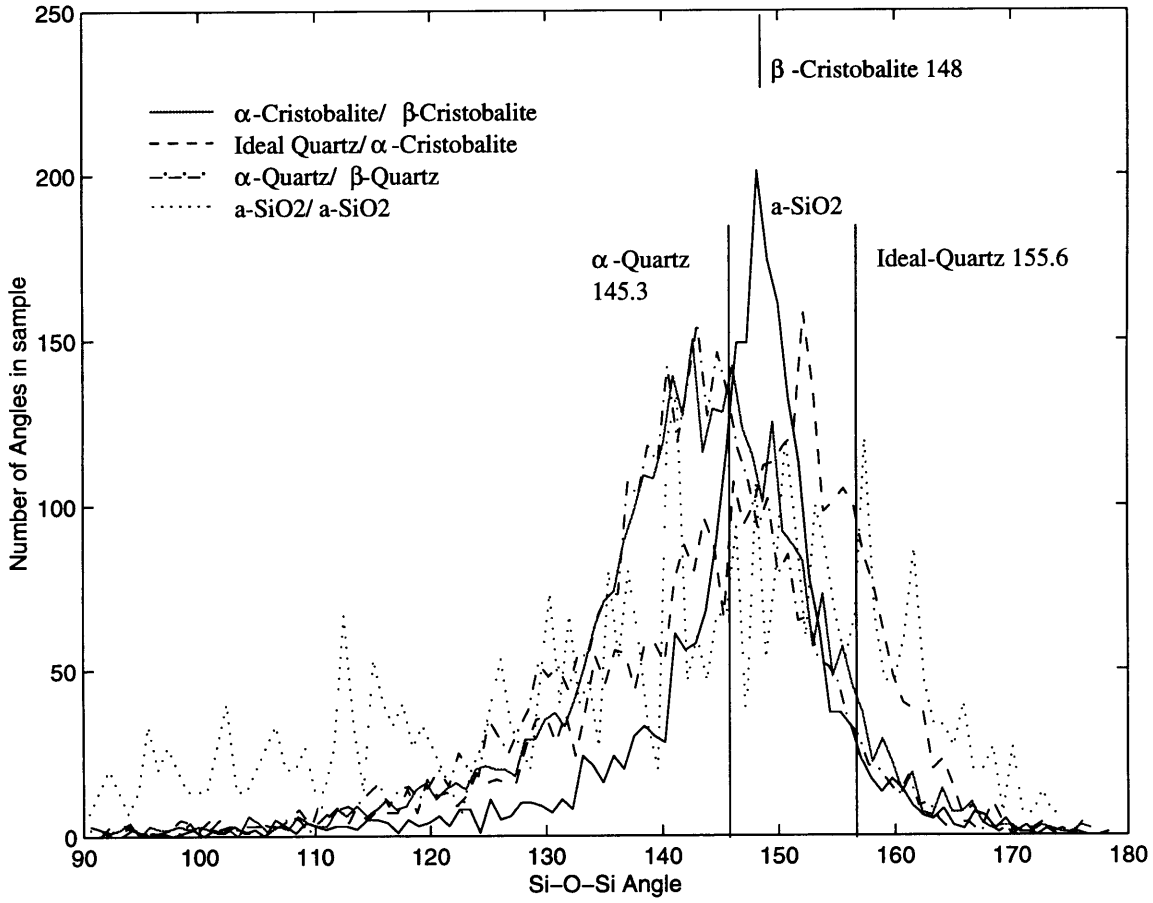

Figure 5.26: Si-O-Si inter-tetrahedral bond angle distribution for cascade-amorphized a) α-cristobalite, b) α-quartz, c) ideal-quartz and d) cristobalite-like a-SiO_2, compared to the distribution for the as-grown a-SiO_2 and the crystal bond angles.

Computation of a final density for the model cascades provides only qualitative comparisons, because the cascade density may depend to some extent on the arbitrary expansion of the surrounding matrix material imposed in the cascade simulation process. The initial disordering rotations do take place in a nominally stress-free state; the regrowth is, however, subject to the forces imposed by the optimization springs in both the regrown region and the surrounding matrix. Final densities of the cascade regions were computed using techniques described in Chapter 3, only limited to the regrown region, and the results are presented in Table 5.5. The density of the silica cascade (2.44) is only 5% different from that of its α-cristobalite precursor model (2.33), while the Si_3N_4 cascade is about 14% denser (3.32) than its β-Si_3N_4 precursor model (2.91). The anomalously high value (42% larger) for the SiC cascade density (4.57) compared to the crystal value (3.21) reflects the great difficulty in avoiding steric overlaps in the attempt at rebonding after the initial imposed disorder in this highly over-constrained structure.

Node 38:

37 tetrahedra

1 6-rings
8 7-rings
3 8-rings
4 9-rings

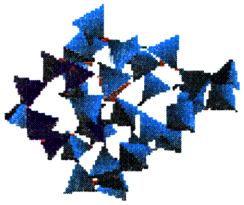

Node 237:

45 tetrahedra

1 4-ring
1 6-rings
1 7-ring
4 8-rings
5 9-rings
1 10-ring

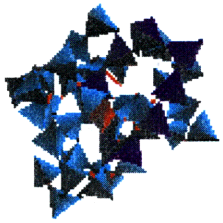

Node 358:

42 tetrahedra

2 6-rings
1 8-ring
3 9-rings
7 10-rings

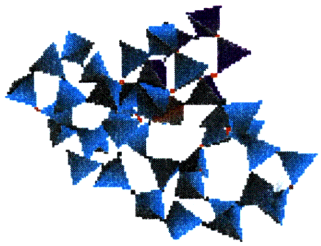

Node 745:

29 tetrahedra

12 6-rings

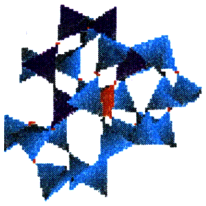

Figure 5.27: Local clusters from α-cristobalite regrown using β-cristobalite rules.

Radial correlation density functions were computed for cascades in all three compounds, using the method described earlier (Chapter 4) which involved averaging correlation data for 50 tetrahedra randomly chosen from a cascade. The results (Figures 5.39 and 5.40) are plotted as Si-X, Si-Si and X-X partial radial correlations. The correlations obtained for the cascade in α-cristobalite regrown with β-cristobalite rules are compared in Fig. 13 to those for crystalline β-cristobalite, represented as triangular peaks rather than δ-functions. The Si-O and O-O short-range correlations, corresponding to the [SiO_4] tetrahedron, are identical, but the intermediate-range correlations (Si-Si and longer-range Si-O and O-O correlations) in the amorphized cascade region only vaguely reflect those of the crystal and reproduce the principal features appearing in radial density functions of several neutron- and electron-amorphized crystalline silica polymorphs derived from diffraction measurements [110, 135]. (Nearly identical correlation results are obtained for cascade models with other starting configurations of SiO_2 regrown with a variety of rules , suggesting a common endpoint for other cascade-disordered silicas.)

The radial correlation plots for cascade-amorphized β-Si_3N_4 and α-SiC models, reproduced in Figures 5.39 and 5.40, are by contrast almost featureless beyond the short-range correlations within the coordination tetrahedra, corresponding to nearly random arrangements of tetrahedra without distinguishable intermediate-range structure. (The anomalous apparent saturation in the SiC plots (Fig. 15) is due to the small spatial extent of the cascade:

Node 2:

51 tetrahedra

1 3-ring
1 6-ring
3 7-rings
2 8-rings
16 9-rings
1 10-ring

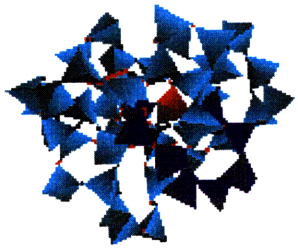

Node 168:

41 tetrahedra

1 3-ring
1 4-ring
1 6-ring
11 8-rings
1 9-ring

2 10-rings

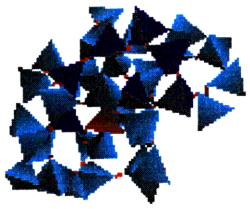

Node 477:

37 tetrahedra

3 6-rings
13 8-rings

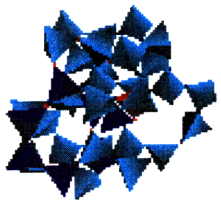

Node 592:

56 tetrahedra

6 6-rings
33 8-rings

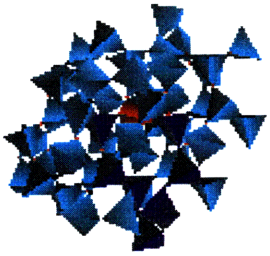

Figure 5.28: Local clusters from α-quartz regrown using β-quartz rules.

for the same number of tetrahedra in the cascade model, the cascade volume in SiC is physically smaller than the cascades volumes of SiO_2 or Si_3N_4 because of the higher density of SiC, for which the 1-nm correlation distances begin to exceed the cascade radius.)

5.3 Topological implications for amorphizability

The assembly procedure outlined for generating amorphous structures from SiO_2, Si_3N_4 and SiC provide some insights into the respective amorphizabilities of the three compounds. Substantial topological disorder is relatively easy to propagate in {4,2}-connected silica, for even modest deviations from crystalline assembly rules and collision cascade reconstructions. The resulting amorphous assemblages were substantially connected and exhibited little tetrahedral distortion. The explanation can be seen in the considerable multiplicity of options afforded in these marginally-connected networks, in particular the independence of the inter-tetrahedral Si-O-Si angles from each other and from the O-Si-O intra-tetrahedral angles.

Node 30:

47 tetrahedra

2 5-ring
3 7-rings
5 8-rings
3 9-rings
1 10-ring

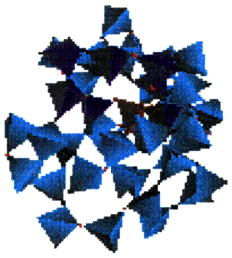

Node 188:

34 tetrahedra

2 4-rings
3 6-rings
6 8-rings
5 10-rings

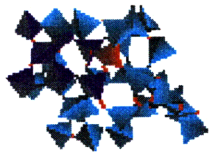

Node 282:

34 tetrahedra

1 3-ring
1 4-ring
3 7-rings
3 8-rings
3 9-rings
1 10-ring

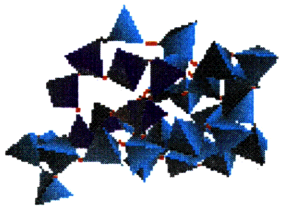

Node 562:

54 tetrahedra

4 6-rings
1 7-ring
22 8-rings
1 9-ring

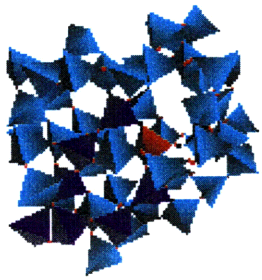

Figure 5.29: Local clusters from ideal quartz regrown using α-cristobalite rules.

It appears possible to propagate topological disorder also in Si3N4 assemblies with the same extent of rules deviation, the resulting arrangements suffering from about the same underconnection and tetrahedral distortion as for silica, in agreement with molecular dynamics simulations [121]. But the overall amorphized Si_3N_4 structure is seen to remain much more crystal-like than silica, doggedly retaining many of the same intermediate and long-range correlations exhibited by its crystalline analogue. The local clusters, while topologically distinct and incorporating some new elements, do not stray far from the local cluster of the crystalline arrangement. The difficulty in amorphizing Si_3N_4 by irradiation may lie in this reluctance to cede intermediate- or long-rang order, or in related problems associated with acceptable reconnection following cascade randomization.

By contrast, topological disorder in SiC proved difficult to propagate acceptably, even in assembly models with only modest rules deviations applied. As with Si_3N_4, though the local topology developed a new element (dominant 5-rings in this case), the propagation attempt retained most of the intermediate-range correlations of the crystalline form on which the rules are based. Assembly was accomplished only at an accompanying (and probably energetically unacceptable) cost of substantial underconnection and large tetrahedral dis-

Node 91:

56 tetrahedra

1 5-ring
6 5-rings
3 8-rings
2 9-rings
8 10-rings

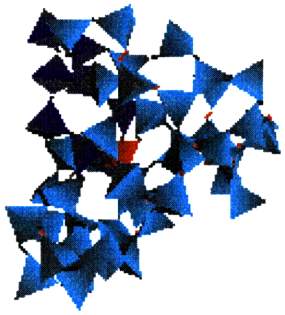

Node 115:

43 tetrahedra

2 6-rings
7 5-rings
3 8-rings
3 9-rings

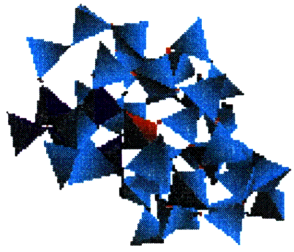

Node 164:

35 tetrahedra

1 5-ring
1 6-ring
3 7-rings
8 9-rings

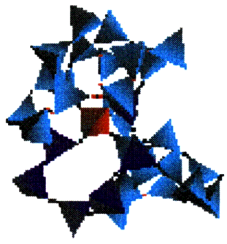

Node 243:

41 tetrahedra

1 4-ring
4 6-rings
3 7-rings
3 8-rings
1 10-ring

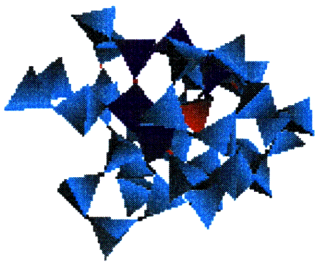

Figure 5.30: Local clusters from cristobalite-like glass regrown using the same rules.

tortion. It is clear that one reason is strong interdependence of the four Si-C-Si angles at a given vertex and the interrelation of the Si-C-Si and C-Si-C tetrahedral angles for the 4,4 connectivity. As indicated earlier (Chapter 2), both α and β forms of SiC nevertheless amorphize under irradiation almost as readily as do crystalline silicas, with an ease very much at variance with the predictions of topological freedom and also with the results of the present modeling study, both of which imply great difficulty in propagating topological disorder in chemically ordered SiC. The admission of chemical disorder as a possibility substantially alters the topological basis assumed for the modeling, as well the likely result.

The similarity of angular distributions and local cluster topologies for the amorphized models of ideal quartz and a-SiO_2 derived from β-cristobalite may give a topological basis to the experimentally observed identical terminal densities of neutron-amorphized quartz and vitreous silica. The cascade results presented here for silicas are far more similar than the corresponding amorphous silicas produced from assembly-rule modifications alone Section 5.1, whose structures adhere more closely to their crystalline antecedents. We speculate that the initial random rotations in the cascade simulation produce a more common starting point for reconnection, which reconnection is then less affected by differences in the reassembly rules imposed.

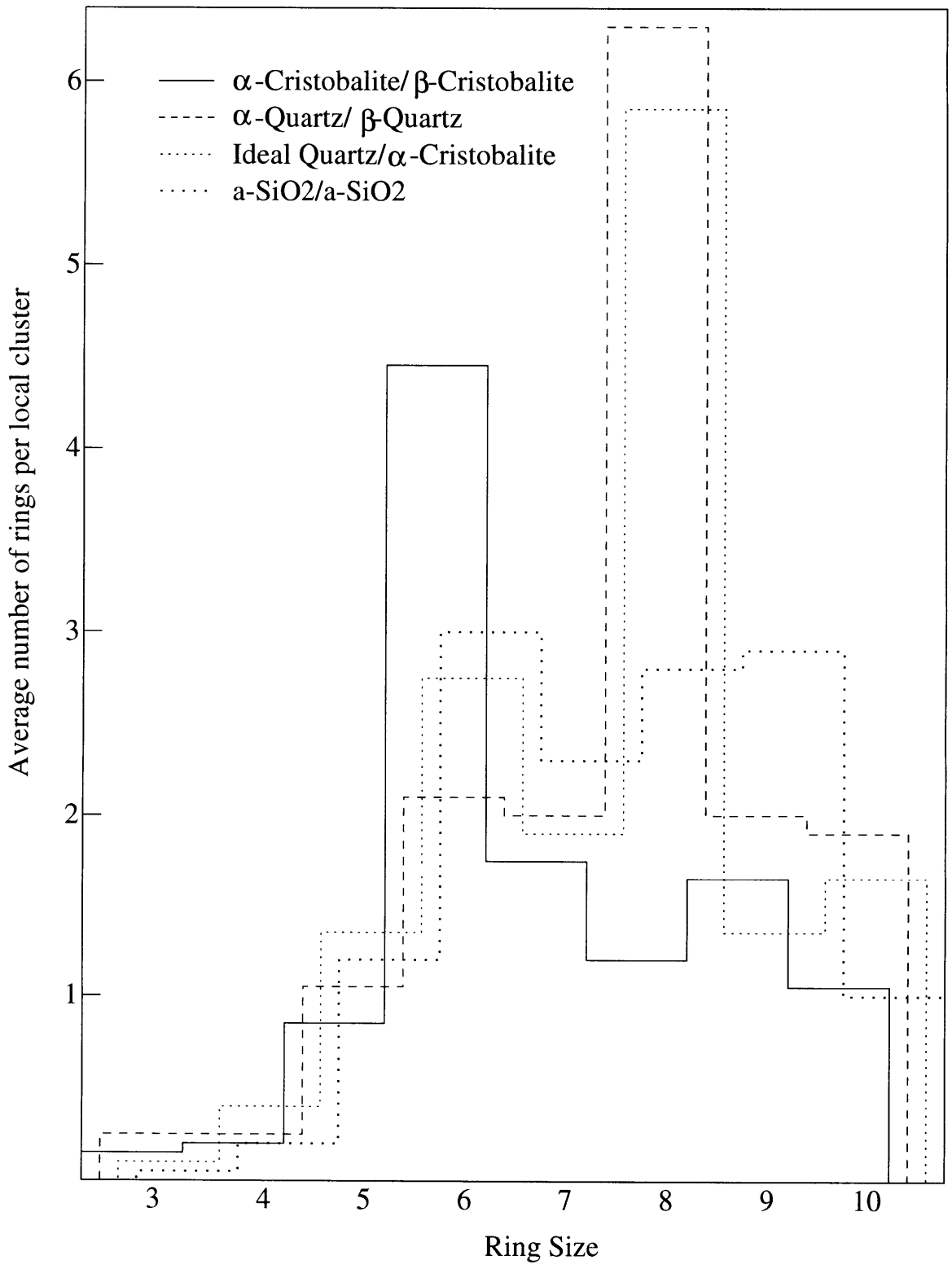

Figure 5.31: Histogram of primitive ring size distributions in local clusters of the four cascade-amorphized silicas described above.

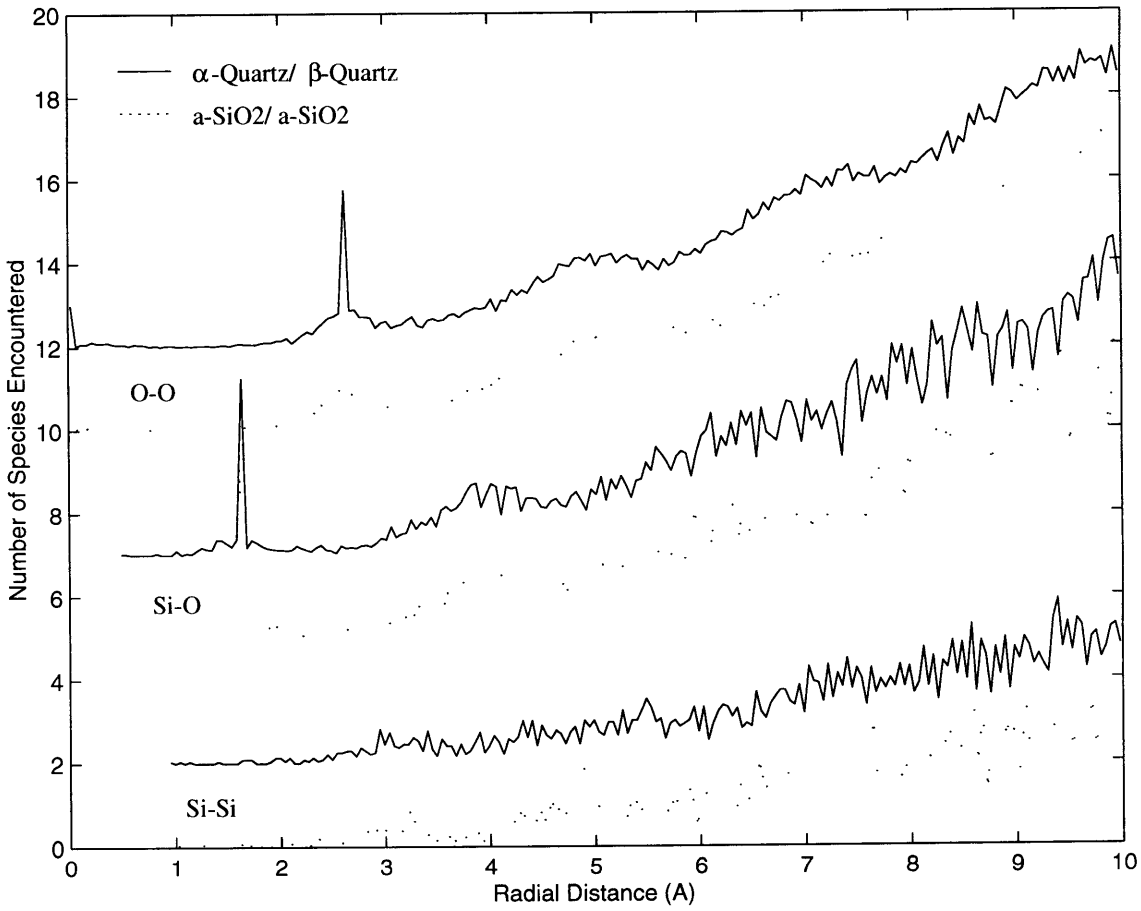

Figure 5.32: Partial radial density functions for O-O, Si-O and Si-Si correlations in cascade-amorphized α-quartz regrown with β-quartz rules and amorphous silica grown with modified β-cristobalite rules and regrown with the same rules.

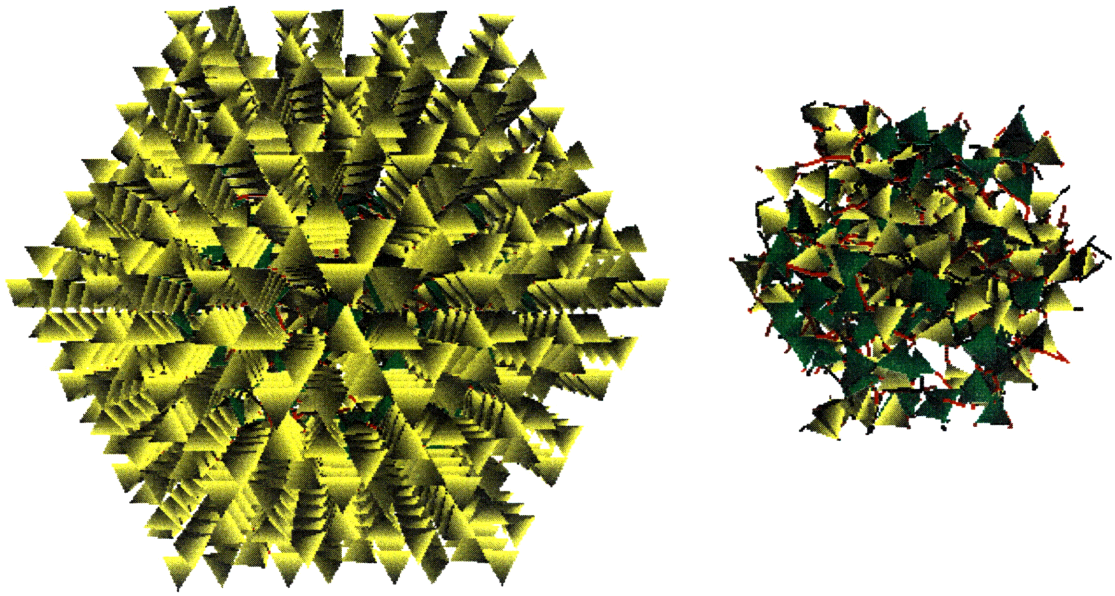

(a) (b)

Figure 5.33: Cascade simulation for a a) 2000 tetrahedra of β-Si_3N_4 in which b) the embedded central 400 tetrahedra have been disordered and rebonded using β-Si_3N_4 rules. Many underconnected tetrahedra (green) and large remanent optimization spring segments (red) remain.

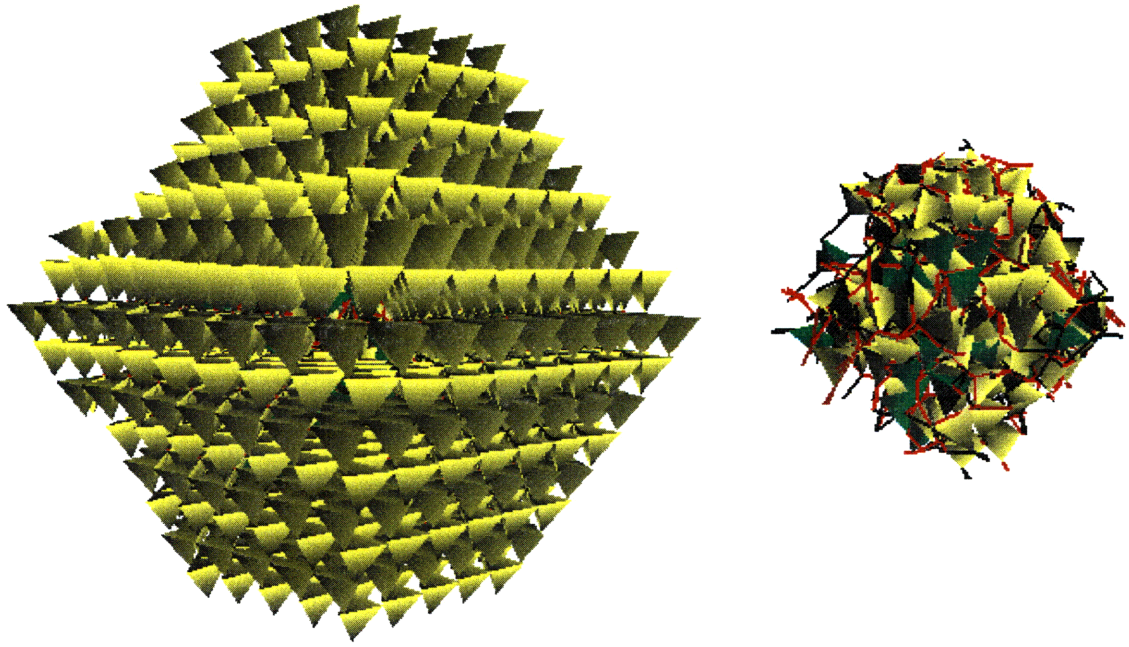

(a) (b)

Figure 5.34: Cascade simulation for a a) 2000 tetrahedra of α-SiC in which b) the embedded central 400 tetrahedra have been disordered and rebonded using α-SiC rules. Many underconnected tetrahedra (green) and large remanent optimization spring segments (red) remain.

Node 25:

37 tetrahedra
1 3-rings
7 4-rings
3 5-rings
8 6-rings
5 7-rings

8,28,57

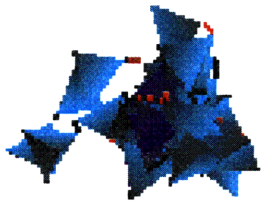

Node 467:

27 tetrahedra
4 3-rings
3 4-rings
3 5-rings
20 6-rings

8,29,67

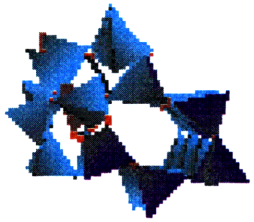

Figure 5.35: Four representative Si_3N_4 local clusters from the final β-Si_3N_4 cascade configuration in Figure 5.33b from near the center and near the periphery, with their near neighbor counts. Node 467 near the periphery is β-Si_3N_4-like, node 25 near the center very unlike its precursor.

Node 178:

20 tetrahedra
6 3-rings
13 4-rings
33 5-rings
9 6-rings

12,46,96

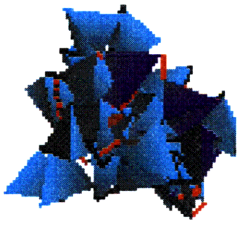

Node 532:

27 tetrahedra
10 3-rings
7 4-rings
8 5-rings
1 6-ring

11,41,91

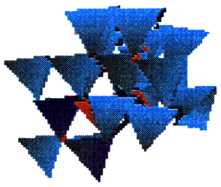

Figure 5.36: Four representative SiC local clusters from the final α-SiC cascade configuration in Figure 5.34b. Node 532 near the periphery is SiC-like, node 178 nearer to the center decidedly not.

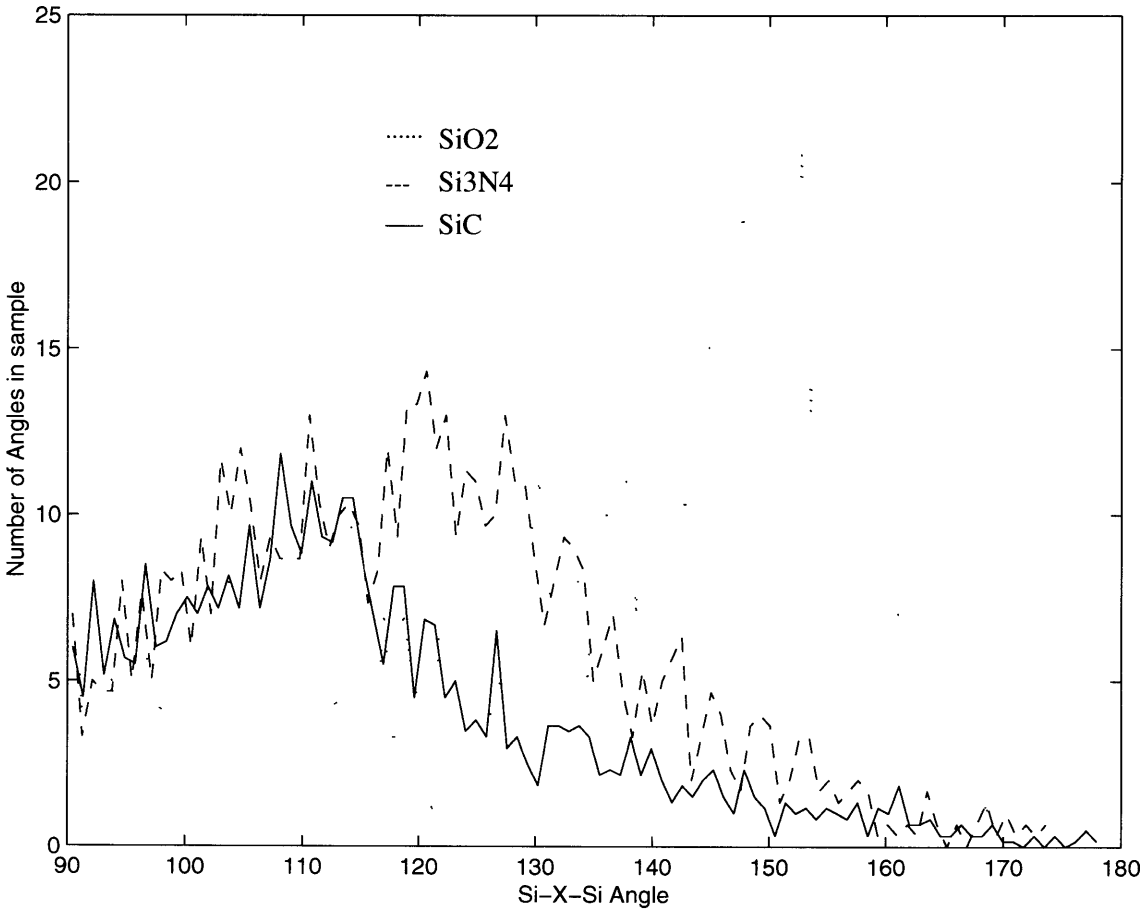

Figure 5.37: Distribution of Si-X-Si inter-tetrahedral angle for the cascade-amorphized regions in α-cristobalite SiO_2, β-Si_3N_4 and α-SiC. The larger overall number of angles for {4,3} Si_3N_4 and {4,4} SiC has been accounted for by normalizing their distributions to that for {4,2} SiO_2 by dividing the number of angles in their distributions by 3 and 6 respectively.

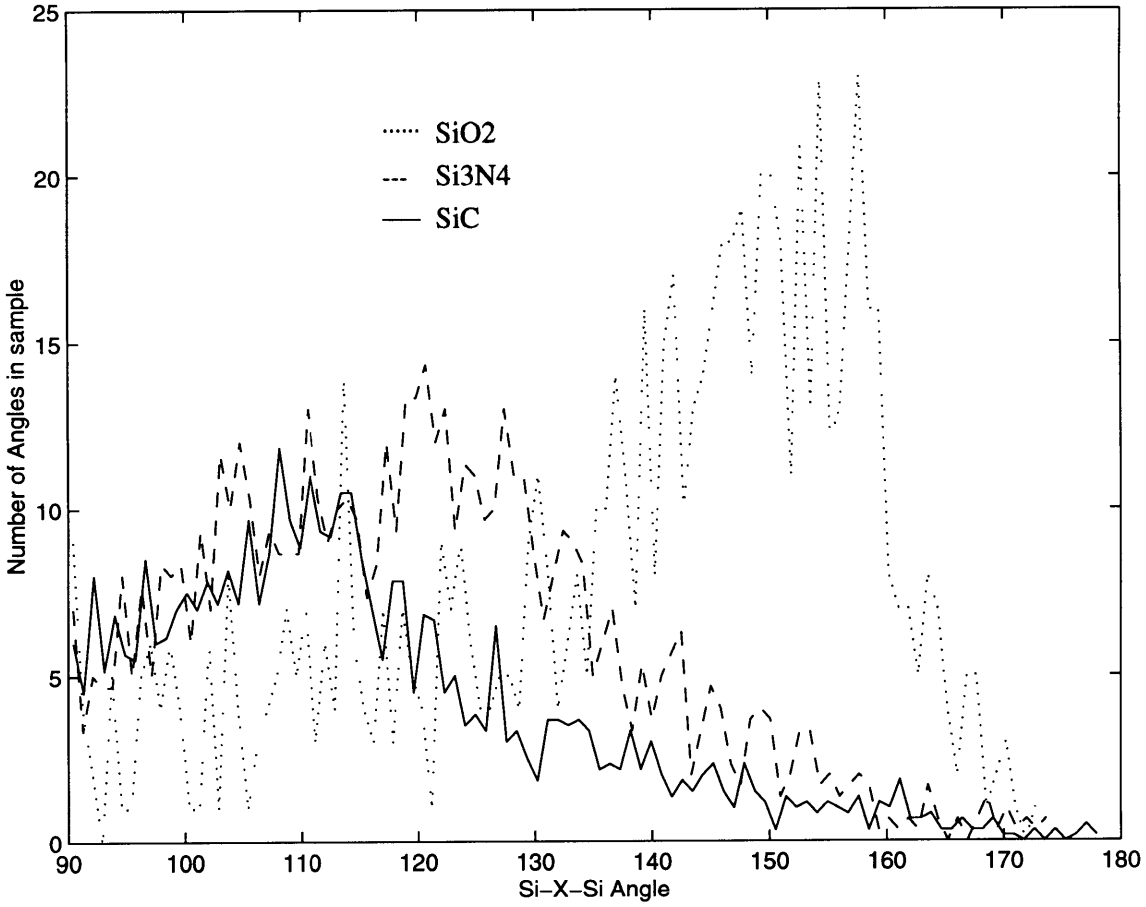

Figure 5.37: Distribution of Si-X-Si inter-tetrahedral angle for the cascade-amorphized regions in α-cristobalite SiO_2, β-Si_3N_4 and α-SiC. The larger overall number of angles for {4,3} Si_3N_4 and {4,4} SiC has been accounted for by normalizing their distributions to that for {4,2} SiO_2 by dividing the number of angles in their distributions by 3 and 6 respectively.

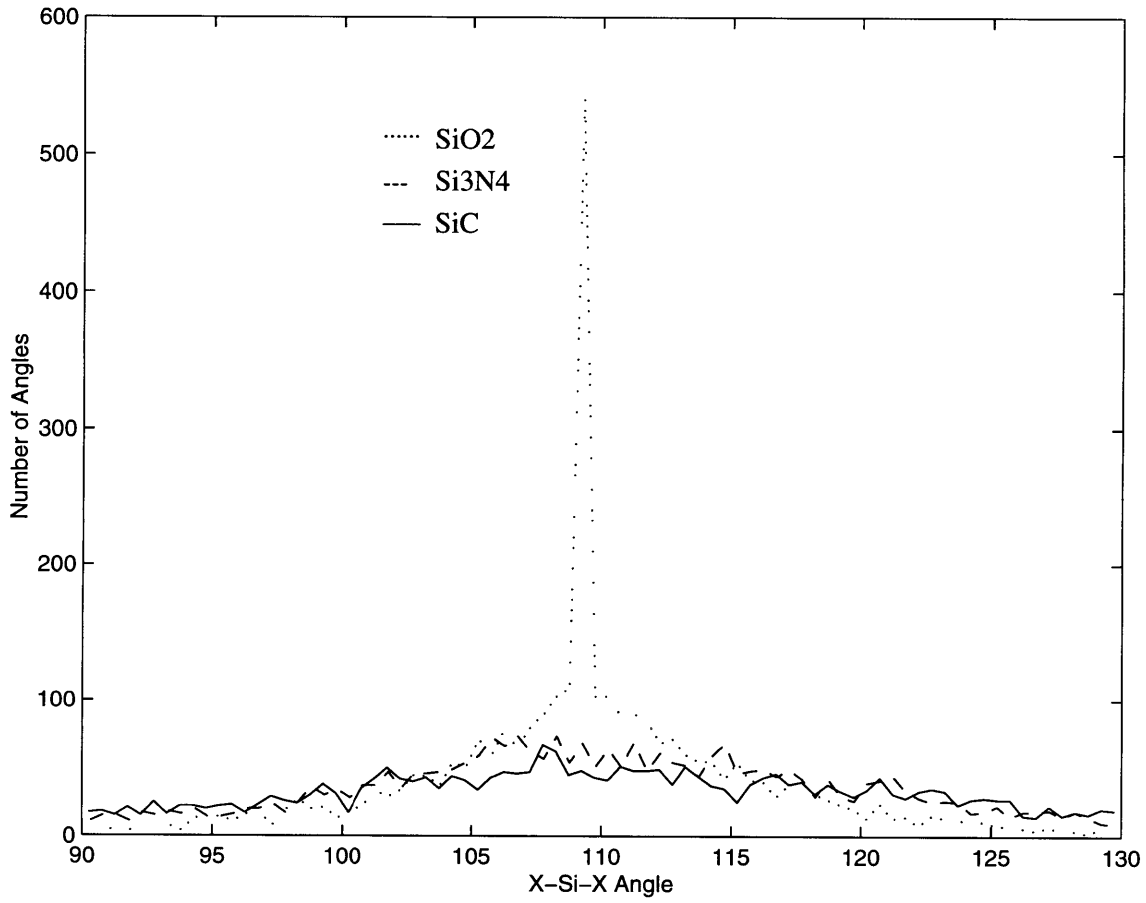

Figure 5.38: Distribution of X-Si-X intra-tetrahedral angle for the cascade-amorphized regions in α-cristobalite SiO_2, β-Si_3N_4 and α-SiC.

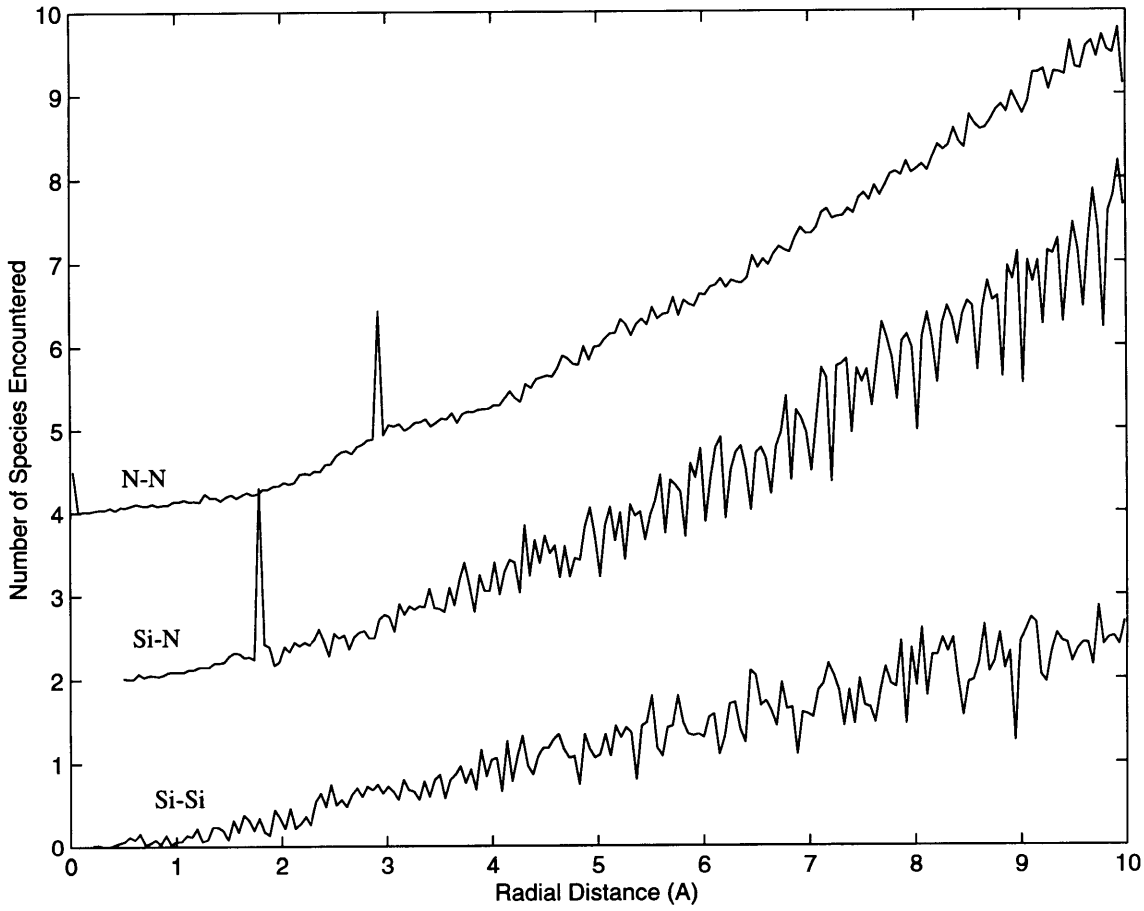

Figure 5.39: Partial radial density function for N-N, Si-N and Si-Si correlations in cascade-amorphized β-Si_3N_4 model.

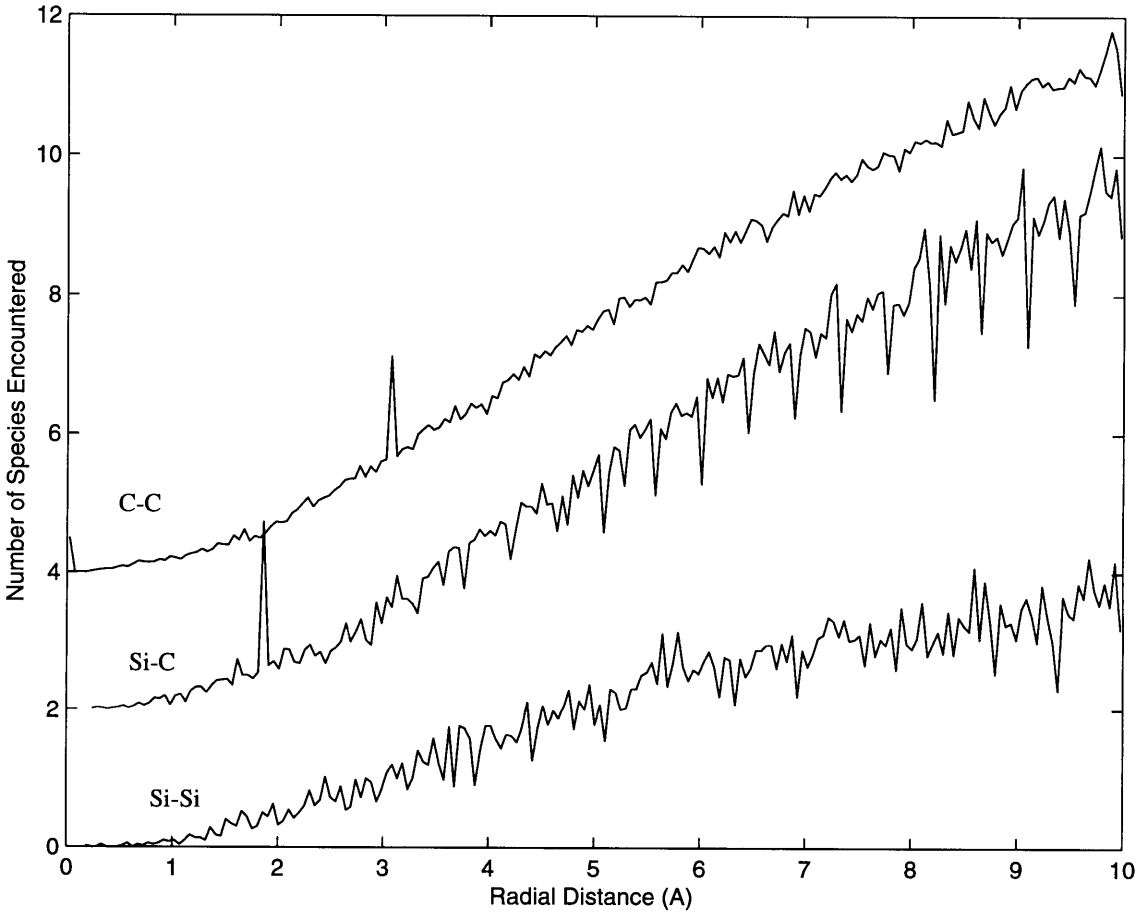

Figure 5.40: Partial radial density function for C-C, Si-C and Si-Si correlations in cascade-amorphized α-SiC model.

Cascade Precursor	**0**	1	2	3	4	5	6	7	8	9	10	11	Σ
α-cristobalite	**72.9**	8.5	13.1	5.5									**27.1**
α-quartz	**72.7**	9.1	9.6	8.6									**27.3**
Ideal quartz	**70.7**	11.1	9.6	8.6									**29.3**
a-SiO_2	**60.1**	11.1	8.3	20.5									**39.9**
β-Si_3N_4	**61.4**	8.6	1.9	0.2	0.6	10.0	13.6	2.9					**38.6**
α-SiC	**56.1**	5.5	3.4	1.8	1.0	0.1	1.0	0.2	10.1	12.9	7.0	2.0	**43.9**

Table 5.6: Percent underconnected tetrahedra listed by number of missing connections in cascade-amorphized silica, Si_3N_4 and SiC models.

Chapter 6

Conclusions

We have demonstrated a method for the rapid assembly of arbitrarily large structural models required for investigation of topological properties of tetrahedral networks. The method, which has been explored for, but is not limited to, vertex-sharing tetrahedra (nor indeed to tetrahedra alone), is based on locally-repeated assembly rules. Surprisingly simple assembly rules sets were formulated for the six tetrahedral network crystalline silica polymorphs as well as Si_3N_4 and SiC polymorphs; these rules also represent rather simple distinctions between structures with large crystallographic and topological disparities once assembled. In silica, a range of displacive modifications is achievable by alteration of initial tetrahedron offset, and both density and Si-O-Si inter-tetrahedral angles were found to be sensitive functions of this choice. The range of allowable angles compatible with retaining connectivity is also easily explored and was found to exceed the range favored by bonding-angle energy considerations for all polymorphs except keatite, whose structure imposes stronger geometrical constraints. The assembly rules proved surprisingly simple, even for crystallographically complex α-Si_3N_4 and the highly over-connected SiC networks, and provide an easily implemented method for rapidly erecting large crystalline models for subsequent manipulation.

A description of local topology, based on a limited set of one-dimensional irreducible rings and associated tetrahedra, has been shown to provide a useful structural unit–the local cluster–for distinguishing all six crystalline polymorphs. Unlike the unit cell, to which it presents a conceptually attractive alternative, the local cluster embodies all topological properties of the crystal structure and is also applicable to non-crystalline structures. Structural density, while a function of displacive modification, was also found to correlate with topology, larger rings and ring size distributions permitting denser structures.

More-or-less fully connected amorphous tetrahedral silica networks were shown to be derivable from minor modifications of the crystal assembly rules and are easily optimized using a simple spring model to represent tetrahedral distortions, steric exclusion codes to

control density, and bond reformation algorithms to maximize connectivity. The local assembly approach also emulates the stochastic progression of glass formation routes. Local clusters for these amorphous structure models evidence local variations in topology in addition to distribution of bond-angles. Partial radial density functions derived from the amorphous structure models retained features of the crystals on which the modified rules were based, but disparities increased with increasing topological deviation from the crystal structure. It is clear that many other topologically disordered structures are possible with further rules modifications, which are being explored.

The similarity of the four silica cascade results provides at least circumstantial evidence that the common density of metamict silicas has its origins in topological constraints. It appears that the different regrowth schemes have minimal effect on the topology of the final configurations, which suggests that the initial random disordering–which establishes roughly the same starting condition for all precursor structures–is the largest driver in the establishing the eventual metamict configuration. It is known from diffraction measurements of radiolytically (electron irradiation) amorphized quartz, cristobalite and tridymite [102] that small differences in metamict structure persist, reflecting the different precursor origins, but the present results for cascade amorphization suggest that such differences may be minimized in cascades. Indeed, significant differences in intermediate-range order are found for electron- and neutron-amorphized quartz [102], though the requisite comparison of neutron-amorphized cristobalite and neutron-amorphized quartz has not been made.

The appearance of larger rings at the expense of smaller rings points to the difficulty in connecting up smaller circuits from a random starting configuration of tetrahedra. The presence of larger rings would be expected to densify a structure like vitreous silica or cristobalite which are initially dominated by 6-rings, because of the ability of larger rings to fold back on themselves and pack more densely than 6-rings. The effect of rings larger than 8-rings in quartz is more difficult to predict. What is clear from the local clusters and ring statistics is that the cascade-amorphized quartz models end up with a more equitable distribution of ring sizes and are no longer dominated by 8-rings; the ratio of small to large rings therefore tips towards smaller rings, and a less dense structure is the expected consequence.

As found in assembly exercises where the initial offset angle was varied, density for a given topology is also a function of the inter-tetrahedral angle achieved, a higher density resulting from a smaller Si-O-Si bond angle θ. While the average Si-O-Si bond angle for cascade-amorphized α-quartz actually decreases (from 143.6° to 139°, Table 5.5), the largest number of angles (peak in the distribution, Figure 5.26) occurs at a higher angle than for undisordered α-quartz, predicting a lowering of the density.

That the computed density of the α-quartz models stays the same (the density of idealized quartz rising to about the same value) suggests that the model cascades retain too

much crystalline character; 8-rings still dominate the two quartz cascades (though not by anything like so much as in crystalline quartz) and 6-rings the cristobalite cascade. One reason is that the disordering step implemented does not allow for translation of the rotated tetrahedra, so they remain in their original positions immediately prior to reconnection. The reconnection thus generates an entity closer to a quasi-crystal (no orientational order, translational order retained) than a fully topologically-disordered arrangement. Idealized quartz is at the low density extreme for quartz topology, and–provided the tetrahedron positions are maintained–any tetrahedron rotations can only densify the structure. The model amorphization procedure thus needs to effect more translational disorder in addition to the orientational disorder provided by tetrahedron rotations. A new procedure has been implemented that allows for random translation of tetrahedra up to an Si-O bond length distance, which should better eliminate the influence of precursor structure on cascade reconstruction and allow dilatation of the quartz cascade.

A further procedural modification being tried is to let the cascade reconnect internally while the boundary is still expanded, before relaxing and reconnecting the boundary to the reconstructed cascade. Of course, the compressibilities of neither the model crystalline matrix nor the model cascade are those of the real materials, and the actual final cascade density will depend on both. Final refinement of the models by optimizing to a realistic potential (for example, in subsequent molecular dynamics simulations with model atom coordinates as starting configurations) will ultimately have to be carried out to provide more quantitative predictions of density. It is qualitatively clear, however, that topological constraints alone have a significant influence on the amorphization route and final metamict configurations.

Topological disorder was found relatively easy to propagate in SiO_2, during assembly or in re-assembly following cascade disordering, and in Si_3N_4 during assembly. SiC could not be disordered in assembly without significant underconnection and tetrahedral distortion, which could both prove energetically unacceptable. The modeling procedure provided easy access to the relevant structural parameters of bond angles, density, topology and radial correlations. The methodology demonstrates the extent to which topology alone may dictate structural options and provides a low-cost complement–if not alternative–to full-blown molecular dynamics approaches for modeling of network structures.

It should be emphasized that the cascade modeling procedure described does not attempt to simulate atomistic processes occurring within a collision cascade but instead to explore the topological possibilities for reconstruction. What the results point to is that the topology of {4,2}-connected silica networks permits reconnection, after collisional disordering, which can continue to propagate sterically-viable topological disorder without substantial underconnection or tetrahedral distortion. In marked contrast, reconnection in Si_3N_4 and SiC produces much more underconnection, substantial tetrahedral distortion, and configu-

rations which–while topologically allowable and technically non-intersecting–appear sterically disastrous and unphysically random. While it appears possible to assemble a topologically disordered (albeit a little underconnected and very crystal-like) model of Si_3N_4 using modified local rules Section 5.1, it does not appear possible to reconnect randomly rotated [SiN_4] tetrahedra. In SiC, it does not appear possible even to assemble a viable amorphous model, let alone cascade- amorphize a crystalline one.

One conclusion is that propagation of cascade-induced topological disorder in Si_3N_4 and in SiC is painful at best and comes with a large energy cost. Another is that the viability of a-SiC is even less than that of a-Si_3N_4, however amorphized. The only other viable option available to either is propagation of a topologically-ordered reconnection from the periphery, which is presumably what occurs in Si_3N_4, a compound that has proven experimentally very difficult to amorphize. The excess energy provided by underconnection and strain in those reconnections that are successful provides a large driving force for recrystallization, an alternative to which is not available as it is in silicas.

That SiC, in fact, experimentally amorphizes readily implies that the operating topologies are far different from those assumed in the cascade modeling. As suggested earlier, introduction of chemical disorder in SiC yields local introduction of Si (or diamond) structure with effectively {4,2}-like topological constraints and $f \approx 0$. The CSi antisite, locally creating a [CC_4] tetrahedron of diamond, is favored energetically and has been found in MD simulations of collision cascades in SiC [19] and detected recently in experimental EXAFS and Raman spectra of ion-amorphized SiC [7]. Such an interpretation of SiC amorphizability implies that a precondition is the establishment of critical antisite defect populations in order to provide sufficient structural freedom to propagate topological disorder. These point defects may anneal thermally at modest temperatures, possibly accounting for (or at least contributing to) the 485 K and 498 K critical temperatures in α- and β-SiC [133, 132], and are produced with higher presumed efficiency by fast-electron irradiation (effecting single displacements instead of cascades), possibly explaining the lower ($\sim$ 300 K) critical temperature [65, 85] for electron irradiation-induced amorphization.

Apart from steric exclusion and optimization spring forces and torques, our cascade simulations model to no potential, and the constraints are purely topological. One consequent limitation is that the computed densities of the amorphized regions cannot be critically compared to experimental density measurements, because the imposed expansion of the constraining periphery has no exact physical basis. The complete set of coordinates obtained can, however, be used as input to MD codes which can relax the structure enthalpically with a realistic potential. The relaxed coordinates can then be used to compute density, radial density correlation functions and elastic constants for comparison with experimental diffraction and mechanical property data. Atomistic modeling of amorphous networks

requires angle-dependent forces, so the potentials are not simple [16]. Refinement of the topological models in this way is nevertheless underway.

6.1 Future research

Molecular dynamics refinement of topological models

Local-rules based simulations generate general atom coordinates from which can be derived not only radial density functions but also (by Fourier transformation) interference functions that can be compared to experimental diffraction profiles. However, because topological modeling does not model to a potential, save that effectively supplied by the vertex springs and any repulsive forces applied, the models produced are not likely to be in a thermodynamically lowest free energy configuration and cannot be compared directly to real configurations. Our models do, nevertheless, reflect the dictates of topological constraints and so do a good deal of the work that has to be done in molecular dynamics simulations. Therefore, they make efficient starting configurations for subsequent MD refinement, using realistic potentials.

Implementation of global ring distribution algorithms

In Section 4.2 we outline the algorithm suggested by Goetzke and Klein [38]. We sketch an analysis of the time complexity of their approach, and whereas for a small sample of local clusters, our algorithm is quite efficient, for global ring statistics, their algorithm is clearly preferable. The addition of efficient enumeration of rings for the structures we produce would, of course, be an enhancement of the existing code. We would like to use the ring counts computed by this algorithm to test for correctness as well as provide a formal proof.

Eutaxy and cascade recrystallization

As indicated in Section 5.2, our computed cascade densities have turned out higher and the RDFs more crystalline than we should have liked. Part of the difficulty is that the possibility of translation (apart form spring adjustments) during cascade reconnection has not been incorporated into the regrowth algorithm. A second is that, apart from tetrahedron overlap proscription, there is no specific steric repulsion term akin to the Si-Si repulsion conventionally thought to govern Si-O-Si bond angles in silicas. Adding repulsion (described in Appendix A but not yet tested) implements a principle known as *eutaxy*, first introduced by

Michael O'Keeffe [95] which holds that what ultimately governs structure is not attractive forces but repulsive forces; in ionic solids, for example, it is the like ions trying to get as far away from each other as possible which governs the structural configuration. It is also our contention that, by forcing our generated structures to stay more open in this way, we will improve the connectivity of the models.

Reconnection pathways

Another way to attack underconnection is to investigate a procedure for finding "reconnection pathways" between pair of underconnected tetrahedra. This idea is loosely based on a technique used in graph matching algorithms. The problem: we want to find a set of disjoint edges that maximally cover the nodes of the graph. If we partition our graph edges into two sets, those that are matching edges and those that are currently unmatched, we can make the following definitions: An "alternating path" is an odd path of edges in the original graph which alternate between matched edges and unmatched edges (m-u-m-u-m-u-m). An alternating path is an "augmenting path" if its two endpoints are unmatched. By exchanging the edges on an augmenting path, we increase the size of our matching. We would like to use a technique with a similar flavor to reduce underconnection.

Single displacement amorphization and percolation threshold

Our "kill and regrow" procedure attempts to simulate in-cascade amorphization where disordering displacements occur simultaneously. However, amorphization can occur from the accumulation of *single* displacements, for example during electron irradiation or radiolysis or when (as suggested for SiC) amorphization takes place only when a critical density of point defects is sustained through cascade overlap. The defects represent local loss of constraints —for example an E′ oxygen vacancy center in SiO_2 constitutes removal of a constraint on two adjacent Si atoms. For marginally-constrained structures like silica, with $f = 0$, removal of a *single* constraint in the network provides (theoretically) structural freedom for the network to rearrange, but of course, such a rearrangement would require an enormous cooperative effort in redefining and rebonding many tetrahedra. In practice, there is a critical local density of removed constraints which must be sustained to provide local freedom for rearrangement. Exploration of the local accumulation of such missing network linkages amounts to testing the *rigidity* and *connectivity percolation thresholds* for the global structural freedom, which have been explored for simple two-dimensional triangular nets (essentially $\{2,6\}$ networks) [68]. Notably, rigidity percolation has a long-range component in that a broken bond in one part of a network can affect rigidity in distant parts of the network.

We would like to explore critical *local* freedom in three-dimensional {4,2} tetrahedral networks like silica as a function of the local density of removed constraints, modeled by progressive local introduction of {3,2} polytopes, followed by the eventual reconnection in altered topologies. If we consider breaking bonds one at a time, what we will have is sets of pairs of neighboring 3-connected tetrahedra. In order to investigate what possible altered structures can be realized, we would restrict reconnection. That is if tetrahedra *a* and *b* are disconnected from eachother and tetrahedra *c* and *d* are likewise disconnected, we will say that *a* and *b* are "taboo" to eachother as are *c* and *d* (that is, we will disallow them from reconnecting). Then, if we can find reconnection pathways between *a* and *d* and *b* and *c*, we may discover a feasible structure.

Modeling network structure of silicate, borosilicate and phosphate glasses

Short-range, chemically-ordered polytopes are the starting point for network formation in our modeling tool. [SiO_4] tetrahedra, [BO_4] tetrahedra and [BO_3] triangular coordination polyhedra are the structural building blocks for borosilicate networks (and their crystalline analogues): [PO_4] tetrahedra for phosphates. [BO_3] triangles and [SiO_4] (and [BO_4]) tetrahedra share each vertex with a second polytope, forming {3,2} and {4,2} networks, In phosphate glasses, only three of the four vertices of the [PO_4] tetrahedra are shared, like [BO_3] triangles generating essentially {3,2} networks, but perhaps more accurately {4,1.75} topological networks, since the geometric availability of the unbonded oxygen vertex for alternative rebonding must be considered during reconstruction (for example, during irradiation). We have indicated the corresponding structural freedoms accorded these networks (Chapter 2): the increased structural freedom of phosphate networks relative to silica networks is evident in the ten-fold increase in amorphizability of Pb phosphates.

In networks, rings have been much explored in the topological modeling analysis. There is evidence that the density is related to ring complement, and changes in ring topology can be reflected in density changes, as supported by the results for silicas discussed in Chapter 4. The correlation suggests that the structures of vitreous and irradiation-amorphized silicas are—like the tridymite and cristobalite crystalline polymorphs—largely dominated by 6-rings, a distribution generally confirmed by our assembly modeling studies and in molecular dynamics [121] models. The energies of the silica inter-tetrahedral bond angle are fairly flat until 3-ring configurations (130.5°) are reached, so a distribution of ring sizes is expected. The distribution may be spatially segregated by size, resulting in network structures which are even less homogeneous. It is possible, for example, to envisage heterogeneous silica structures in which delimited regions dominated by 6-rings are linked to each other by larger

and smaller rings. Larger rings are responsible for the higher density of the denser silica polymorphs because (unlike smaller, more rigid rings) they can fold back on themselves, and the densification of vitreous silica by irradiation could arise from opening up of 6-rings to larger rings at regional boundaries. In B_2O_3 glass, the boroxyl 3-rings, comprising three corner-sharing [BO_3] triangles, purportedly make up the greater pan of the structure [136]. In phosphate glasses, linear chains are a more prominent feature than rings [105].

Our modeling codes have been written in such a general way that they can easily deal with [BO_3] triangles and 3-connected [PO_4] tetrahedra, as well as {4,4}-connected [SiO_4] and [BO_4] tetrahedra. The formation of non-bridging oxygens in alkali silicates adjacent to alkali modifiers can be dealt with in similar fashion to 3-connected [PO_4] tetrahedra in phosphates. We would like to explore the topological controls on the assembly of [BO_3] triangles in B_2O_3 networks, 3-connected [PO_4] tetrahedra in P_2O_5 networks, and 3-connected [SiO_4] in alkali silicates (where the alkali is treated as bound to a NBO and can bind to up to 5 other NBOs). Next, we could explore co-assembly of [BO_3] triangular and 3- or 4-connected [SiO_4] and [BO_4] tetrahedral mixed polytopes in alkali borosilicate glasses. This mixed polytope case is not so different from the treatment of mixed conformational proteins in virus shell assembly[5]; the assembly can be carried out by random polytope addition in stoichiometric proportions or with a segregation bias. An analogous treatment in co-assembly of 3-connected [PO_4] with the [FeO_6] octahedra likely found in the proposed bon phosphate waste glasses or or 8 9-fold oxygen-coordinated Pb ions found in the lead phosphate glasses previously investigated [116] is more problematical because of the edge- and face-sharing involved and is better dealt with in the kinetic rules-based modeling scheme outlined next. Local cluster and bond angle analysis will be carried out in these simulations, as for the silica, nitride and carbide glass models described in this thesis.

Kinetic rules-based modeling

Local rules-based topological approaches and molecular dynamics approaches are at opposites ends of a modeling spectrum. In the first, interatomic potentials are in evidence only insofar as polytope connection spring forces and torques enforce topological preferences and steric exclusion repulsive forces are needed to prevent polytope overlap in the second, topology arises out of energy minimization as an afterthought. One approach is a hybrid approach which, for want of a better term, might be called *kinetic* rules-based modeling. In this approach [106, 107], the basic bond abstraction is extended with the notion of binding kinetics, in that the structural entities are set in motion and can bind or not bind according to bond energy preferences and also local rules stipulations. The objects assembling can be atoms or can be larger coordination units, as in our tetrahedron assembly, which attach to each other. The procedure is a little like doing simple molecular dynamics with foreknowl-

edge of the network topological preferences.

The kinetic rules modeling approach is a natural one for simulating cascades in network structures, because it allows for the translation of polytypic units (and therefore, allows antisite disorder in SiC) during initial disordering and rebonding that we need to build into our cascade simulations.

Appendix A

Implementation

This appendix describes the basic components of the simulator in detail and provides an overview of the major algorithms used. This code is derived from the virus shell toolkit developed by Berger, Muir and Schwartz.

A.1 Polyhedron Abstraction

The basic unit in every simulator model is the polyhedral node which consists of an atom of one type located at the center of a regular polyhedron and four atoms of another type located at each of its vertices. The parameters that can vary between models include the center atom type, the vertex atom type, the vertex degree (the number of other nodes that can connect at a vertex), and the polyhedron degree (the number of vertices in the polyhedron). In addition, for a given model the user can define multiple node types and how they attach to each other. For example, in Chapter 3 in the description for the rules of quartz, there was shown a representation of a node in a model of SiO_2 that has a polyhedron degree of four and a vertex degree of one.

Each polyhedral node has a data structure associated with it that keeps track of information needed for the simulation. This includes the coordinates of the center of the node, vectors to each of its corners for the center, rotation vectors, its polyhedral degree and maximum number of neighbors, optimal bond angles for each of its neighbors, and pointers to each of its neighbors. Much of this information is derived from the local rules detailed in the next section and is used for breadth first growth as discussed in Section A.5.1.

A.2 Local Rules

Local rules are an important element of the simulator. They control both the process of adding a new node to the structure as well as interactions between pre-existing nodes. They are specified by the user in a rules file as described in Section A.4.1 and are loaded in before

The work reported in this appendix is joint work with Vinay Pulim and will be published in his SM thesis.

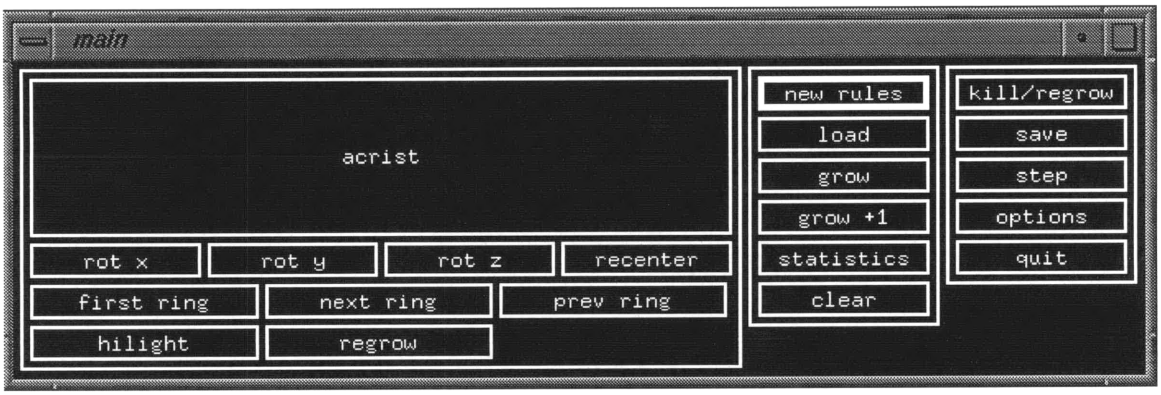

Figure A.1: Main window of the graphical user interface.

a simulation starts. A rules file lists every type of node and the set of local rules associated with them. The first component of the local rules is a definition of the position and orientation of the initial node. This definition is used during the building of a new structure to decide how to orient the first node. The second component is listing of transformations that specify how to add a new neighboring node at each of its vertices. In the simulator, these transformations are stored in an array of matrices, one for each neighbor of each corner of each node type.

When adding new nodes, the matrix associated with a given node's neighbor is applied to a copy of that node to rotate and translate it into the correct position. In a sense, a clone is made of the parent node and then transformed relative to the parent. In addition, three dimensional array also store information about neighbors' node types and corner numbers. The local rules also indirectly specify the optimal bond angle and torque angle between a given node and each of its neighbors. The simulator calculates these angles by actually growing a temporary structure with a root node of the current node type and then adding each of neighbors while measuring the resulting bond angles.

Local rules are also used during growth to attach pre-existing nodes together. When two nodes are within a sufficient distance from each other, the simulator checks their types and determines whether or not they can attach to each other under their local rules. In addition, during optimization steps, nodes are transformed relative to each other to in sure the bond angles between them are as close to the optimal bond angles as possible.

A.3 The Graphical User Interface

A.3.1 Buttons

The user interacts with the simulator through a graphical user interface. The main window is shown in Figure A.1. It consists of a rules box and twenty buttons which control the simulation. The function of each of the components is explained in this section.

The rules box simply displays the name of the primary rules set being used in the current simulation. Any operations performed that do not ask the user to specify a rules set will use

the ones displayed in the rules box.

The first row of buttons beneath the rules box are used to control the user's viewpoint within the graphics display. The "rot x", "rot y", and "rot z" buttons rotate the viewpoint around each of the three coordinate axes. In addition, the "recenter" button is used to return the viewpoint to the default position along the positive y-axis with the positive z-axis pointing upwards and the positive x-axis pointing to the left.

The next row contains the ring viewing buttons which are only useful after a local cluster has been computed. The "first ring" button displays the first ring in the local cluster, and the "next ring" and "prev ring" buttons cycle through the rest of the rings.

The bottom row contains the "highlight" button, which displays the current structure with underbound nodes highlighted in green, as well as the "regrow" button which draws only the regrow region on the graphics displays after a collision cascade has been computed.

The "new rules" button allows the user to read in a new set of rules. These rules will affect only new nodes added to the existing structure and will not change the rules associated with nodes that are already present. This is useful for the simulation of collision cascades which require two sets of rules, one for the original structure and another for the regrow region. The simulator searches for rules files in the current directory as well as the "rules" subdirectory.

The "save" button writes the contents of the current simulation to a data file, including the simulations parameters, the location and states of all of the nodes, their corresponding adjacency matrix, and the rules associated with each node. The button first prompts the user for a file name before continuing. The "load" button reads in a data file and updates the graphics display to show the newly loaded simulation. By default, the simulator saves and loads files from a subdirectory with the same name as the currently loaded rules set.

The "grow" button adds nodes to the simulation using the currently loaded rules set. It first prompts the user for the number of nodes to add before continuing. The "grow +1" button is very similar to the "grow" button except that it does not prompt the user and it only adds one node to the simulation. This is useful for a step-by-step visualization of a simulation.

The "kill/regrow" button begins a collision cascade simulation. The user is prompted for the size of the cascade. The resulting simulation will depend on the options set and (newly) defined rules file (the cascade nodes are subjected to the last rules set loaded before the "kill/regrow" button was pressed). See Section A.5.7 for details about the kill/regrow procedure.

Figure A.2 shows the sub-window of the "options" button. This sub-window contains various simulation parameters that the user can change. These include the turning on or off of graphics, optimization, spinodal decomposition during regrowth, and VRML output. In addition, the user can set various constants such as the spring constant, depth of search for rings, optimization threshold, radial distribution function (RDF) radius, bond lengths, and molar masses.

The "statistics" button brings up a sub-window listing various operations that can be performed on the simulation (shown in Figure A.2. The "node number" button will create a local cluster for the node entered into the text box. The "sample size" button will create local clusters for a random sampling of nodes with the sample size specified in the text box. Furthermore, the "distances" button will calculate RDF distances for a random sampling

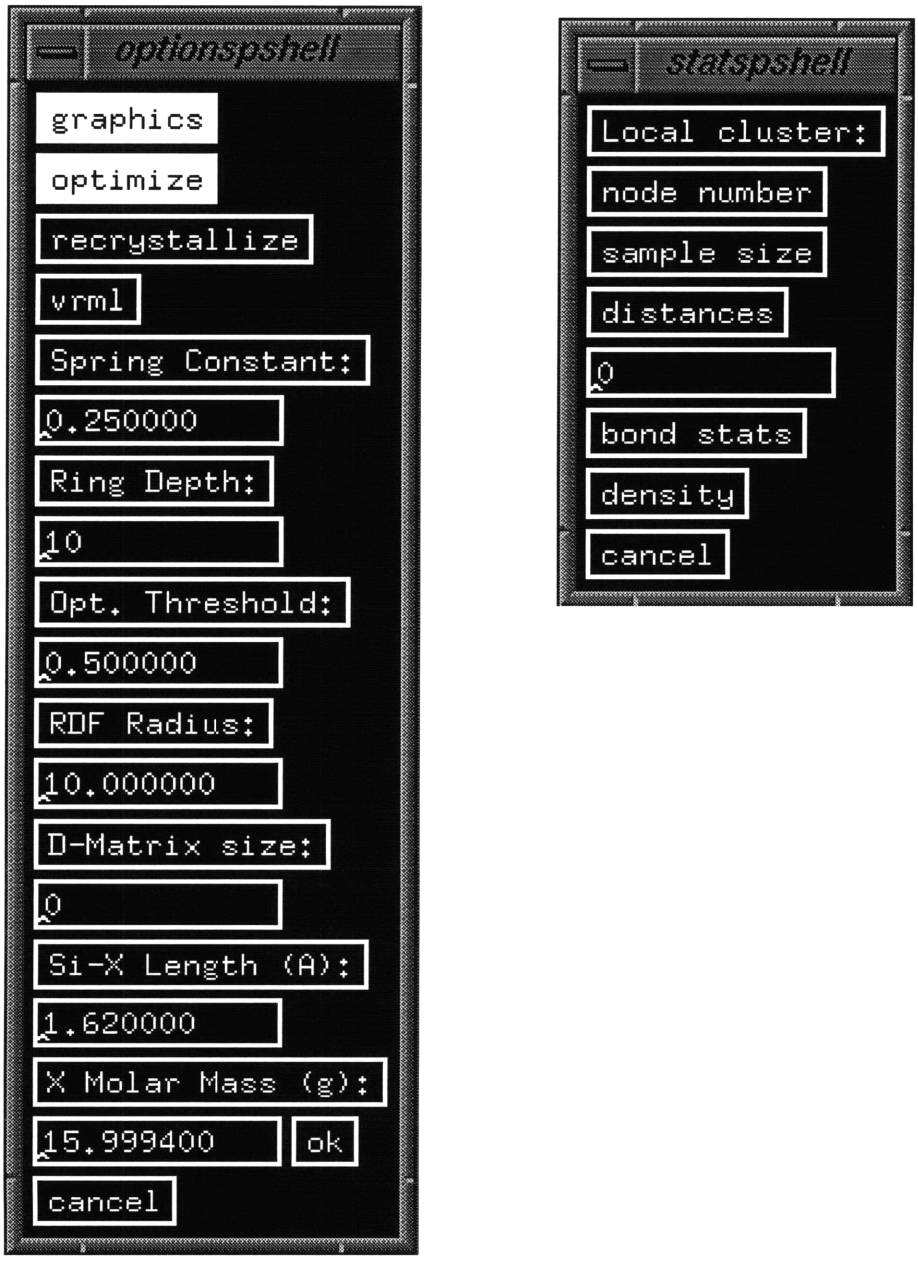

Figure A.2: The options (left) and stats (right) sub-windows.

of nodes. The "bond stats" button will calculate a variety of statistics such as the bond angle distribution, bond lengths, and the number of underbound nodes. Finally, the "density" button will calculate the approximate density of the current structure.

The last two buttons, "clear" and "quit" perform the obvious operations of destroying the current structure and exiting the program.

A.3.2 Graphics Display

The graphics display provides the user with a three dimensional visual representation of the simulation. Each node is represented by a shaded yellow polyhedron, except for the root node which is shaded red and underbound nodes which are shaded green. However, during local cluster ring displays, the color scheme changes slightly. Nodes in the local cluster will be shaded light blue and the currently highlighted ring will be dark blue. In every display, springs which connect polyhedra at their corners will always be represented by red lines.

The graphics in the simulator are produced using the OpenGL graphics library, OpenGL is available on a variety of platforms and allows for very portable code without a loss in graphics quality. In addition, the simulator allows the user to disable graphics so that it is still possible to run simulations on platforms that lack the proper support.

Although the graphics display is very useful for visualizing simulations, it does act as a bottleneck during the simulation, especially when one is dealing with large structures. The simulator may have to wait for the graphics to be displayed before continuing calculations. To solve this problem, the user can disable the graphics display before a simulation is run and then re-enable the display once it is complete.

A.4 Data Files

The simulator uses three types of data files: rules files, grow files, and VRML files. Rules files define each node type, describe how they interact, and set up an initial node. Grow files contain the entire state of a simulation and can be used to interrupt a simulation and resume it at a later time. VRML files are similar to grow files except they only contain enough data to reconstruct a graphical representation of the simulation., and they are only readable by VRML browsers and OpenInventor compatible viewers. Data such as simulation parameters, adjacency information, and rules are not saved with VRML files. This section describes each file type and provides an overview of their implementation.

A.4.1 Rules Files

Figure 3.1 shows a sample rules file. The first line of the file specifies the number of node types. The second line determines the degree of the polyhedron for the first node type as well as the number of neighbors at each corner. In this case, the node type is a tetrahedron whose corners are each seeking one neighbor. The third line specifies whether or not the polyhedron is regular, and if it is not then the initial corner coordinates must be specified. The fourth line gives an initial rotation applied to the initial node. Rotations are specified by a

series of rotations around the coordinates axis of the form "<axis1> <degrees1> <axis2> <degrees2> ...<axisN> <degreesN>;" where "axisN" is one of "x", "y", or "z" and degreesN is the number of degrees to rotate around the specified axis. The remaining lines specify rules for each corner. In the example, the first of these lines gives the rule for corner 0, which is connected to corner 1 of a node of type 0. This is followed by a rotation of that neighboring tetrahedron. The information in lines 2-8 is repeated for each node type.

A.4.2 Grow Files

Grow files are binary files and therefore are not directly readable by a text viewer. This is done in order to conserve disk space and to allow for faster saving and loading of files. The first element of a grow file is the version number of the simulator used to create it. This information is used by the simulator to insure that the grow file is compatible with the current version. The version number is followed by information about the nodes, such as the number of node types, the polyhedron degree of each type of node, the number of neighbors at each corner, and the number of nodes. Next is a listing of every node and all of the information associated with each one. This includes such information as the node's location and the rules associated with the node. After this, the grow file contains a listing of the adjacency information which specifies how each nodes connects to its neighbors. This is followed by the listing of the kill region nodes, if any, and finally the pre-computed distance matrix, if it exists.

A.4.3 VRML Files

VRML file provide an easy way to export the graphics displayed by the simulator to other viewers. They contain VRML code that describes the location and orientation of each node in the simulation and no other information. The VRML files can be read by any VRML 1.0 compatible viewer, which includes all VRML browsers as well as OpenInventor compatible viewers. To create VRML output files, the VRML option must be checked in the options menu.

A.5 Major Algorithms

A.5.1 Breadth First Growth

New nodes are added to the structure in breadth first order. That is, the corners of older nodes are filled before corners of the newer nodes, similar to the way a breadth first search of a tree checks all of the nodes on one level before moving down to the next level. For instance, assume the simulator is currently working on the parent node A, which has four unfilled corners. It would first try to fill all of node A's corners before attempting to fill the corners of any of its children. This breadth first order insure that the growing structure is well balanced and symmetric, and it models how glass actually grows in nature.

The breadth first growth is actually implemented by a queue which initially contains just the root node. This node is then removed and each of its corners are checked to see if they can attach to nearby nodes. Since this is the first node it will not have any neighbors so new nodes are added to each of its corners. These new nodes are then added to the end of the queue. The first node in the queue is then removed and each of its corners are checked for neighbors, and if none exist then nodes are added to each of its corners. These new nodes are then added to the end of the queue, and the next node is removed form the head of the queue. This process is continued until either the queue is empty or the maximum number of nodes has been reached. During the procedure nodes, some problems may arise. For instance, no neighboring nodes may exist near an unfilled corner of a node and there may not enough room to add a new node. In this case, nearby bonds may have to be broken and reattached to accommodate the new node. A detailed explanation of the breadth first growth algorithm is given here in pseudo-code:

```
queue is initialized to empty
if no nodes exist in the structure
  add new node to queue
else
  for each node i in the structure
    if node i has an unfilled slot
      add node i to queue
    end
  end
end
while queue is not empty
  remove node i from the head of the queue
  for each corner j of node i
    for each slot k of corner j
      if k is empty
        try to attach a nearby node
        if no nearby node could be attached
          add a new node to node i at slot k
          if successful
            add the new node to tail of queue
          else
            try to break and reattach to a nearby node
          end
        end
        optimize the structure
      end
    end
  end
end
```

A.5.2 Ring Finding and Local Clusters

A local cluster for a given node is composed of the set of all nodes in every primitive ring that passes through that node. A primitive ring for a given node is determined by finding the shortest path through existing nodes from one vertex of the node back to another vertex of the node. One or more primitive rings can exist for each pair of vertices of a given node. A ring is calculated by performing a breadth first search of all nodes branching off from one vertex of the given node and ending when that node is hit again during the search. The user can specify the depth of the breadth first search to optimize speed. Many rings go through a node, called a test node for clarification, but a ring is only primitive if for each node in the ring the shortest path to the test node is through the nodes in the ring. To aid in primitive ring calculations, a distance matrix is calculated first. It contains graph distances between every pair of nodes. The graph distance between a pair of nodes is equal to the number of nodes in between the two nodes plus one. Initially, the simulator calculated the distance matrix for the entire structure but this proved to be a very time consuming operation. Therefore, a new data structure know as a local distance matrix was devised to improve the speed of calculations.

A.5.3 Local Distance Matrices

A local distance matrix (LDM) is very similar to a normal distance matrix except in the way that it is calculated and in the amount of information that it contains. An LDM only contains enough information to calculate a local cluster for a single test node. More specifically, it contains the distances between the test node and all other nodes that are reachable through a breadth first search to a user specified depth. Since every primitive ring through the test node is a subset of this set, no more information is need than is contained within an LDM. The speedup in execution time by using LDM in place of an entire distance matrix is immense without any loss in accuracy.

A.5.4 Density Calculations

The simulator uses two methods for computing density. The first method simply samples several spherical regions within a structure and averages the densities computed within each one. This method is very fast without much loss in accuracy. The second method computes a convex hull around the entire structure and then computes the enclosed volume and mass, and from this the density. This method, although it is slower and less accurate, is useful for computing the density of an entire structure (not just regions within it). This method is less accurate because it is extremely difficult to compute the convex hull of extremely porous structures.

A.5.5 Optimization

The simulation uses a simple spring model to represent the forces between nodes. Each node is connected to each of its neighbors with a single spring. During each step of optimization the springs are relaxed and allowed to exert various forces on the nodes. The basic forces are

translational forces, rotational forces, bending forces, and twisting forces. The translational force exerted by a spring pulls the center of mass of a polyhedral node along the spring's axis. The translational forces applied to each of the node's corners are averaged and applied to the center of the node, changing only its position but not affecting its orientation. The rotational force exerted by a spring rotates the node around its center allowing its corner to get closer to its neighbor. These forces are also averaged and rotate the node accordingly. The bending forces do not result directly from the springs. Rather, they are forces created to push bond angles between adjacent nodes closer to the optimal bond angle determined by the rules. The bending force can be thought of as a force exerted by a bent spring that is trying to return to its original low energy state. Finally, the twisting forces are forces that attempt to push the torque between two nodes connected by a spring to an optimal torque angle that has already been computed from the rules.

Since the polyhedral nodes are abstractions of physical structures they are subject to several constraints. Most importantly, the polyhedron represented by an individual node must remain rigid during the course of a simulation. In addition, the angle formed by two neighboring polyhedra is limited by both a minimum and a maximum value since bonds cannot bend past certain thresholds. Finally, due to steric constraints polyhedra cannot overlap or intersect each other. The simulator ensures that none of these constraints are violated during the course of an experiment.

As mentioned earlier in Section A.5.1, during growth there is sometimes not enough room for a new node to be inserted. In this case, nodes near the current parent node must be broken apart and reattached to either the parent node or other nearby nodes. This procedure involves searching for a pair of nodes whose point of attachment is closest to the parent node's current corner. These nodes are then broken apart and one of them is reattached to this corner. The other node can either attach to another corner of the parent node or it can rejoin the breadth first growth queue and later attach to another free node. This breaking and reattaching greatly reduces the number of underbound nodes when growing an irregular glass structure and during collision cascades. The optimization algorithm is summarized here:

```
while total spring energy > threshold
  for each node i in structure
    for each corner j of node i
      for each slot k of corner j
        calculate forces on slot k of corner j of node i
        apply forces to node i and move it accordingly
        place node i in the correct bucket
      end
    end
  end
  calculate total spring energy of structure
end
```

The forces acting on a given slot are calculated as follows:

```
dir is the translational force vector
torqs is the array of rotational torque vectors
initialize dir to the zero vector
initialize torqs to empty
add a radial expansion force to dir if performing a collision cascade
if slot is not empty
  get node i connected to slot
  if spring to node i is too long then break it and return
  calculate offset to node i from slot
  add a force proportional to offset to dir
  calculate torque vector resulting from offset and add to torqs
  determine optimal bond angle by averaging angles from both nodes
  calculate torque vector needed to reach optimal bond angle
  add it to torqs
  calculate torque vector needed to reach optimal twist angle
  add it to torqs
  perform a nearest neighbor search from current slot
  for each node j in nearest neighbor list
    for each corner k of node j
      if k is within repulsion threshold and all of its slots are full
        calculate torque needed to repulse slot from corner k
        add it to torqs
      else if k has an empty slot
        calculate torque needed to attract slot to corner k
        add it to torqs
      end
    end
  end
end
```

A.5.6 Buckets and Nearest Neighbor Search

A time consuming step during growth and optimization is searching for nodes that are within a certain distance of a given node. Initially, this was accomplished by calculating the distance to every node in the structure and checking whether or not it was within the required threshold. However, as structures get very large, the time required to perform this calculation grows very quickly. To solve this problem, the simulator implements buckets, subdivisions of the simulation workspace which keep track of every node within its region. Using buckets, to find neighboring nodes, the simulator only needs to search neighboring buckets instead of searching the entire structure. They allow for a nearest neighbor search time that grows linearly with the size of the structure. A single bucket is implemented by the following structure:

```
structure {
```

```
  size:  integer
  list:  array of nodes
} Bucket
```

The global variables b_width, b_height, and b_depth determine the dimensions of the three dimensional array containing all of the buckets in the simulation. In addition, the global variable b_size determines the dimensions of the cubical volume of each bucket. When a node is added to the structure it is assigned to the bucket containing the space which the node is in. The actual insertion of the node into the bucket is accomplished by adding the node to the bucket structure's list element and incrementing its size element.

Buckets allow for extremely fast nearest neighbor searches, on the order of O(1). The actual algorithm used to find the nodes near a node n is given here:

```
let r be the search radius from node n
let buckets be the array containing all buckets intersected by
  a sphere s of radius r centered at node n
for each bucket b in buckets
  for each node i in b
    if the coordinates of node i are within sphere s
      add i to nearest neighbor list
    end
  end
end
return nearest neighbor list
```

A.5.7 Collision Cascades

Collision cascades simulate the effects of irradiation on a structure. The simulator performs collision cascades using two different methods. The first method, recrystallization, removes all the nodes within the affected region and then adds new nodes to the boundary until the vacuum is filled. New nodes are added according to a different set of rules from those used to grow the original structure. A common action sequence that a user might follow is to first grow a large structure using rules set A, remove a fifth of the nodes located in the center of structure, load a new rules set B, and then regrow the deleted nodes. A description of the recrystallization algorithm follows:

```
queue is initialized to empty
for each node i in the irradiated region
  for each corner j of node i
    for each slot k of corner j
      if the node attached at slot k is outside the irradiated
        region and it is not already in queue then add it to
        queue
```

```
      end
    end
  end
end
for each node i in the irradiated region
  remove node i from structure
end
while queue is not empty
  remove node i from the head of the queue
  for each corner j of node i
    for each slot k of corner j
      if k is empty
        try to attach a nearby node
        if no nearby node could be attached
          add a new node to node i at slot k
          if successful
            add the new node to tail of queue
          else
            try to break and reattach to a nearby node
          end
        end
        optimize the structure
      end
    end
  end
end
for each node i in the structure
  if node i has an unfilled slot then add it to the queue
end
while queue is not empty
  remove node i from the head of the queue
  for each corner j of node i
    for each slot k of corner j
      if k is empty
        try to attach a nearby node
        if no nearby node could be attached
          try to break and reattach to a nearby node
        end
        optimize the structure
      end
    end
  end
end
```

In future versions of the simulator, a variant of the algorithm will be implemented which gradually changes the rules as one moves from the boundary to the center of the irradiated region. Node that are close to the boundary will grow new nodes according to rules that are very similar to the original rules. However, nodes closer to the center will follow the newer rules.

The second method of performing collision cascades is spinodal decomposition. This method involves disturbing the nodes in the irradiated region by breaking all bonds and randomly rotating and offsetting nodes. Then, the nodes are allowed to move and reattach themselves using a different rules set until all bonds are reformed. The algorithm used for spinodal decomposition is as follows:

```
for each node i in the irradiated region
  disturb node i by translating and rotating it slightly
end
queue is initialized to empty
for each node i in the structure
  if node i has an unfilled slot then add it to the queue
end
while queue is not empty
  remove node i from the head of the queue
  for each corner j of node i
    for each slot k of corner j
      if k is empty
        try to attach a nearby node
        if no nearby node could be attached
          try to break and reattach to a nearby node
        end
        optimize the structure
      end
    end
  end
end
for each node i in the structure
  if node i has an unfilled slot then add it to the queue
end
while queue is not empty
  remove node i from the head of the queue
  for each corner j of node i
    for each slot k of corner j
      if k is empty
        try to attach a nearby node
        if no nearby node could be attached
          try to break and reattach to a nearby node
        end
        optimize the structure
```

```
        end
      end
    end
  end
```

The best method to use for collision cascades varies between structures and it is up to the user to decide which is better.

Bibliography

[1] H. Abe, H. Naramoto, and C. Kinoshita. Amorphization of graphite under ion or electron irradiation. In *Materials Research Society Symposium Proceedings*, volume 373, pages 383–388, 1995.

[2] J.M. Aitken and E.A. Irene. Silicon dioxide films in semiconductor devices. In M. Tomozawa and R.H. Doremus, editors, *Treatise on Materials Science and Technology*, volume 26, pages 1–56. Academic Press, New York, NY, 1986.

[3] R. S. Averback, M. Ghaly, and H. Zhu. Surface damage during keV ion irradiation: results of computer simulations. In *Materials Research Society Symposium Proceedings*, volume 373, pages 337–348, 1995.

[4] Bonnie A. Berger and P. W. Shor. Local rule switching mechanism for viral shell geometry. MIT Laboratory for Computer Science Technical Memo 527, 1995.

[5] Bonnie A. Berger, P. W. Shor, L. Tucker-Kellogg, and J. King. A local rules based theory of virus shell assembly. *Proceedings of the National Academy of Science, USA*, 91:7732–7736, 1994.

[6] J.D. Bernal. The Bakerian lecture, 1962: The structure of liquids. In *Proc. R. Soc.*, volume A280, pages 299–322, London, 1964.

[7] W. Bolse. Formation and development of disordered networks in Si-based ceramics under ion bombardment. *Nuclear Instrumental Methods*, B, 1998. In press.

[8] N. Bordes and R. C. Ewing. Ion-beam and electron-beam induced amorphization of berlinite ($AlPO_4$). In *Materials Research Society Symposium Proceedings*, volume 373, pages 395–400, 1995.

[9] C.J. Brinker. Structural studies of sol-gel silicate glasses. *Transactions of the American Crystollographic Association*, 27:163–190, 1991.

[10] P.J Burnett and T.F. Page. Effects of ion implantation on the mechanical properties of fully and partially stabilized zirconias. *American Ceramic Society Bulletin*, 65:1393–1398, 1986.

[11] W.G. Cady. *Piezoelectricity*. Dover Publications, New York, NY, 1964.

[12] S.L. Chan, L.F. Gladden, and S.R. Eliot. Magnetic resonance studies on neutron-irradiated quartz and amorphous silica. *Journal of Non-Crystalline Solids*, 106:413–416, 1988.

[13] L. Coes. A new dense crystalline silica. *Science*, 118:131–132, 1953.

[14] A.R. Cooper. Zachariasen's rules, Madelung constant, and network topology. *Physics and Chemistry of Glasses*, 19(4):60–68, 1978.

[15] E. A. Cooper, C. D. Hughes, W. L. Earl, K. E. Sickafus, G. W. Hollenberg, F. A. Garner, and R. C. Bradt. Cation disorder determined by MAS^{2}7Al NMR in high dose neutron irradiated spinel. In *Materials Research Society Symposium Proceedings*, volume 373, pages 413–418, 1995.

[16] A. N. Cormack and Y. Cao. Molecular dynamics simulation of silicate glasses. In B. Silvi and P. D'Arco, editors, *Modeling of minerals and silicated meterials*, pages 227–271. Kluwer Academic Publishing, Drecht, Netherlands, 1997.

[17] T.H. Cormen, C.E. Leiserson, and R.L. Rivest. *Introduction to Algorithms*, chapter 26, page 550. The MIT electrical and computer science series. Massachusetts Institute of Technology, Cambridge, Massachusetts, third edition, 1990.

[18] G. Das and T.E.Mitchell. Electron radiation damamge in quartz. *Radiation Effects*, 23:49–52, 1974.

[19] T. Diaz de la Rubia, M.-J. Caturla, and M. Tobin. Molecular dynamics studies of radiation effects in silicon carbide. In *Materials Research Society Symposium Proceedings*, volume 373, page 555=566, 1995.

[20] J. M. Delaye and D. Ghaleb. Molecular dynamics simulation of SiO_2 +B_2O_3 +Na_2O +ZrO_2 glass. *Journal of Non-Crystalline Solids*, 195:239–248, 1996.

[21] B.N. Delone. Proof of the fundamental theorem in the theory of stereohedra. *Soviet Mathemetics*, 2:812–817, 1961.

[22] R.A.B. Devine. Macroscopic and microscopic effects of radiation in amorphous SiO_2. *Nuclear Instrumental Methods*, B91:378–390, 1994.

[23] M.T. Dove, A.P. Giddy, and V. Heine. Rigid unit mode model of displacive phase transitions in framework silicates. *Transactions of the American Crystallographic Association.*, 27:65–75, 1991.

[24] S. Dutton, D.J.R. Taylor, and R.F.T. Stepto. Monte-Carlo modeling of the formation, structure and properties of polymer networks. *Die Angewandte Makromol. Chemie*, 240:39–57, 1996.

[25] R. K. Eby, R. C. Ewing, and R. C Birtcher. The amorphization of complex silicates by ion-beam irradiation. *Journal of Materials Research*, 7:3080–3102, 1992.

[26] E.P. EerNisse and C.B. Norris. Introduction rates and annealing of defects in ion-implanted SiO_2 layers on Si ii, the molecular geometry of simple liquids. *Journal of Applied Physics*, 45:5196–5205, 1974.

[27] S.R. Elliott. Extended-range order, interstitial voids and the first sharp diffraction peak of network glasses. *Journal of Non-Crystalline Solids*, 1995.

[28] R. C. Ewing, L. M. Wang, and W. J. Weber. Amorphization of complex ceramics by heavy-particle irradiations. In *Materials Research Society Symposium Proceedings*, volume 373, pages 347–358, 1995.

[29] R. C. Ewing, W. J. Weber, and F. W. Clinard. Radiation effects in nuclear waste forms for high-level radioactive waste. *Progress in Nuclear Energy*, 29:63–127, 1995.

[30] R.C. Ewing. The metamict state: 1993 – the centennial. *Nuclear Instrumental Methods*, B91:22–29, 1994.

[31] Jr. F. W. Clinard, G. F. Hurley, and L. W. Hobbs. Neutron irradiation damage in MgO, Al_2O_3 and $MgAl_2O_4$ ceramics. *Journal of Nuclear Materials*, 108-109:655–670, 1982.

[32] J.L. Finney. Random packings and the strucutre of simple liquids. *Proc. Royal Society*, A319:495–507, 1970.

[33] E.M. Flanigen, J.M. Bennett, R.W. Grose, J.P. Cohen, R.L. Patton, R.M. Kirchner, and J.V. Smith. Silicalite, a new hydrophobic crystalline silica molecular sieve. *Nature*, 271:512–515, 1978.

[34] O.W. Flörke, O.W. Flörke, and U. Giese. Moganite: A new microcrystalline silica-mineral. *Neues Jahrbuch Min. Abh.*, 149:325–336, 1984.

[35] J. F. Gibbons. Ion implantation in semiconductors. II. Damage production and annealing. *Proceedings of the IEEE*, 60:1062–1096, 1972.

[36] G.V. Gibbs, E.P. Meagher, M.D. Newton, and D.K. Swanson. A comparison of experimental and theoretical bond length and angle variations for minerals, inorganic solids and molecules. In M. O'Keeffe and M.A. Navrotsky, editors, *Structure and Bonding in Crystals*, volume 1, pages 195–225. Academic Press, New York, NY, 1981.

[37] L.F. Gladden. Medium-range order in v-SiO_2. *Journal of Non-Crystalline Solids*, 119:318–330, 1990.

[38] K. Goetzke and H.J. Klein. Properties and efficient algorithmic determination of different classes of rings in finite and infinite polyhedral networks. *Journal of Non-Crystalline Solids*, 127:215–220, 1991.

[39] W. Gong, L.M. Wang, R.C. Ewing, and H.S. Xie. Interface-mediated amorphization of coesite by 200 keV electrons. *Journal of Applied Physics*, 1997. In press.

[40] D.L. Griscom. Point defects and radiation damage processes in alpha-quartz. In *Proceedings of the 33rd Frequency Control Symposium*, pages 98–109, Washington, D.C., 1979. Electronic Industries Assn.

[41] P. K. Gupta. Rigidity, connectivity, and glass forming ability. *Journal of the American Ceramic Society*, 76:1088, 1993.

[42] P. K. Gupta. Non-crystalline solids: glasses and amorphous solids. *Journal of Non-Crystalline Solids*, 195:158–164, 1996.

[43] P. K. Gupta and A. R. Cooper. Topologically disordered networks of rigid polytopes. *Journal of Non-Crystalline Solids*, 123:14, 1990.

[44] Lester Guttman. Ring structure of the crystalline and amorphous forms of silicon dioxide. *Journal of Non-Crystalline Solids*, 116:145–147, 1990.

[45] A.C. Hannon, D.I. Grimley, R.A. Hulme, A.C. Wright, and R.N. Sinclair. Boroxol groups in vitreous boron oxide: new evidence from neutron diffraction and inelastic neutron scattering studies. *Journal of Non-Crystalline Solids*, 177:299–316, 1994.

[46] H.X. He. Computer-generated vitrous silica networks. *Journal of Non-Crystalline Solids*, 89:402–416, 1987.

[47] P.J. Heaney. Structure and chemistry of the low-pressure silica polymorphs. *Reviews in Minerology*, 29:1–40, 1994.

[48] P.J. Heaney and J.E. Post. The widespread distribution of a novel silica polymorph in microcrystalline quartz varieties. *Science*, 255:441, 1992.

[49] R.J. Hemley, A.P. Jephcoat, H.K. Mao, L.C. Ming, and M.H. Manghnani. Pressure-induced amorphization of crystalline silica. *Nature*, 334:52–54, 1988.

[50] R.J. Hemley, C.T. Prewitt, and K.J. Kingma. High-pressure behavior of silica. *Reviews in Minerology*, 29:41–81, 1994.

[51] Higgins. Silica zeolites and clathrasils. *Reviews in Mineralogy*, 29:507–543, 1994.

[52] L. W. Hobbs, A. E. Hughes, and D. Pooley. A study of interstitial clusters in irradiated alkali halides using direct electron microscopy. In *Proceedings of the Royal Society of London, Series A*, volume 332, pages 167–185, 1973.

[53] L. W. Hobbs, A. N. Sreeram, C. E. Jesurum, and B. A. Berger. Structural freedom, topological disorder, and the irradiation-induced amorphization of ceramic structures. *Nuclear Instrumental Methods*, B116:18–25, 1996.

[54] Linn Hobbs. Network topology in aperiodic networks. *Journal of Non-Crystalline Solids*, 192:79–91, 1995.

[55] Linn Hobbs. The role of topology and geometry in the irradiation-induced amorphization of network structures. *Journal of Non-Crystalline Solids*, 182:27–39, 1995.

[56] L.W. Hobbs. Point defect stability in ionic crystals at high defect concentrations. *J. Physique*, 37[C7]:3–26, 1976.

[57] L.W. Hobbs. Murphy's law and the uncertainty of electron probes. In *Scanning Microscopy Supplement*, volume 4, pages 171–183, 1990.

[58] L.W. Hobbs. Topology and geometry in the irradiation-induced amorphization of insulators. *Nuclear Instrumental Methods*, B91:30–42, 1994.

[59] L.W. Hobbs, F.W. Clinard, S.J. Zinkle, and R.C. Ewing. Radiation effects in ceramics. *Journal of Nuclear Materials*, 216:291–321, 1994.

[60] L.W. Hobbs, C.E. Jesurum, and V. Pulim. Topological modeling of cascade amorphization in network structures using local rules. *Materials Science and Engineering*, 1998. in press.

[61] L.W. Hobbs, C.E. Jesurum, V. Pulim, and B. Berger. Local topology of silica networks. *Philosophical Magazine*, B, 1998. in press.

[62] L.W. Hobbs and M.R. Pascucci. Radiolysis and defect structure in electron-irradiated α-quartz. *J. Physique*, 41 [Colloque C6]:237–242, 1980.

[63] L.W. Hobbs and A.N. Sreeram. Structural criteria for amorphization of network solids. In *Materials Research Society Symposium Proceedings*, volume 373, pages 359–364, 1995.

[64] H. Inui, A. Suzuki H. Mori, and H. Fujita. Electron-irradiation-induced crystalline-to-amorphous transition in beta-SiC single crystals. *Philosophical Magazine*, 65:1–14, 1992.

[65] H. Inui, H. Mori, and H. Fujita. Electron-irradiation-induced crystalline to amorphous transition in alpha-SiC single crystals. *Philosophical Magazine*, 61:107–124, 1990.

[66] H. Inui, H. Mori, and T. Sakata. High-resolution electron microscopy study of electron-irradiation-induced crystalline-to-amorphous transition in alpha-SiC single crystals. *Philosophical Magazine*, 66:737–748, 1992.

[67] H. Inui, H. Mori, T. Sakata, and H. Fujita. Electron irradiation induced crystalline-to-amorphous transition in quartz single crystals. *Journal of Non-Crystalline Solids*, 116:1–15, 1990.

[68] D.J. Jacobs and M.F. Thorpe. Generic rigidity percolation: the pebble game. *Physical Review Letters*, 75:4051–4054, 1995.

[69] U. Jain, A.C. Powell, and L.W. Hobbs. Simulation of the crystal-to-amorphous transformation in irradiated quartz. In *Materials Research Society Symposium Proceedings*, volume 209, pages 201–206, 1991.

[70] C.E. Jesurum, V. Pulim, and L.W. Hobbs. Modeling the cascade amorphization of silicas with local-rules reconstruction. *Nuclear Instrumental Methods*, B, 1998. in press.

[71] C.E. Jesurum, V. Pulim, and L.W. Hobbs. Topological modeling of amorphized tetrahedral ceramic network structures. *Journal of Nuclear Materials*, 1998. in press.

[72] C.E. Jesurum, V. Pulim, L.W.Hobbs, and B. Berger. Modelling of topologically-disordered tetrahedral network structures using local rules. In G.E. Matthews and R.T. Williams, editors, *13th International Conference on Defects in Insulating Materials*, number 239-241 in Materials Science Forum, pages 37–40. Trans Tech Publications, July 1996.

[73] F. W. Clinard Jr., D. E. Peterson, D. L. Rohr, and L. W Hobbs. Self-irradiation effects in 238Pu-substituted zirconolite. I. temperature dependence of damage. *Journal of Nuclear Materials*, 126:245–254, 1984.

[74] P.P. Keat. A new crystalline silica. *Science*, 120:328–330, 1954.

[75] P. Kofstad. *High Tempurature Corrosion*. Elsevier Applied Science, London, 1988.

[76] E. Lell, N.J. Kreidl, and J.R. Hensler. Radiation effects in quartz, silica and glass. In J.E. Burke, editor, *Progress in Ceramic Science*, volume 4, pages 1–93. Pergamon Press, New York, NY, 1966.

[77] F. Liebau. *Structural Chemistry of Silicates. Structure, Bonding and Classification*. Springer–Verlag, Berlin, 1985.

[78] J.K.N. Lindner, R. Domres, and E.H. te Kaat. Radiation damage and amorphization of silicon by 6 MeV Ni ion implantation. *Nuclear Instrumental Methods*, B39:306–310, 1989.

[79] J.K.N. Lindner, R. Zuschlag, and E.H. te Kaat. Radiation damage and amorphization of silicon by 2 MeV nitrogen ion implantation. *Nuclear Instrumental Methods*, B62:314–318, 1992.

[80] Carol Marians and Linn Hobbs. Local structure of silica glasses. *Journal of Non-Crystalline Solids*, 119:269–282, 1990.

[81] Carol Marians and Linn Hobbs. Network properties of crystalline polymorphs of silica. *Journal of Non-Crystalline Solids*, 124:242, 1990.

[82] C.S. Marians. *A language for the study of silica networks*. PhD dissertation, Massachusetts Institute of Technology, Department of Materials Science and Engineering, 1988.

[83] C.S. Marians and L.W. Hobbs. A language for the study of network silica glasses. In R.A. Weeks and D.L. Kinser, editors, *Effects of Modes of Formation on the Structure of Glasses*, volume 53 and 54 of *Diffusion and Defect Data*, pages 31–36. Trans Tech Publications, Aedermannsdorf, Switzerland, 1987.

[84] C.S. Marians and L.W. Hobbs. Characterization of SiO_2 surfaces as a function of network connectivity. *Journal of Non-Crystalline Solids*, 106:317–320, 1988.

[85] A. Matsunaga, C. Kinoshita, K. Nakai, and Y. Tomokiyo. Radiation-induced amorphization and swelling in ceramics. *Journal of Nuclear Materials*, 179-181:457–460, 1991.

[86] Hj. Matzke. Radiation damage and xenon release in quartz and fused silica following ion bombardment. *Phys. Stat. Sol.*, 18:285–295, 1966.

[87] J. Clerk Maxwell. On the calculation of the equilibrium and stiffness of frames. *Philosophical Magazine*, 27:294, 1864.

[88] C. J. McHargue, P. S. Sklad, and C. W. White. The structure of ion implanted ceramics. *Nuclear Instrumental Methods*, B46:79–88, 1990.

[89] W.M. Meier and D.H. Olson. *Atlas of Zeolite Strucutre Types*. Butterworth–Heinemann, Boston, MA, 3rd rev. edition, 1992.

[90] G. Miehe and H. Graetsch. Crystal structure of moganite: a new structure type for silica. *European Journal of Minerology*, 4:693–706, 1992.

[91] S.E. Miller and A.G. Chynoweth. *Optical Fiber Telecommunications*. Academic Press, New York, NY, 1979.

[92] R.L. Mozzi and B.E. Warren. The structure of vitreous silica. *Journal of Applies Crystallography*, 2:164–172, 1969.

[93] Doug Muir. Simulating the formation of viral protein shells. Sm thesis, M.I.T., Cambridge, MA, 1994.

[94] D.F. Mullica, H.O. Perkins, D.A. Grossie, L.A. Boatner, and B.C. Sales. Structure of dichromate-type lead pyrophosphate, $Pb_2P_2O_7$. *Journal of Solid State Chemistry*, 62:371–376, 1986.

[95] M. O'Keeffe. On the arrangements of ions in crystals. *Acta Crystallogr.*, A33:924–927, 1977.

[96] M.R. Pascucci, J.L. Hutchison, and L.W. Hobbs. The metamict transformation in alpha-quartz. *Radiation Effects*, 74:219–226, 1983.

[97] R.L. Pfeffer. Damage center formation in SiO_2 thin films by fast electron irradiation. *Journal of Applied Physics*, 57:5176–5180, 1985.

[98] W. Primak. Fast-neutron-induced changes in quartz and vitrous silica. *Physical Review*, 110:1240–1254, 1958.

[99] W. Primak. *Compacted States of Vitreous Silica — Studies on Radiation Effects in Solids*. Gordon and Breach, New York, NY, 1975.

[100] W. Primak and R. Kampwirth. The radiation compaction of vitrous silica. *Journal of Applied Physics*, 39:5651–5658, 1968.

[101] L.C. Qin. HREM electron-irradiated silicas. In G.W. Bailey and C.L. Reider, editors, *Proceedings of the 51st Annual Meeting of EMSA*, pages 1102–1103, San Fransisco, CA, 1993. San Fransisco Press.

[102] L.C. Qin and L.W. Hobbs. Energy-filtered electron diffraction study of vitreous and amorphized silicas. *Journal of Non-Crystalline Solids*, 192&193:456–462, 1995.

[103] J. Rankin, L. W. Hobbs, L. A. Boatner, and C. W. White. An in situ annealing study of lead implanted single crystal calcium titanate. *Nuclear Instrumental Methods*, B32:28–31, 1988.

[104] A.G. Revesz and G.V. Gibbs. Structural and bond flexibility of vitreous SiO_2 films. In G. Lucovsky, S.T. Pantelides, and F.L. Galeener, editors, *The Physics of MOS Insulators*, pages 92–96. Pergamon, New York, NY, 1980.

[105] B.C. Sales, J.O. Ramey, J.C. McCallum, and L. A. Boatner. Structural differences between the glass state and ion-beam-amorphized states of lead pyrophosphate. *Journal of Non-Crystalline Solids*, pages 179–193, 1990.

[106] R.S. Schwartz. A multi-threaded simulator for the kinetics of virus shell assembly. Sm thesis, M.I.T., Cambridge, MA, 1996.

[107] Russell Schwartz, Peter W. Shor, Peter E. Prevelige, Jr., and Bonnie Berger. Local rules simulation of the kinetics of virus capsid self-assembly. Submitted to the Journal of Molecular Biology, December 1997. Presented at the 1997 Phage and Virus Assembly Meeting in Monterrey, CA in June, 1997.

[108] J.F. Shackleford. The interstitial structure of non-crystalline solids. *Journal of Non-Crystalline Solids*, 204:205–216, 1996.

[109] K. E. Sickafus, A. C. Larson, M. Nastasi N. Yu, G. W. Hollenberg, F. A. Garner, and R. C. Bradt. Cation disorder in high dose, neutron-irradiated spinel. *Journal of Nuclear Materials*, 219:128–134, 1995.

[110] I. Simon. Structure of neutron-disordered silica. *Phys. Rev.*, 103:1587–1588, 1956.

[111] I. Simon. Structure of neutron-irradiated quartz and vitreous silica. *Journal of the American Ceramic Society*, 40:150–153, 1957.

[112] T.L. Simpson and B.E. Volcani. *Silicon and Siliceuos Structures in Biological Systems*. Springer, New York, NY, 1981.

[113] L.L. Snead and S.J. Zinkle. Amorphization and the effect of implanted ions in SiC. In *Materials Research Society Symposium Proceedings*, volume 373, pages 377–382, 1995.

[114] L.L. Snead, S.J. Zinkle, J.C. Hay, and M.C. Osborne. Amorphization of sic under ion nad neutron irradiation. *Nuclear Instrumental Methods*, B, 1998. In press.

[115] A.N. Sreeram, L.W. Hobbs abd N. Bordes, and R.C. Ewing. Irradaition-induced amorphization of $AlPO_4$. *Nuclear Instrumental Methods*, B116:126, 1996.

[116] A.N. Sreeram and L.W. Hobbs. Structure characterization of metamict and glassy lead phosphate. In *Materials Research Society Symposium Proceedings*, volume 279, pages 559–564, 1993.

[117] A.N. Sreeram and L.W. Hobbs. Characterization of metamict and glassy lead phosphates. In *Materials Research Society Symposium Proceedings*, volume 321, pages 26–31, 1994.

[118] S.M. Stishov and S.V. Popova. A new dense modification of silica. *Geochemistry (USSR)*, 10:923–926, 1961.

[119] R. Szostak. *Handbook of Molecular Sieves*. Van Nostrand Reinhold, New York, NY, second edition, 1997.

[120] K. Tanimura, T. Tanaka, and N. Itoh. Creation of quasistable lattice defects by electronic excitation in SiO_2. *Physical Review Letters*, 51:423–426, 1983.

[121] P. Vashishta, A. Nakano, R.K. Kalia, and I. Ebbsjö. Molecular dynamics simulations of covalent amorphous insulators on parallel computers. *Journal of Non-Crystalline Solids*, 182:59–71, 1995.

[122] B. Vessal, M.Amini, and C.R. Catlow. Computer simulation of the structure of silica glass. *Journal of Non-Crystalline Solids*, 159:184–186, 1993.

[123] G.F. Voronoĭ. Nouvelles applications des paramètres continus â la théorie des formes quadritiques. *J. Reine Angew. Math.*, 134:198–287, 1908.

[124] L. M. Wang and R. C. Ewing. Ion beam-induced amorphization of $(Mg,Fe)_2SiO_4$ olivine series: an in situ transmission electron microscopy study. In *Materials Research Society Symposium Proceedings*, volume Bulletin 17, pages 333–338, 1992.

[125] L. M. Wang, R. C. Ewing, W. J. Weber, and R. Eby. Temperature and ion-mass dependence of amorphization dose for ion beam irradiated zircon ($ZrSiO_4$). In *Materials Research Society Symposium Proceedings*, volume 279, pages 451–456, 1993.

[126] L. M. Wang, W. L. Gong, N. Bordes, R. C. Ewing, and Y. Fei. Effects of ion dose and irradiation temperature on the microstructure of three spinel compositions. In *Materials Research Society Symposium Proceedings*, volume 373, pages 407–412, 1995.

[127] L.M. Wang. Private communication.

[128] W. J. Weber. Radiation-induced defects and amorphization in zircon. *Journal of Materials Research*, 5:2687–2697, 1990.

[129] W. J. Weber. Radiation-induced amorphization in complex silicates. *Nuclear Instrumental Methods*, B65:88–92, 1992.

[130] W. J. Weber. Alpha-decay-induced amorphization in complex silicate structures. *Journal of the American Ceramic Society*, 76:1729–1738, 1993.

[131] W. J. Weber, G. J. Exarhos, and L. M. Wang. Temperature and dose dependence of metal colloid production in alpha-irradiated CaF_2 single crystals. In *Microstructure of Irradiated Materials. Symposium*, volume 373, pages 311–316, 1995.

[132] W. J. Weber, L. M. Wang, and N. Yu. The irradiation-indiced crystalline-to-amorphous phase transition in α-sic. *Nuclear Instrumental Methods*, B 116:322–326, 1996.

[133] W.J. Weber and L.M. Wang. The temperature dependence of ion-beam-induced amorphization in beta-SiC. *Nuclear Instrumental Methods*, B106:298–302, 1995.

[134] J. S. Williams, R. D. Goldberg, M. Petravic, and Z. Rao. Phase transformations and compound formation during ion irradiation of materials. *Nuclear Instrumental Methods*, B84:199–203, 1994.

[135] M.C. Wittels and F.S. Sherrill. Radiation damage in SiO_2 structures. *Phys. Rev.*, 93:117–118, 1954.

[136] A.C. Wright. Neutron and X-ray amorphography. In C.J. Simmons and O.H. El-Bayoumi, editors, *Experimental techniques of glass science*, Ceramic Transactions, chapter 8. American Cermaic Society, 1992.

[137] A.C. Wright. The structure of vitreous silica. *Journal of Non-Crystalline Solids*, 179:84–115, 1994.

[138] A.C. Wright, R.A. Hulme, D.I. Grimley abd R.N. Sinclair, S.W. Martin, D.L. Price, and F.L. Galeener. The structure of some simple amorphous network solids revisited. *Journal of Non-Crystalline Solids*, 129:213–232, 1991.

[139] A.F. Wright and M.S. Lehmann. The structure of quartz at 25 and 590° C determined by neutron diffraction. *Journal of Solid State Chemistry*, 36:371–380, 1981.

[140] N. Yu, K. E. Sickafus, and M. Nastasi. First observation of amorphization in single-crystal $MgAl_2O_4$ spinel. *Philosophical Magazine*, 70:235–240, 1994.

[141] N. Yu, K. E. Sickafus, and M. Nastasi. Temperature effects on ion irradiation damage in $MgAl_2O_4$ spinel single crystals. In *Materials Research Society Symposium Proceedings*, volume 373, pages 401–406, 1995.

[142] W.H. Zachariasen. The atomic arrangement in glass. *Journal of the American Chemical Society*, 545:3841–3851, 1932.

[143] J. F. Ziegler, J. P. Biersack, and U. Littmark. *Stopping and range of ions in solids*, page 321. Pergamon Press, New York, NY, 1985.

[144] S. J. Zinkle. Microstructure of ion irradiated ceramic insulators. *Nuclear Instrumental Methods*, B91:234–246, 1994.